Polarization properties and nonlinear dynamics of quantum dot lasers

Lukasz Olejniczak

To cite this version:

Lukasz Olejniczak. Polarization properties and nonlinear dynamics of quantum dot lasers. Other. Université Paul Verlaine - Metz, 2011. English. NNT : 2011METZ001S . tel-01752962

HAL Id: tel-01752962
https://hal.univ-lorraine.fr/tel-01752962v1

Submitted on 29 Mar 2018

Vrije Universiteit Brussels, Belgium
Department of Applied Physics and Photonics
Brussels Photonics Team B-PHOT
&
SUPELEC, Metz, France
OPTEL & LMOPS EA 4423 (Lab. Matériaux Optiques,
Photonique et Systèmes)

Doctor of Philosophy Dissertation

Polarization properties and nonlinear dynamics of quantum dot lasers

by

Lukasz Olejniczak

Promotors:
Prof. Dr. Sc. Krassimir Panajotov
Prof. Dr. Ir. Marc Sciamanna

2010

Thesis defended on February 16, 2011

Members of the jury
Prof. Dr. W. ELSAESSER President
Prof. Dr. A. VALLE Reviewer
Prof. Dr. Th. ERNEUX Reviewer
Prof. Dr. Ir. H. THIENPONT Examiner
Prof. Dr. K. PANAJOTOV PhD Director
Prof. Dr. Ir. M. SCIAMANNA PhD Director

Contents

Acknowledgements

Three years of living abroad and working toward a PhD have definitely been the most intensive part of my life. This journey to the unknown turned out to be full of adventures, new experiences and people, that greatly contributed to make my dream come true.

The razor sharp difference between being a student and being a PhD student did not become obvious to me at once. Fortunately, thanks to my supervisors: Krassimir PANAJOTOV and Marc SCIAMANNA, I have learned at some moment that solutions to large problems must come in small, although still requiring hard work, steps. First of all, I would like to express my deep gratitude to both of you for giving me the opportunity to develop my interest into semiconductor components and opening a PhD position in your teams. Next, thank you for your patience and for your friendly and encouraging attitude. Finally, thank you for your guidance and inspiration. I am really glad to have worked with you. Without you this thesis would not have been possible. I would like to express my special gratitude to Sebastian WIECZOREK for his contributions to our study on nonlinear dynamics in optically injected quantum dot lasers and teaching me some trick of the trade in using AUTO.

Financial support from Vrije Universiteit and SUPELEC during all the years spent in Brussels and Metz is also thankfully acknowledged.

I would also like to extend my thanks to my fellow PhD students and colleagues that contributed to the quality of my life here abroad, especially: Marek NAPIERALA, Mateusz ZUJEWSKI, Tomek NASILOWSKI, Babar BASHIR, Xunqi WU, Nicolas MARSAL and Damien RONTANI.

On a more personal basis, I would like to thank my fiancee Monika, my parents and brothers for their support and all the happiness they brings in my life.

Parts of this work have been published in the following articles:

1. L. Olejniczak, M. Sciamanna, H. Thienpont, K. Panajotov, A. Mutig, F. Hopfer, D. Bimberg, ”Polarization Switching in Quantum-Dot Vertical-Cavity Surface-Emitting Lasers,” IEEE Phot. Techn. Lett., 21, 14, pp. 1008–1010, 2009.

2. L. Olejniczak, M. Sciamanna, K. Panajotov, ”Polarization instabilities and nonlinear dynamics in a quantum dot laser”. In Technical Digest of ICTON 2009:(4 pages), Island of Sao Miguel, Azores (Portugal), 2009.

3. M. Sciamanna, L. Olejniczak, I. Gatare, K. Panajotov, H. Thienpont, A. Valle, ”Semiconductor lasers nonlinear dynamics: complexity made useful”. In ICTON Mediterranean Winter (ICTON-MW’09), Angers (France), 2009.

4. L. Olejniczak, K. Panajotov, H.Thienpont, M.Sciamanna, ”Self-pulsations and excitability in optically injected quantum dot lasers: impact of the excited states and spontaneous emission noise,” Phys. Rev. A, 82, 023807, 2010.

5. L. Olejniczak, K. Panajotov, S. Wieczorek, H.Thienpont, M.Sciamanna, ”Intrinsic gain switching in optically injected quantum dot laser lasing simultaneously from the ground and excited state,” J. Opt. Soc. B, 27, 11, pp. 2416–2423, 2010.
   Selected to Virtual Journal of Ultrafast Science, 9, 12, December 2010.

6. L. Olejniczak, M. Sciamanna, H. Thienpont, K. Panajotov, A. Mutig, F. Hopfer, D. Bimberg, ”Polarization properties and instabilities of QD VCSELs,” Proc. of SPIE, Semiconductor Lasers and Laser Dynamics IV, 7720, 77201, pp. G1–G11, 2010.

7. L. Olejniczak, M. Sciamanna, H. Thienpont, K. Panajotov, ”Optical injection dynamics of quantum dot lasers: influence of the excited states,” Proc. of SPIE, Semiconductor Lasers and Laser Dynamics IV, 7720, 772022, pp. 1–9, 2010.

8. L. Olejniczak, M. Sciamanna, H. Thienpont, K. Panajotov, A. Mutig, F. Hopfer, D. Bimberg, ”Polarization switching and polarization mode hopping in quantum dot vertical-cavity surface-emitting lasers,” Optics Express, vol. 19, no. 3, pp. 2476–2484, 2011.

Chapter 1

Introduction

In the past decade semiconductor lasers have become key devices in applications ranging from optical telecommunications and data storage to manufacturing and medical treatment. On the one hand side, such a strong market position is a consequence of their numerous advantages including low power consumption, single-mode continuous wave operation at room temperature, broad spectrum of achievable wavelengths and possibility of direct modulation. On the other hand, there is a strong demand for small, reliable sources of coherent light which do not require bulky and expensive external power suppliers and cooling stages.

In this introductory chapter we give a brief overview of the historical development and characteristics of quantum dot (QD) semiconductor lasers. We start by a description of nanostructures that can potentially be used as active regions in semiconductor lasers and show how the size quantization effects can improve their performance. Next, we discuss properties of actual QDs. In particular, we focus on their inhomogeneous broadening, effects of the excited states, capture and relaxation processes, linewidth enhancement factor and temperature stability. Next, we describe two geometries of semiconductor lasers studied in this thesis, namely edge emitting (EEL) and vertical-cavity surface-emitting (VCSEL) ones. Active region of the investigated VCSELs consists of QDs grown either in Stranski-Krastanov or in submonolayer mode. We discuss optical properties of both kinds of QDs and then summarize the progress that has been made in the development of QD EEL and QD VCSELs.

1.1 From bulk to quantum dots (QDs)

A real breakthrough in the semiconductor laser technology turned out to be the implementation of double heterostructures, where the term heterostructure refers to an artificial crystal built of two semiconductor materials with different values of the energy bandgap, refractive index, effective mass, mobility of charge carriers etc. [1]. In the most common approach a narrow energy bandgap material is sandwiched between materials with larger energy bandgap, which results in the formation of potential barriers at the junctions. As it is shown in Fig. 1.1, such barriers can then be effectively used to confine charge carriers, because they always attempt to lower their energy. Notice however, that the confined carriers are still free to move in all three spacial directions. Since the region of carrier recombination is largely limited to the middle layer, the energy of the emitted photons will be determined by its bandgap energy.

Yet another advantage of double heterostructures is that amongst materials relevant to photonics technology, those with narrower energy bandgap are in general characterized by larger refractive index [2]. This means that the middle layer can also act as a planar waveguide for the emitted photons, providing both carrier and optical confinement, see Fig. 1.1.

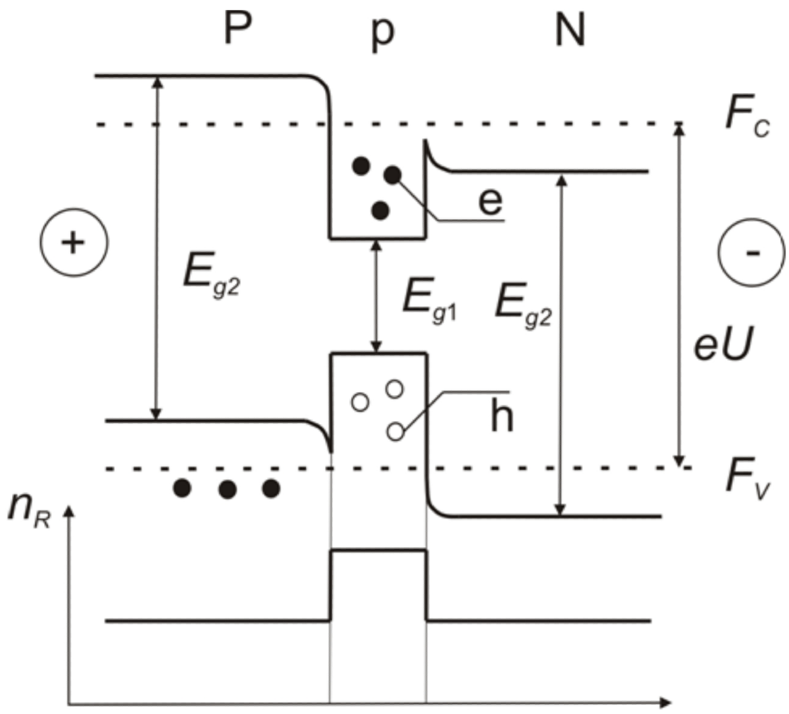

Figure 1.1: Double heterostructure in which a lower energy bandgap material E_{g1} is sandwiched between materials with larger energy bandgap E_{g2}, which leads to both optical and carrier confinement, the former due to larger refractive index n_R of materials with narrower energy bandgap.

If the thickness of the middle layer d is comparable with the de Broglie wavelength of the charge carriers, then this particular band alignment as in

Fig. 1.1 is called a quantum well (QW). Such size reduction changes the energy spectrum of the charge carriers and the density of states. The latter property describes the number of available carrier states in unit volume and unit energy interval. In bulk materials the energy spectrum of a free electron in the conduction band is given by [3]:

$$E = E_g + \frac{\hbar^2 k^2}{2m^*} = \frac{\hbar^2}{2m^*}(k_x^2 + k_y^2 + k_z^2), \tag{1.1}$$

where E_g is the energy bandgap, m^* is the effective mass of an electron, while $\hbar\vec{k}$ is its quantum mechanical momentum with the wavevector $\vec{k} = \{k_x, k_y, k_z\}$ related to the de Broglie wavelength of an electron λ by $k = |\vec{k}| = 2\pi/\lambda$. The resulting density of states ρ^{bulk} reads (see Fig. 1.2) [3]:

$$\rho^{bulk}(E) = \frac{1}{2\pi^2}(\frac{m^*}{\hbar^2})^{3/2}\sqrt{E - E_g}. \tag{1.2}$$

QW structure confines the charge carriers only in one dimension, i.e. in the growth direction, and they are still free to move in the plane of the layer. Such confinement, however, already puts constraints on the carrier wave motion across the well, so that we must fit in there an integral number n of half wavelengths (we assume infinite barrier height) [3]:

$$d = n\frac{\lambda}{2}. \tag{1.3}$$

Consequently, the wavevector for motion perpendicular to the plane of the QW, k_z, is given by:

$$k_z = \frac{2\pi}{\lambda} = n\frac{\pi}{d}. \tag{1.4}$$

Next, the energy spectrum of an electron in the conduction band becomes [3]:

$$E = E_g + \frac{\hbar^2}{2m^*}n^2\frac{\pi^2}{d^2} + \frac{\hbar^2}{2m^*}(k_x^2 + k_y^2). \tag{1.5}$$

The second term in Eq. 1.5 represents quantized confinement energy, whereas the third term is the kinetic energy for motion in the plane of the QW. Notice, that the band-edge is shifted to higher energy by $\frac{\hbar^2}{2m^*}\frac{(n\pi)^2}{d^2}$. Since this value depends on the thickness of the QW, one-dimensional confinement already gives possibility to tailor the emitted wavelength.

Bulk density of states splits into a series of discrete subbands in QWs, Fig. 1.2b, however, due to the free motion of carriers in the plane of the well each subband remains a continuum of states. The resulting density of states of QWs, ρ^{QW}, takes on a staircase like function given by [4]:

$$\rho^{QW} = \frac{m^*}{\pi\hbar^2}\sum_n \Theta(E - E_n), \tag{1.6}$$

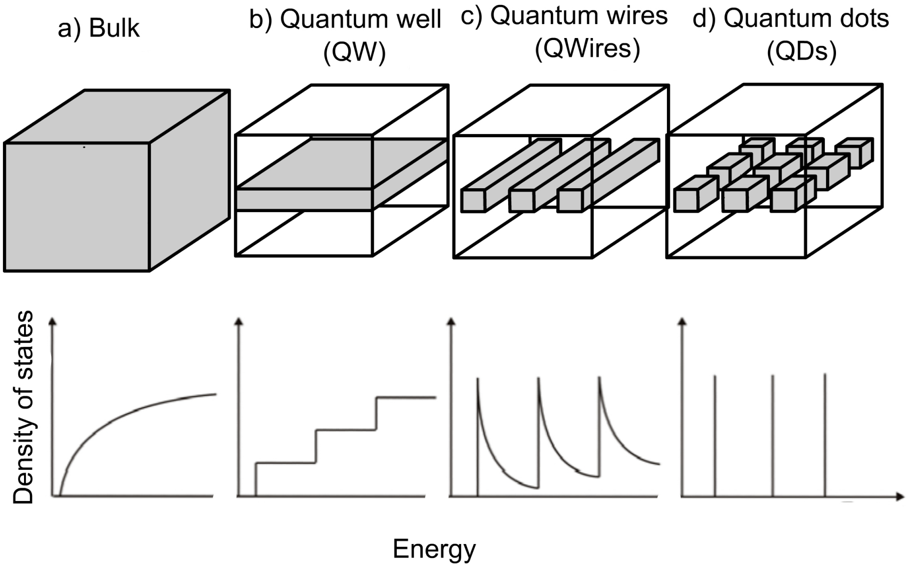

Figure 1.2: Schematic representation of the nanostructures and the corresponding density of states. a) Bulk, b) quantum well (QW), c) quantum wire (QWire), d) quantum dot (QD).

where E_n is the n-th energy level within the QW, while $\Theta(E - E_n)$ is the Heaviside function, i.e. it takes the value of zero when E is less than E_n and 1, when E is equal to or greater than E_n.

Further restriction of motion of carriers in two and three dimensions results in quantum wires (QWire) and quantum dots (QDs), respectively. In the former case the energy spectrum of an electron in the conduction band becomes [4]:

$$E = \frac{\hbar^2 \pi^2}{2m^*}(\frac{n_x^2}{L_x^2} + \frac{n_z^2}{L_z^2}) + \frac{\hbar^2}{2m^*}k_y^2 \tag{1.7}$$

and results in a density of states that is singular at the subband edges, see Fig. 1.2c [4]:

$$\rho^{QWire}(E) = \frac{1}{\pi\hbar^2}\sum_n \sqrt{\frac{m^*}{2(E - E_n)}}\Theta(E - E_n). \tag{1.8}$$

Here n_x and n_z are quantum numbers used to label respective energy levels. Note, that due to the free motion of carriers in the y-direction, the subbands in QWires still remain continuous bands. They become series of discrete states only in QDs, Fig. 1.2d. In this case the energy spectrum and the density of states read [4]:

$$E = \frac{\hbar^2 \pi^2}{2m^*}(\frac{n_x^2}{L_x^2} + \frac{n_y^2}{L_y^2} + \frac{n_z^2}{L_z^2}), \tag{1.9}$$

$$\rho^{QD}(E) = \sum_n 2\delta(E - E_n), \tag{1.10}$$

where δ is the Dirac delta function.

It is worth noticing that each additional quantization piles up the density of states into a narrower range of energies, meaning that more and more transitions can contribute to the emission at a given energy. This is very beneficial for semiconductor lasers. In particular, it can greatly improve their performance in terms of material gain, quantum efficiency, threshold current, output power. In this regard, QDs seem to be perfect because in their case all the carriers that reach QDs should emit photons at the same energy, in analogy to transitions between discrete levels of individual atoms. Ideal QD lasers would, therefore, provide huge material gain, posses ultra low threshold currents, be insensitive to temperature, exhibit zero-value of the linewidth enhancement factor. All these advantages, however, are based on the following assumptions [5]:

- lack of inhomogeneous broadening, meaning an ensemble of identical QDs;
- one confined electron and hole level with infinitely high barrier potential, meaning lack of thermal escapes of carriers;
- only bimolecular e-h recombination; meaning lack of nonradiative channels.

As we will show in the following sections, most of these assumptions are not fulfilled in actual structures.

1.2 Properties of actual QDs

1.2.1 Inhomogeneous broadening

To fully benefit from the δ-function like density of states of QDs, all QDs within a QD ensemble should be identical, that is, they should possess the same size, shape, orientation and composition [6]. It is, however, hardly possible to fulfill this requirement when dealing with millions of spontaneously grown nanostructures. Since the energy spectrum of a single QD is determined by its geometrical parameters, the emission spectrum of a QD ensemble will exhibit inhomogeneous broadening due to the dispersion of these parameters. In Fig. 1.3, QD diameter and height fluctuations are summarized by the respective histograms, which show that the size of QDs within an ensemble, and therefore the transition energy, follows a Gaussian distribution function G [8]:

$$G(E) = \frac{1}{\sqrt{2\pi}\zeta_0} \exp\left(-\frac{(E - E_{GS})^2}{2\zeta_0^2}\right), \tag{1.11}$$

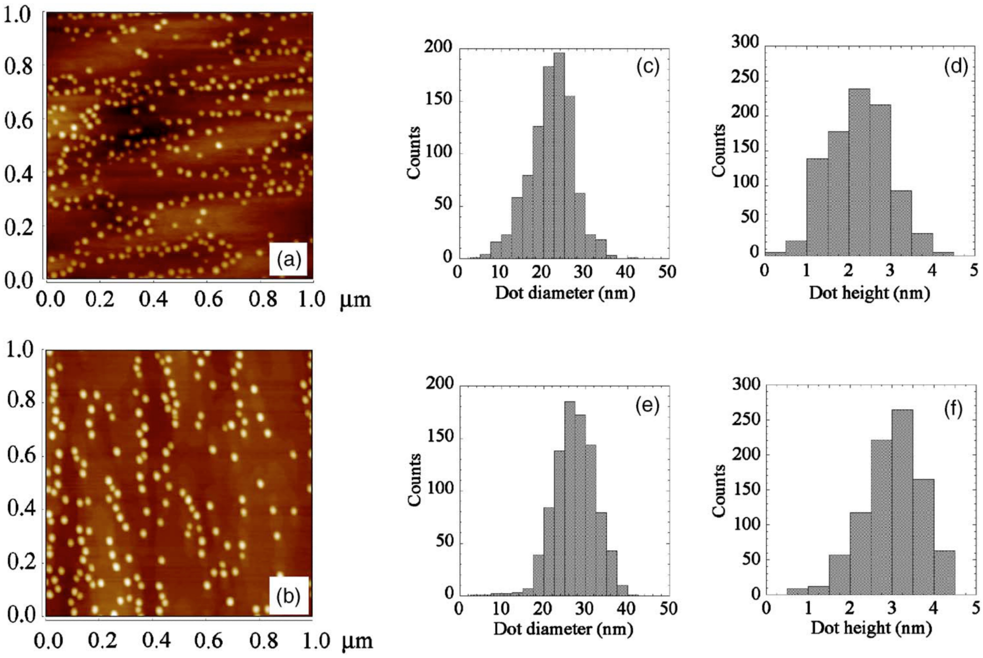

Figure 1.3: Plan views of the uncapped single layer QD sample a) and of the upper layer of the double stacked QD sample. The size and height histograms associated with each image are also shown in panels c-f [7].

which full-width at half maximum (FWHM) is given as $\Gamma_{IHB} = 2.35\zeta_0$ with ζ_0 being a standard deviation [8]. Here E_{GS} represents the ground-state transition energy. In [7] the diameter and height fluctuations have been estimated to be 21.9±5.2 nm and 2.2±0.7 nm, respectively, for a single layer sample and 27.4±4.9 and 3.0±0.7 nm for a stacked layer sample resulting in the FWHM of the photoluminescence (PL) peaks of 50-70 meV. Standard deviations of the diameter and the height of 3% and 4%, respectively, resulting in the FWHM of 35 meV have been reported for QDs formed under high growth temperatures [9]. In general, due to latest advances in the QD growth techniques the inhomogeneous broadening does not exceed 100 meV. The best uniformity with the FWHM of the PL spectra of a few tens of meV is achievable with QDs grown in submonolayer (SML) mode (see also Sec. 1.3.2) [10, 11, 12, 13].

1.2.2 Gain in lasers with self-organized QDs

If all QDs within an ensemble were identical, meaning no inhomogeneous broadening, the material gain provided by such an ensemble would be limited only by the homogeneous broadening resulting from a finite phase coherence time [5, 14], see Fig. 1.4. Such homogeneously broadened gain is commonly assumed to follow Lorentzian distribution L [8]:

$$L(E - E_{GS}) = \frac{\hbar\Gamma_{HB}/\pi}{(E - E_{GS})^2 + (\hbar\Gamma_{HB})^2}, \tag{1.12}$$

which FWHM is given as $2\hbar\Gamma_{HB}$ with Γ_{HB} being the phase coherence rate. With $\Gamma_{HB} = 1/150$ fs, as in [14], the FWHM amounts to 8 meV.

The resulting linear optical gain of the QD active region with a volume density of dots of N_{QD}^{3D} is given as [8]:

$$g^1(E) = \frac{2\pi e^2\hbar N_{QD}^{3D}}{cn_b\epsilon_0 m_0^2}\frac{|<\Psi_e|\Psi_h>|^2 M^2(f_c - f_v)}{E_{GS}}L(E - E_{GS}), \tag{1.13}$$

where f_c and f_v are the electron occupation probability for the conduction and valence band, respectively, M is the transition matrix element and $|\langle\Psi_e|\Psi_h\rangle|^2$ describes the overlap integral between the envelope of electron and hole wave functions. Under the assumption of charge neutrality in each QD [8] we have:

$$f_v = 1 - f_c. \tag{1.14}$$

Consequently, the difference $(f_c - f_v)$ in Eq. 1.13 becomes:

$$f_c - f_v = 2f_c - 1. \tag{1.15}$$

Due to a close proximity of electrons and holes in QDs it can be assumed that they are captured and emitted in pairs as excitons and, therefore, the occupation probability for electrons in Eq. 1.15 can be replaced by the occupation probability for excitons f_{ex}.

As already shown in Sec. 1.2.1, actual QDs exhibit dispersion of their geometrical parameters, which significantly broadens the gain spectrum. The resulting linear optical gain of such an ensemble can be expressed as [8]:

$$\begin{aligned} g^1(E) &= \frac{2\pi e^2\hbar N_{QD}^{3D}}{cn_b\epsilon_0 m_0^2}\frac{|<\Psi_e|\Psi_h>|^2 M^2}{E_{GS}} \\ & \int_{-\infty}^{+\infty}(2f_{ex}(E^{'}) - 1)G(E^{'} - E_{GS})L(E^{'} - E_{GS})\mathrm{d}E^{'} \end{aligned} \tag{1.16}$$

The existence of a large material gain in InAs/GaAs QD lasers has been verified in [15]. The value of 6.8×10^4 cm^{-1} at 77K turned out to be one order of magnitude larger than measured at the same conditions material gain of a QW laser with similar confinement size [15].

Although the material gain is indeed exceptionally large in QD lasers, the maximum modal gain of a single QD layer is in general limited to about 9 cm^{-1} in InAs [16] and 7 cm^{-1} in InP QD lasers [17]. This is due to a small value of the optical confinement factor Γ, defined as the ratio of the total volume of

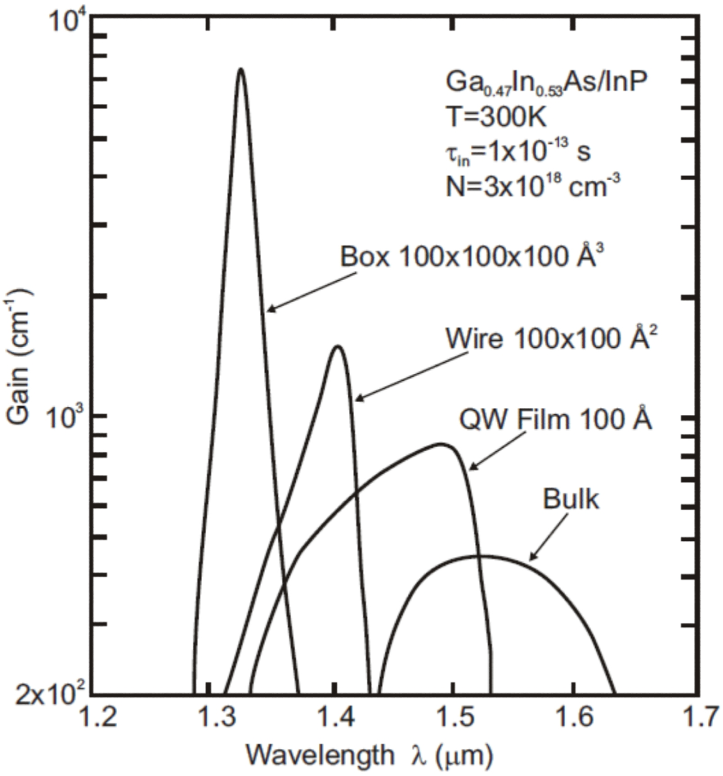

Figure 1.4: Theoretically calculated optical material gain for bulk material, QW, quantum wire, and QD. Taken from [6].

the QDs in the active region to the total volume of the cavity. Γ can be split into an in-plane Γ_{xy} and vertical Γ_z component as [18]:

$$\Gamma = \Gamma_{xy}\Gamma_z, \tag{1.17}$$

with Γ_{xy} given by:

$$\Gamma_{xy} = \frac{N_{QD}^{2D} A_{QD}^{xy}}{A} = \varsigma. \tag{1.18}$$

In Eq. 1.18, ς is the areal coverage, A_{QD}^{xy} is the average in-plane area of a single QD, whereas A is the area of the active region.

The vertical component Γ_z of the confinement factor characterizes the overlap between the QDs and the optical mode [18]. Typical value of Γ_z for a single layer of QDs and a 150 nm thick cavity is 7×10^{-3} [18]. Putting this value into Eq. 1.17 and assuming $\varsigma = 0.02$ (after [18]) we obtain the optical confinement factor being as small as $\Gamma = 1.4 \times 10^{-4}$. Modal gain can be increased by increasing the areal density of QDs or by increasing the number of QD layers. Both approaches have been successfully verified experimentally [16, 19].

It should be noted that although in the vast majority of cases the inhomogeneous broadening has negative impact on the performance of QD lasers, a certain minimum gain bandwidth is required to maintain overlap of the gain spectrum and the cavity resonance over a useful range of temperatures and currents.

1.2.3 Excited states

Prospective benefits of QDs are based on the assumption that there exists only one confined energy level for electrons and one energy level for holes in QDs [20], the so-called ground state. Photoluminescence measurements, however, show in general multiple energy levels that are inhomogeneously broadened due to nonuniform size distribution of QDs [21, 22], see Fig. 1.5. Also theoretical band structure calculations show multiple energy levels in both the conduction and the valence bands [23, 24]. Such multiple energy structure limits the performance of QD lasers. In the first place it opens potential channels for thermally induced escape of carriers from the ground-state and, therefore, reduces the differential gain and temperature stability. Furthermore, it slows down the intradot dynamics and consequently limits the modulation bandwidth. Finally, it breaks the symmetry of the gain spectrum and, therefore, increases the linewidth enhancement factor.

The energy and degeneracy of the respective energy levels depend on the size and shape of QDs [26]. In a cubic box approximation the ground and the first excited states are two-fold and six-fold degenerate, respectively. Consequently, such a QD can be regarded as an atom with two-fold degenerate S state and six-fold degenerate P state [27]. For circular and elliptical QDs, however, energies of single particle states are given by [28]:

$$E_{nl} = (2n + |l| + 1)\hbar\omega_0, \tag{1.19}$$

where $n = \{0, 1, 2, ...\}$ is the radial quantum number, $l = \{0, \pm1, \pm2, ...\}$ is the angular momentum quantum number and $\hbar\omega_0$ is the confinement energy. Each state is additionally two-fold degenerate due to the spin. Consequently, the lowest energy state $(n, l) = (0, 0)$ can accumulate two electrons, the first excited level can in total accumulate four electrons, i.e. $(n, l) = (0, 1)$ and $(0, -1)$, and so on [28]. This is consistent with experimental findings [24, 26, 29]. Consequently, in majority of rate-type models, QDs are represented by a two-energy level system comprising a ground state and a two-fold degenerate excited state coupled to a quasi-continuum of states associated with the wetting layer [30, 31].

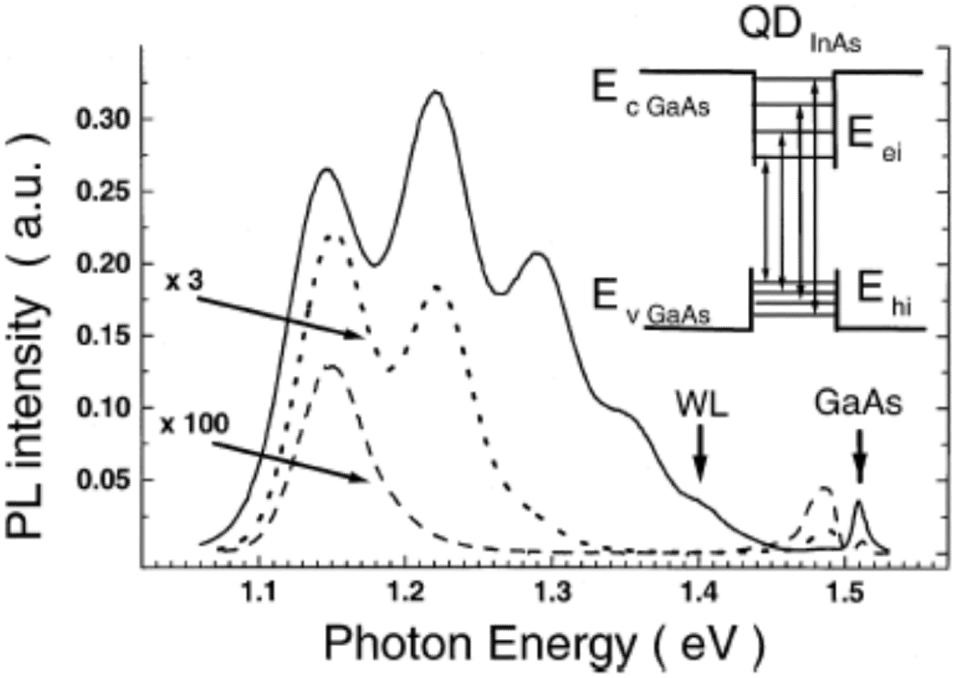

Figure 1.5: Photoluminescence spectra of the QD structure measured at T = 10K for various excitation powers. Taken from [25]

1.2.4 Capture and relaxation processes

The discrete energy spectrum of QDs puts constraints on the allowed relaxation mechanisms. In particular, single longitudinal-optical (*LO*) phonon emission is forbidden unless the energy levels within a single QD are separated by exactly the *LO*-phonon energy (e.g. 32 meV for InAs [32]). Lack of this relaxation channel, commonly referred to as phonon bottleneck, was expected to cause a strong increase of the carrier relaxation scattering time to nanoseconds [33]. Detail experimental investigations by means of time-resolved photoluminescence spectroscopy and ultrafast differential transmission spectroscopy showed however, that the relaxation time apparently does not exceed few tens of picoseconds [34, 35]. Several mechanisms have been proposed to explain such behavior such as Auger-type processes [32, 35, 36], multiphonon processes [35, 37] and defect-assisted phonon emission [38]. Multiphonon processes have been shown to dominate at low excitation densities [35], whereas Auger processes dominate at high excitation densities [35], with electron-electron scattering governing electron capture from the wetting layer into the QD excited state and electron-hole scattering efficiently relaxing electrons from the excited to the ground state [32].

Capture of carriers into the QDs is in general slower than the intradot relaxation but still takes place on the picosecond time scale [34, 35, 39, 40]. Thermally induced escape of carriers from QDs, in turn, occurs at a slow time scale up to few hundreds of picoseconds [40, 41].

Due to a smaller effective mass, energy level separation for electrons in the conduction band is considerably larger than the energy level separation for holes in the valence band. The latter energy is of the order of k_BT and as a result the capture, relaxation and escape rates for holes are much faster than the respective values for electrons. It can, therefore, be assumed that the overall dynamics is governed only by electrons. This is even more true for p-doped QD lasers.

1.2.5 Temperature stability

Temperature stability of a laser is described by the so-called characteristic temperature T_0, which fits the temperature dependence of the threshold current by exponential expression:

$$J_{th}(T) \propto \exp \frac{T}{T_0}. \tag{1.20}$$

In ideal case of temperature insensitive laser T_0 should be infinite. In QD lasers this would be possible only if all the injected carriers contributed entirely into the radiative recombination in QDs (only bimolecular e–h recombination), meaning lack of thermally induced escape of carriers to the excited states, and lack of non-radiative recombination. In actual QD lasers these requirements are satisfied only at low temperatures when the escape rates are much smaller than the radiative lifetime [42, 43, 44]. In such a case redistribution of carriers from one QD to another and establishment of quasi-Fermi levels for the charge carriers do not occur leading to nonequilibrium filling of QDs. Since the initial number of carriers captured into various QDs is the same, the contributions of individual QDs to the lasing also are the same [45].

At higher temperatures thermal excitation of carriers to the excited states is more probable leading to redistribution of carriers from one QD to another and eventually to the establishment of quasi-equilibrium distributions with the corresponding quasi-Fermi levels [45]. In such a case the occupation of the respective energy levels changes from QD to QD [45]. In addition, in order to maintain threshold gain the pump current needs to be increased so that the thermal escapes are balanced. This mechanism is directly responsible for a reduction of T_0 in QD lasers.

1.2.6 Linewidth enhancement factor

In semiconductors both the refractive index and absorption/gain depend on the frequency and on the carrier density N. Indeed, every change in the number of carriers injected into the active region influences the gain value.

Through the Kramers–Kronig relation, a variation of the gain leads to a variation of the refractive index and, therefore, modifies the cavity resonance frequency. In other words, changes in the carrier density result in the phase - amplitude coupling. The strength of such a coupling is described by the linewidth enhancement factor (α).

For a given frequency, α-factor is defined as the ratio of the partial derivatives of the real and imaginary parts of the complex susceptibility ($\chi = \chi_{RE} + i\chi_{IM}$) with respect to the carrier density:

$$\alpha = -\frac{\partial \chi_{RE}/\partial N}{\partial \chi_{IM}/\partial N} \tag{1.21}$$

Alternatively, the α-factor can be expressed by the ratio of the refractive index change to the optical gain change with respect to the carrier density or simpler by the ratio of the differential refractive index to the differential gain:

$$\alpha = -\frac{4\pi}{\lambda}\frac{\partial \delta n/\partial N}{\partial g/\partial N}. \tag{1.22}$$

The α-factor is a very important parameter of semiconductor lasers. In the first place, it is responsible for the linewidth broadening with respect to the linewidth of gas lasers given by Schawlow-Townes formula [46]. Next, it is a source of the chirp under direct modulation [47, 48] and filamentation in broad-area devices [49]. It also has a great impact on the dynamics of semiconductor lasers subject to optical injection [50] or optical feedback. In majority of application it is desirable to have α-factor equal to zero. If successful, it would be possible to get rid of expensive external modulators and optical isolators from the optical systems.

Small values of the α-factor have been expected for QD lasers, owing to their high differential gain and symmetric gain spectrum which, in turn, arises from the delta function like QD density of states. To highlight the potential advantages of QD lasers over their QW counterparts we show in Fig. 1.6 the gain and the carrier-induced change of the refractive index for a QD laser and for a conventional QW laser. Let us assume that the QD ensemble constituting the active region of the investigated QD laser shows a perfect Gaussian energy distribution and that there is only one energy level for electrons and holes, i.e. the ground state with the energy of E_{GS}. Under such conditions the gain spectrum is perfectly symmetric around E_{GS}. If the cavity resonance frequency Ω_{cav} equals the peak gain energy then the carrier-induced change of the refractive index is exactly zero, meaning $\alpha = 0$. However, when the cavity resonance is detuned from E_{GS}, every change of the carrier density will result in a change of the refractive index and, therefore, the value of the α-factor will become different from zero. Note that in such a two-level system injected carriers do not shift the peak gain energy, hence the α-factor can be

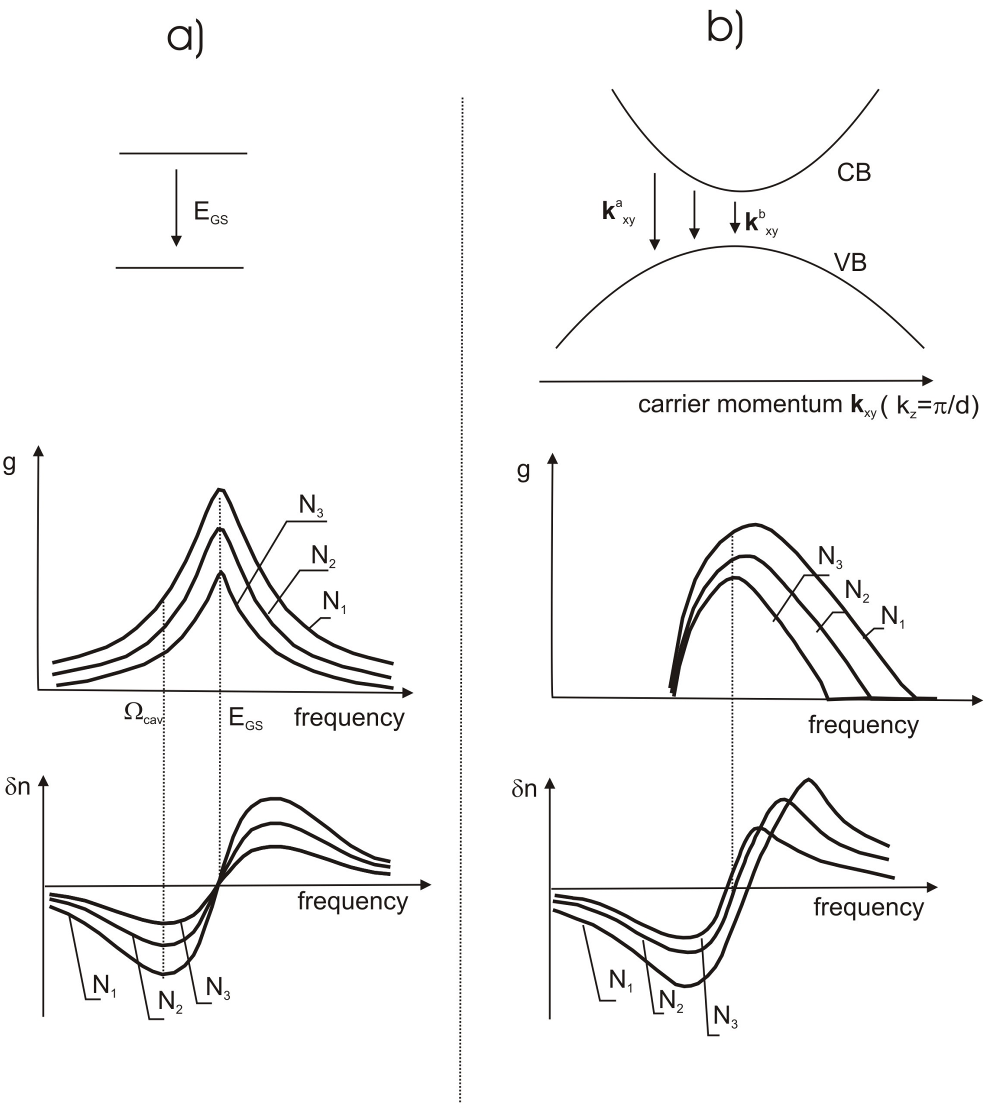

Figure 1.6: Gain and carrier-induced ($N_1 > N_2 > N_3$) change of the refractive index for A: QD laser and B: conventional QW laser.

considered as a detuning [46]:

$$\alpha = \frac{\Omega_{cav} - E_{GS}}{\gamma_\perp}, \tag{1.23}$$

where $\gamma_\perp$ is the polarization decay rate. For a positive detuning the refractive index increases with the number of carriers while for negative detuning it decreases. The latter effect is commonly referred to as carrier anti-guiding.

In a conventional QW laser the gain spectrum can be regarded as a collection of coupled two-level systems, each with slightly different transition energy corresponding to distinct values of the in-plane wavevector $\vec{k}_{xy}$, e.g. k^a_{xy}, k^b_{xy} in Fig. 1.6-B, within a given subband. The gain spectrum resulting from a superposition of a number of Lorentzian curves corresponding to these wavenumbers [46] is very broad and asymmetric. Moreover, the injected carriers blueshift the peak gain energy. Since the carrier-induced changes of the refractive index occur even at the peak gain energy, typical values of the α-factor for QW lasers are different from zero and lie in the range 0.5–8 (see [51] and references therein). Experimental values for actual QD lasers are quite diversified. On the one hand side, there are reports showing that, indeed the α-factor is very small, e.g. α=0 in [52], 0.1 in [53], 0.15 in [54], 0.5 in [55]. On the other hand, due to the QD size inhomogeneity and contributions from the excited states the values of the α-factor can be similar to those of QW lasers [56, 57], and even substantially larger reaching $\alpha = 57$ in [58]. This shows, that apparently the α-factor of QD lasers depends on the operation conditions [59].

1.3 QD lasers

1.3.1 Edge emitting and vertical-cavity surface emitting lasers

In any laser system there are two fundamental requirements that need to be fulfilled in order to have stimulated emission, namely an active region and a positive optical feedback. The active region is responsible for amplification of light, whereas the positive feedback determines the emitted frequency. In semiconductor lasers there are two approaches to achieve the conditions of stimulated emission, each associated with different laser geometry so that the light is emitted either from the edge of the active region – like in the edge-emitting lasers (EEL), or from the surface that is parallel to the surface of the active region – like in the vertical-cavity surface-emitting lasers (VCSELs). Both geometries are schematically shown in Fig. 1.7.

In EEL the light propagates along the active region, which extends over the whole length of the cavity. Since the light is continuously amplified, the provided gain is sufficient to obtain lasing action with only a weak positive feedback realized by cleaved wafer facets giving reflectivity of 30% [60, 61]. This is not the case in VCSELs where the light propagates in the direction perpendicular to the area of the active region, which occupies only a tiny part of the dissipative cavity [62, 63, 64, 65, 66]. As a result, single roundtrip gain is not sufficient to balance the losses of the cavity and strong positive feedback is crucial to obtain lasing action. The required reflectivity, of over 99%, can be achieved with Distributed Bragg reflectors (DBR) formed by stacks of 20-40 pairs of quarter-wavelength-thick layers with alternating, high-low refractive indices. The circular symmetry and vertical emission, that are characteristic for VCSELs, offer a number of advantages such as a circular

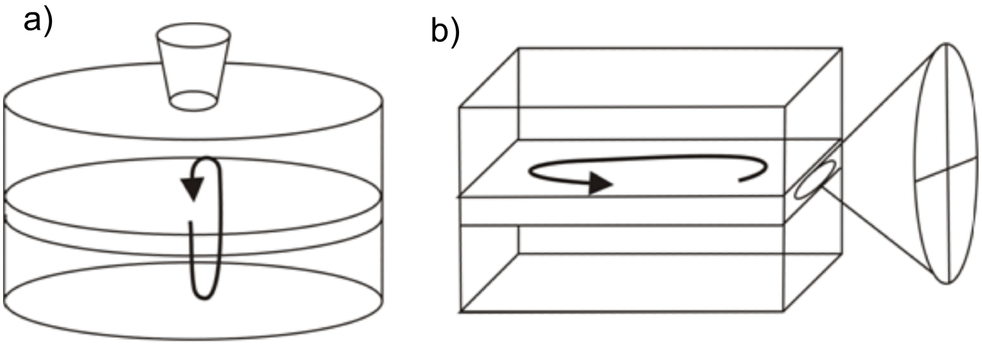

Figure 1.7: Schematic view of a) a vertical-cavity surface-emitting (VCSEL) and b) edge-emitting (EEL) laser.

output beam with low divergence (which can be efficiently coupled into an optical fiber), a possibility to fabricate two-dimensional arrays and to test the devices while on the wafer, a simplified post-processing after separation from the wafer and suitability for simple packaging so that the high volume cost can be very competitive. In addition, the very short cavity supports only one longitudinal mode [67] (though depending on the operation conditions the laser may support the emission of many higher-order transverse modes [68, 67, 69, 70]), whereas the relatively small volume of the active region helps to reduce the threshold current densities [66].

As a general rule of thumb, the symmetry of a laser influences its polarization properties. For instance, due to the highly anisotropic shape of the cavity, EELs emit linearly polarized light which direction is parallel to the active region [67]. In ideal VCSELs, however, the transition strength in the plane of the active region is the same for all directions [71] hence in a devices with perfectly cylindrical symmetry there is no a priori polarization selection mechanism. In real devices a small unintentional structural anisotropy introduced during the fabrication process leads to the existence of two preferential orthogonal polarization axes [72, 73]. Unless special precautions are taken to stabilize the polarization, real VCSELs can exhibit polarization instabilities when changing its operation conditions such as pump current or temperature [73]. Polarization properties of VCSELs are discussed in more details in Chap. 3.

1.3.2 Stranski-Krastanov (SK) and submonolayer (SML) QDs

Self-assembled growth of QDs occurs if there is a large mismatch between the lattice constants of the substrate and the deposited layer materials. For instance, the lattice mismatch between GaAs (5.6533 $\mathring{A}$) and InAs (6.0583 $\mathring{A}$) is of 7 %. We limit the description of the growth modes to Stranski-Krastanov

(SK) and submonolayer (SML) ones. As it is shown in Fig. 1.8, in the SK mode the growth of InAs on GaAs (001) proceeds first by the formation of a strained quantum well, the so-called wetting layer (WL). After reaching its critical thickness, i.e. 1.7 monolayers (ML), the accumulated strain relaxes by the formation of three-dimensional islands - quantum dots. This mode has also been demonstrated for InGaAs on GaAs, InP on GaInP and GaN on AlN.

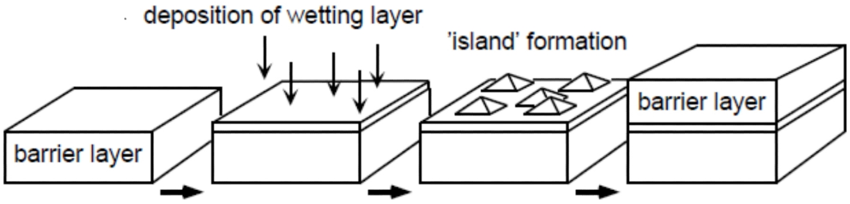

Figure 1.8: Schematic representation of Stranski-Krastanov growth of quantum dots. The QDs (shown as small pyramidal 'islands') grow spontaneously from on the deposited wetting layer due to strain relaxation. Taken from [74]

In SML mode there in no wetting layer. InGaAs QDs are grown by a deposition of a superlattice consisting of thin layers of binary InAs and GaAs but not by a deposition of an InGaAs ternary alloy as in SK mode. For instance, in [75] 0.5ML InAs deposition cycles separated by 2.3ML GaAs were used. With these parameters, conventional continuous-mode deposition would result in uniform quantum well. The distribution of InAs however, is nonuniform which results in the formation of the InAs-rich regions. After the deposition of GaAs, the deposition of the next InAs submonolayer is affected by the nonuniform strain distribution caused by the underlying InAs islands [75]. Because of the large amount of GaAs within the range of confined charge carriers, SML mode is better suited for short wavelengths. SML-QD lasers emitting near 0.94-0.98 μm were successfully demonstrated in [52, 75] with much improved uniformity of the QD ensemble resulting in narrower gain spectrum (FWHM of the gain spectrum of around 26.7 meV, which is two to three times better than that of typical SK InAS/GaAs QDs [7, 76]). Furthermore, good thermal stability together with higher areal density of QDs, reaching 1×10^{11} cm^{-2} in [52], and consequently higher maximum modal gain of a single QD layer of about 44$\pm$3 cm^{-1} [52] make SML-QDs suitable for high-speed VCSELs. Such devices, with the modulation bandwidth of 10.5 GHz, have already been demonstrated in [75].

1.3.3 Characteristics of QD lasers

Issues presented in this dissertation are focused on InGaAs-GaAs QD lasers. First such devices in edge-emitting geometry were fabricated in 1994 and already revealed some of the features expected from three-dimensional confinement, especially in terms of high characteristic temperature T_0 [42]. The value of $T_0 = 330$K was limited, however, only to low temperatures in the range of 77-140K and dropped to $T_0 = 120$K in the range 150-300K. This dramatic decrease of T_0 was attributed to thermal escape of carriers from QDs showing that actual QDs are much more sophisticated than it is assumed in the model with infinite barriers and single confined energy level for electrons and holes. The resulting threshold current density at room temperature was 1 kA/cm^2. This value was reduced to 650 A/cm^2 [77] and 500 A/cm^2 [78] in 1996 and reached 19 A/cm^2 [79] by 2000. The most common approach to increase the characteristic temperature at room temperature was based on p-type doping of QDs. Its effectiveness was confirmed in [43] reaching $T_0 = 213$K in the range of 273-354K. As it is shown in Fig. 1.9, when the doping level increases the characteristic temperature rises and the range of temperature stability for the threshold current density broadens [44]. In a laser with 2×10^{12} cm^2 acceptors per QD layer, the characteristic temperature in the range 288-348K is as large as 1200 K [44]. It should be noticed however, that p-doping have also disadvantages including an increase of the threshold current density and decrease of the differential quantum efficiency, both related to the larger absorption by free carriers in doped structures as compared to undoped ones [44].

Having technology for low threshold and temperature-stable devices, engineers have moved to the development of GaAs-based QD lasers operating at 1.3 μm and even 1.5 μm, i.e. wavelengths relevant for datacom and telecom applications. Until recently, these wavelengths have only been available with structures grown on InP substrates, which provide inferior to GaAs thermal properties and suffer from the lack of lattice-matched semiconductors with a sufficient refractive index step for high quality DBR mirrors required for VCSELs. A natural peak emission wavelength of self-assembled InGaAs SK-QDs is around 1150-nm [19], but it can be extended toward 1.3 μm by overgrowing the QD layer with a thin InGaAs one [80] or by growing QDs within a InGaAs quantum well (so-called DWELL structure) [81]. Capping InAs QDs with a strain-reducing InGaAs layer has also been used to further extend the emitted wavelength toward 1.5 μm. The PL peak of such InAs QDs can then be controlled by the indium composition of InGaAs layer [82]. Lasing at 1.5 μm has been successfully demonstrated in [83], where few layers of InAs QDs overgrown by a thin InGaAs layer were settled in a thick metamorphic buffer. At the moment, however, such devices possess high threshold current densities of 1 kA/cm^2. It has been shown, that application of GaAsSb capping would extend the emission of InAs QDs even to 1.6 μm, making use of a type-II

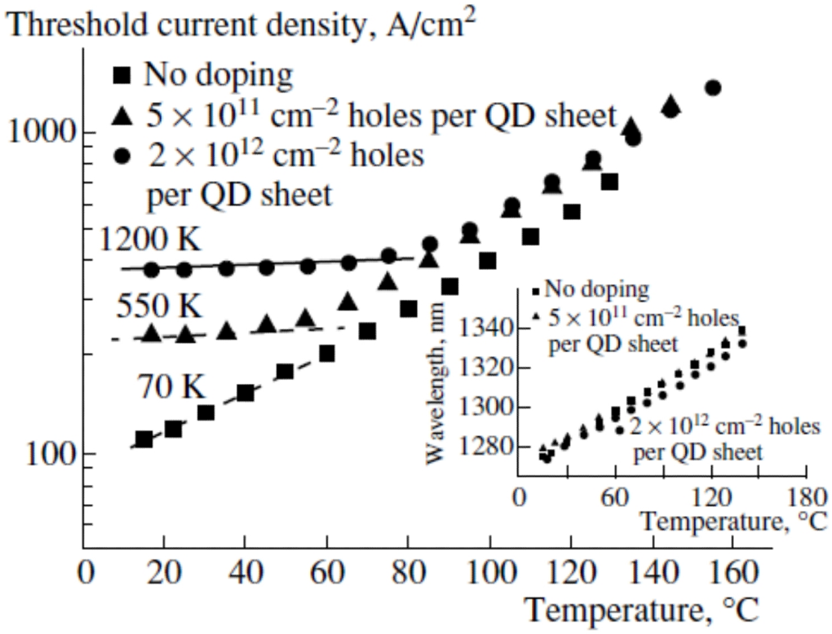

Figure 1.9: Temperature dependence of the threshold current density for the three heterostructures with different p-doping levels. Inset: temperature dependencies of lasing wavelength. Figure taken from [44].

transition between an electron state in the InAs QDs and a hole state in the GaAs Sb capping layer. The prospects for using such structures to fabricate 1.5 μm lasers are discussed in [84].

As it has been shown in Sec. 1.2.2, owing to the reduced optical confinement factor, the modal gain of QDs is in general smaller when compared to QWs. Since in VCSELs the active region, where the light is amplified, occupies only a tiny part of the dissipative cavity, small modal gain of QDs can be insufficient to achieve lasing action. This already shows that lasing from QDs in vertical-cavity geometry is quite challenging. Specifically, the design of a structure providing minimal losses is of particular importance. First QD-VCSEL operating at room temperature through current injection was grown using conventional molecular beam epitaxy (MBE) and demonstrated in 1996 [85]. To achieve sufficient modal gain its active region consisted of 10 periods of In$_{0.5}$Ga$_{0.5}$As QDs with a photoluminescence peak at 1000 nm (at RT) comparable in intensity to the one typically achieved with triple QWs. The devices with 25 × 25 μm square aperture exhibited rather poor electrical characteristics, i.e. large value of the threshold current of 32 mA and of the threshold voltage of 5 V (for ideal structure the threshold voltage for λ = 960 nm is around 1.3 V). In addition, the relatively broad photoluminescence spectrum of 100 meV suggests large size nonuniformity of QDs within the ensemble. The authors also pointed to the contributions of the excited states resulting in the operation at the energy well above that of the ground-state transitions. Improvement in the performance of QD VCSELs required optimization of their structures and, indeed, the threshold current of devices based on oxide-confined design has been reduced below 1 mA [86]. As in the case of edge emitting QD lasers, after manufacturing QD VCSELs operating in continuous wave regime at room temperature, engineers have moved to the development of GaAs-based devices operating at 1.3 μm and grown in MOCVD [19, 87]. Until now, however, characteristics of long wavelength QD lasers grown using MOCVD remain worse than those grown in MBE.

1.4 Scope of the thesis

In this thesis, we first investigate experimentally polarization properties of QD VCSELs. Even though polarization properties of QW VCSELs are quite diversified and have been extensively studied both theoretically and experimentally, the case of QD VCSELs definitely lacks considerable investigations. Basically, these issues are interesting from theoretical point of view, because they can give better insight into the light-matter interactions at a nanoscale level. The rising significance of QD VCSELs for datacom and telecom markets shows, however, that polarization properties of these devices are also of practical importance.

Polarization instabilities of QW VCSELs are in general perceived as their major weakness. This is due to the fact that in many optical systems containing polarization-sensitive elements such instabilities are unacceptable. Interestingly, first experimental studies on polarization of QD VCSELs have shown improved polarization stability, which has been attributed to a relatively large dichroism of structurally anisotropic QDs [88]. This shows that structural properties of QDs influence polarization properties of QD VCSELs and, therefore, one can expect that dispersion of these parameters may be critical for polarization stability. The devices investigated in [88], however, operated only in pulsed regime, i.e. without overheating, whereas it has been shown for QW VCSELs, that polarization properties of VCSELs can be greatly affected by temperature. Our main motivation, therefore, is to study polarization properties of QD VCSELs operating in continuous wave regime at room temperature, i.e. conditions comparable to those necessary for high-speed applications. In our experiment we will investigate two generations of QD VCSELs, namely SK-QD VCSELs grown using MOCVD and SML-QD VCSELs grown using MBE. We will put attention to all kinds of polarization instabilities, that have been reported for QW VCSELs, namely polarization switching and polarization mode hopping.

In this thesis we also investigate dynamical properties of QD lasers subject to optical injection, i.e. an extra light injected to the QD slave laser cavity from external, master laser. In QW lasers this technique has been shown to be an attractive configuration for the fundamental study of nonlinear optical systems [50, 89, 90] and provides the potential means of improving laser performance in terms of its stability, linewidth and modulation bandwidth [91, 92, 93]. We suspect that distinct characteristics of QDs lasers as compared to their QW counterparts, namely the smaller linewidth enhancement factor [56], and strongly damped relaxation oscillations [94], i.e. factors that normally play a major role in nonlinear dynamics of semiconductor lasers, may result in new dynamics, different from those found for QW lasers. First experimental studies on optically injected QD lasers reveal, for instance, the existence of regions in the injection-parameter space (defined by the frequency detuning from the slave laser frequency and the injection strength), where the laser responds to the injected optical signal in a form of single or double excitable pulses [95]. Although excitability is quite common in nature and has already been reported for a variety of laser systems including lasers with optical feedback [96], [97] and lasers with saturable absorber [98], it was the first experimental observation of such a dynamics in optically injected system.

To better understand the overall dynamics of the system we want to dive into the physics of QDs. One of the features that distinguishes QD lasers from their QW counterparts is the more complicated dynamics of carriers, which being captured from the wetting layer into the dots achieve lasing states by successive transitions through excited states. This processes are characterized by the capture and the relaxation time, respectively. Both time constants have been shown to influence the performance of QD lasers in terms of modulation bandwidth and threshold current [57, 99, 100]. We, therefore, want to check the impact of the two time constants on the dynamics of optically injected QD laser. To answer this question we will extend the model presented in [95] to account for the excited states and then we will map the bifurcations of the system in the plane detuning vs. injection strength. We put special attention to dynamics resulting in pulsed output, i.e. excitability and self-pulsations, which, if fast enough, can have many potential applications ranging from medicine to telecom. In particular, we want to show how the dynamics of these self-pulsations is influenced by the spontaneous emission noise and the injection parameters. Finally, we want to utilize such self-pulsations for all-optical signal regeneration. In our simple approach the attenuated/distorted information signal acts as a master laser that switches the QD slave laser between the regions of locking and self-pulsations.

The dynamics observed in optically injected QW laser system are usually modeled by single-mode rate equations [50]. There are however circumstances in which multimode dynamics has to be taken into account. A good example is polarization dynamics of VCSELs where each single-transverse mode is associated with two orthogonal, linearly polarized modes with frequency splitting of a few GHz. Comprehensive study of bifurcations in a model of a two-polarization mode VCSEL subject to orthogonal optical injection (polarization of the injected light is orthogonal to the one of the solitary VCSEL mode) has been presented in [90, 101, 102]. It unveiled bifurcations beyond those found in the single-mode model such as Hopf bifurcation on a two-mode solution and transcritical bifurcation between two-mode and single-mode solutions [101]. Another example is an EEL supporting emission of two longitudinal modes with THz frequency spacing achieved by special cavity design [103]. Optical injection in such a two-color laser revealed the importance of torus bifurcation in the route to two-mode antiphase dynamics with short-pulse packages and optical chaos.

In QD lasers the finite number of QDs within the active region and the discrete energy structure of QDs can lead to saturation of the ground state already at moderate currents. As a result, the occupation of the excited states grows with the current and the laser can start to lase from these states too. Simultaneous emission from both states has been demonstrated for a solitary QD laser in [31, 58, 104]. It has also been studied for a QD laser subject to optical feedback [105] and for dual-wavelength mode-locking [106]. In this thesis we undertake theoretical study of nonlinear dynamics induced by optical injection in such a two-mode QD laser system. Contrary to the case of multi-mode QW EEL [103], in our QD laser model different modes are associated with separate reservoirs of carriers, corresponding to the ground and excited states. These reservoirs are coupled through the relaxation process and are filled up in a cascade manner with different rates determined by the relaxation and capture rates. Oscillations of the ground state occupation caused by optical injection will, therefore, lead to modulation of the relaxation rate and, consecutively, to oscillations in the occupation of the excited state. Ultimately, such modulation can provide a gain switching mechanism and leads to emission of picosecond pulses or short-pulse packages from the excited state.

Chapter 2

Polarization properties of QD vertical-cavity surface-emitting lasers (VCSELs)

2.1 Polarization properties of quantum well (QW) VCSELs

2.1.1 Polarization instabilities in QW VCSELs: Experimental background

Owing to the symmetry of the atomic structure, the in-plane gain (i.e. the gain for light polarization in the plane of the active region), of QW VCSELs grown on (001) substrates is isotropic [71]. Cylindrical symmetry of VCSELs does not break this isotropy and, as a result, in such ideal VCSELs there is no intrinsic polarization selection mechanism such that the laser emits an arbitrary polarization state, i.e. linear, circular, elliptical with an arbitrary orientation in the plane of the active region.

Experimental studies however, show that real QW VCSELs emit linearly polarized light [67, 73, 107]. Although its direction, indeed, slightly changes from device to device, it is usually aligned with the [110] or [1-10] crystallographic axes [67, 107, 108, 109, 110]. This induced anisotropy has been attributed to a birefringence introduced during manufacturing and/or caused by electro-optic effect in the cavity and in the mirrors [111]. Ultimately, each single-transverse mode is associated with two orthogonal, linearly polarized (LP) modes. Due to the existing birefringence their frequencies are split up to a few tens of GHz [73, 109, 112]. Moreover, under given operation conditions only one of them is lasing, whereas another one is suppressed [67, 73, 107, 108, 112].

The most intriguing property of QW VCSELs, however, is that changes in the operation conditions, i.e. pump current or substrate temperature, can destabilize their polarization so that the laser emission switches abruptly to the suppressed LP mode [67, 107, 109]. This phenomenon is commonly referred to as polarization switching. Experimental polarization resolved power-current characteristics at three different substrate temperatures are shown in Fig. 2.1.

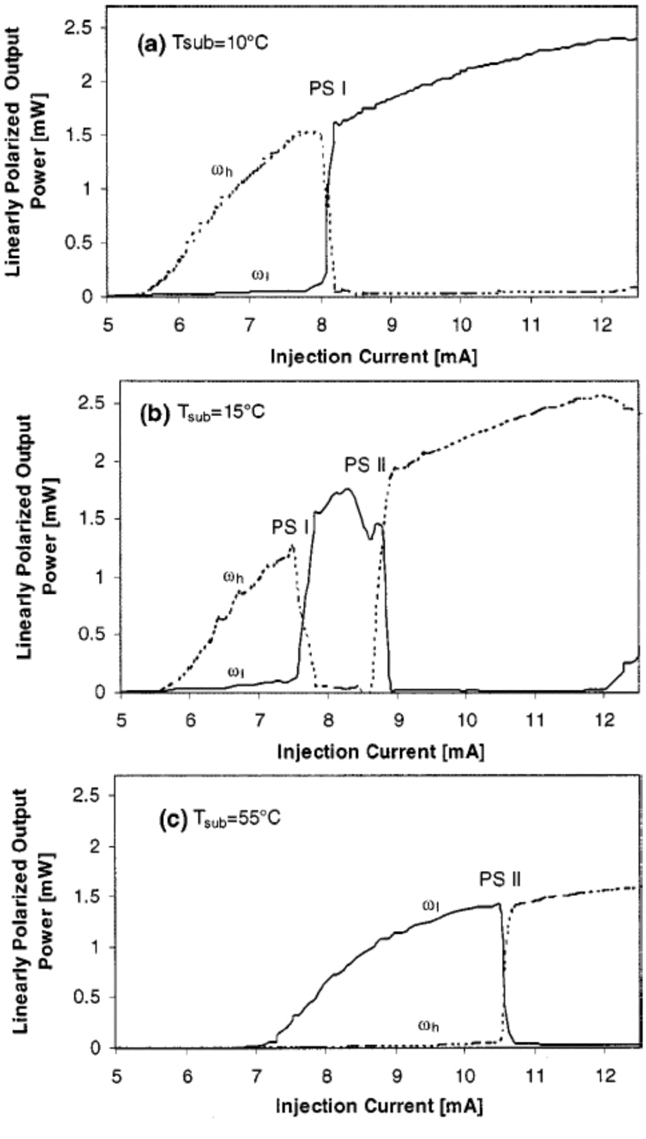

Figure 2.1: Polarization resolved power-current characteristics of a proton implanted VCSEL at different substrate temperatures. Taken from [109].

In Fig. 2.1a, close to the lasing threshold the laser emission is associated with the high-frequency ω_H LP mode however, when the current is increased the laser switches abruptly to the orthogonal low-frequency ω_L one. Such behavior is classified as type-I polarization switching [109]. In polarization switching of type-II [109], the laser first emits at the low-frequency LP mode and then switches to that of higher frequency as in Fig. 2.1c. It also happens that both types of switching occurs consecutively as in Fig. 2.1b.

Polarization properties of QW VCSELs also are influenced by a material strain. Indeed, it changes the lattice constants, alters the band structure and lifts degeneracies, and finally reduces the symmetry of the crystal. Moreover, as experimentally shown in [110, 111, 113, 114] changing the magnitude and/or the orientation of an externally induced in-plane anisotropic strain influences the presence of polarization switching, the current at which this phenomenon occurs and the frequency splitting between the LP modes. This experiment also shows, that unlike the frequency splitting, the gain difference between the LP modes depends on the pump current and achieves its minimum exactly at the switching point. Interestingly, as shown in Fig. 2.2, the increase of the applied stress can induce hysteresis in polarization resolved power-current characteristics, so that forward and backward sweeping of the pump current results in polarization switching events occurring at different currents.

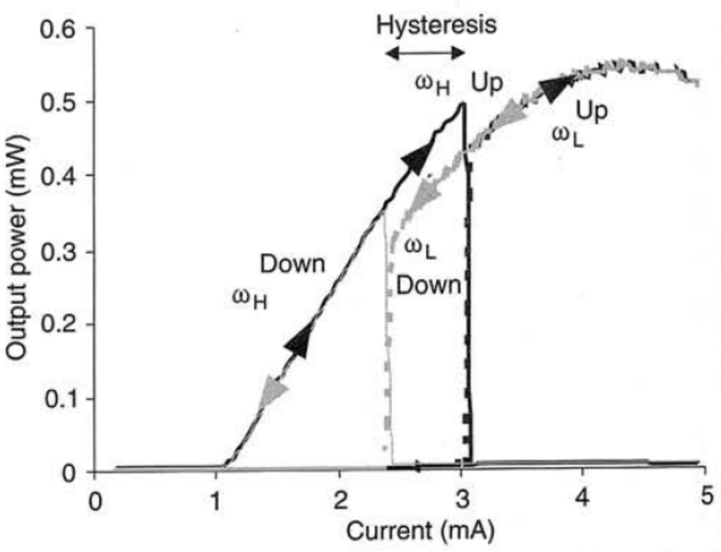

Figure 2.2: Polarization resolved power-current characteristics for the forward and backward current scans, showing polarization switching through a large hysteresis region [73].

Abrupt polarization switching is sometimes accompanied by a noise driven hopping between the two LP modes. This issue is discussed in more detail in

Chap. 3.

2.1.2 Polarization instabilities in QW VCSELs: Theoretical background

Theoretical models that have been proposed to explain polarization switching in QW VCSELs can in general be divided into two groups. The first one, focused around the spin-flip model (SFM) [115, 116], accounts for the angular momentum of the quantum states involved in the process of light emission, spin dynamics and nonlinear light-matter interactions governed by the linewidth enhancement factor. In this model, different polarizations of light are associated with different spin sublevels. It also assumes that splitting between the heavy-hole and light-hole states in the valence band is large so that the latter can be neglected. Consequently, the active region is represented by a four-level system with electron spin-up and spin-down states in the conduction band with the z-component of the angular momentum $J_z = \pm\frac{1}{2}$, and heavy hole states with $J_z = \pm\frac{3}{2}$, see Fig. 2.3. In such a system there are only two possible transitions in which the angular momentum is conserved, i.e. those for which $\Delta J_z = \pm 1$. Transitions involving spin-up states, from $J_z = 1/2$ to $J_z = 3/2$ result in the emission of left-circularly polarized light σ_-, whereas those with negative spin values, from $J_z = -1/2$ to $J_z = -3/2$ yield right circular polarization σ_+. These two circularly polarized fields $E_\pm$ are coupled by linear anisotropies, i.e. linear birefringence and linear dichroism, and by nonlinear light-matter interactions governed by the linewidth enhancement factor [117]. Due to this coupling, QW VCSELs emit linearly polarized light, where the two orthogonal linear components of the electric field read:

$$E_x = \frac{E_+ + E_-}{\sqrt{2}} \tag{2.1}$$

$$E_y = -i\frac{E_+ - E_-}{\sqrt{2}} \tag{2.2}$$

The reservoirs of spin-up and spin-down carriers are coupled through the spin-flip processes, which always tend to equalize their populations and, therefore, spin dynamics, characterized by the spin-flip rate γ_S, also influences the polarization properties.

The SFM model provides a coherent picture of how polarization properties of VCSELs are affected by different types of anisotropies. An alternative approach accounts for temperature- and frequency-dependence of the material gain [107, 109, 119], mechanisms that are neglected in the SFM model. Indeed, in real devices changes of the operation conditions, i.e. pump current and/or substrate temperature, result in a redshift of both the peak gain frequency and the cavity resonance. If we take into account that birefringence splits the frequency of the two LP modes, then they must also experience different

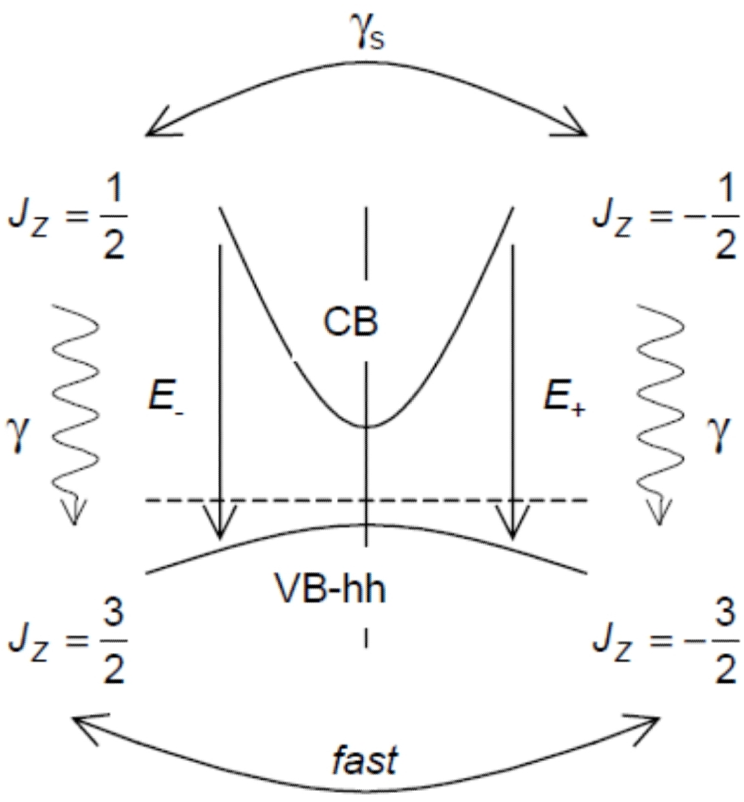

Figure 2.3: Four level system of SFM model. CB - conduction band and VB - hh - heavy hole band are split into different spin sublevels. The reservoirs of spin-up and spin-down carriers are coupled through the spin-flip processes which always tend to equalize their populations with the characteristic spin-flip rate γ_s. Taken from [118].

gains. Consequently, at the lasing threshold the laser emission is associated with the LP mode which experiences higher gain. To achieve the best overlap between the gain curve and the cavity resonance over a wide range of currents the cavity is designed to be at the low-frequency side of the gain maximum and consequently in the vast majority of cases it is the higher frequency LP mode that lases close to threshold, see Fig. 2.4. The increase of the pump current heats the structure and results in a considerable redshift of both the gain curve and the frequencies of the LP modes. The gain curve however, shifts faster and at some point, after the high-frequency LP mode crosses the

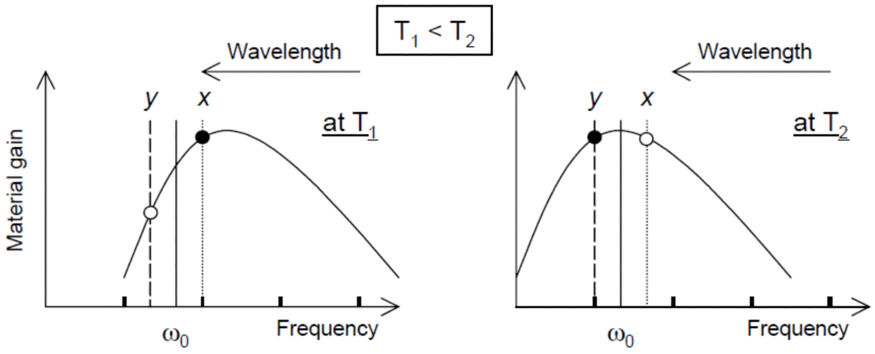

Figure 2.4: Schematic representation of type-I polarization switching due to current heating induced redshift of the cavity resonance ω_0 with respect to the peak gain frequency. x and y correspond to the linearly polarized, orthogonal modes. Taken from [118].

peak gain frequency, the laser emission switches abruptly to the low-frequency LP mode because now it has the highest gain. It explains type-I polarization switching. In order to explain polarization switching of type-II, the model has to account also for the material losses, which are dominated by the heavy-hole split-off band absorption [109]. In such an approach, under given conditions the laser emission is associated with the LP mode which experiences higher net gain.

2.1.3 Elliptical polarization in QW VCSELs

In majority of cases QW VCSELs emit linearly polarized light [116, 117, 120]. However, there are circumstances under which the emission becomes elliptically polarized [116, 117, 121, 122, 123]. Such an emission occurs, for instance, for type-II polarization switching in VCSELs with rather small value of birefringence, i.e. smaller than the spin-flip rate, and isotropic gain [116]. In this case, just above threshold there is a bistability between the two LP modes and, therefore, the laser behavior will depend on which of them is selected at the threshold. If it is the high-frequency LP mode then regardless of the current, this polarization remains stable. Much more interesting is the alternative selection, namely when the current increases, first the lasing low-frequency LP mode loses stability and becomes elliptically polarized. Consecutively, also the elliptically polarized mode becomes unstable and eventually the laser switches to the high-frequency LP mode. It is worth noticing, that the range of stable elliptically polarized light emission (region EP in the inset of Fig. 2.5) is very narrow. The corresponding states are frequency degenerate with two possible signs for the azimuth. The transition from one linearly polarized mode to the other one can occur through either of these two states [116]. Characteristic

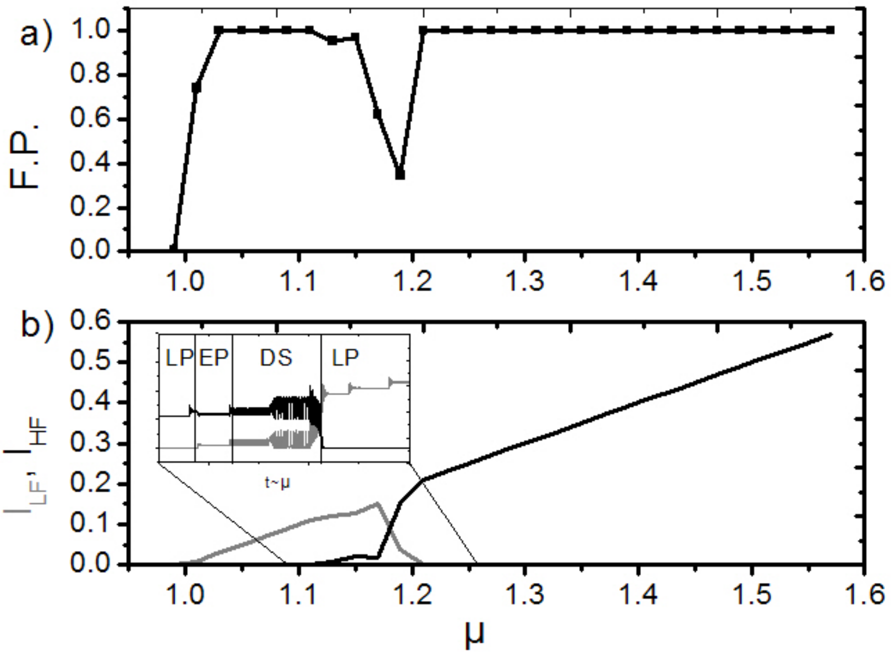

Figure 2.5: a) Fractional polarization coefficient $F.P.$ as a function of the normalized pump current μ and b) the corresponding time-averaged polarization resolved power-current characteristics showing polarization switching of type-II from low-frequency LP mode I_{LH} (gray curve) to high-frequency I_{HF} one (black curve) involving transition to elliptically polarized light emission (EP) and emergence of dynamical states (DS). The inset shows polarization resolved power-current characteristics without time-averaging. The characteristics have been calculated by numerical integration of the SFM model equations [116] with the decay rate of the total carrier number $\gamma = 1$ ns^{-1}, birefringence $\gamma_{bf} = 2\gamma$, dichroism $\gamma_a = 0$, the linewidth enhancement factor $\alpha = 3$, the spin-flip rate $\gamma_S = 50$ ns^{-1} and the decay rate of the electric field in the cavity $\kappa = 300$ ns^{-1}.

feature of the described scenario is that the switching involves the so-called dynamical states which can be understood as an elliptically polarized state whose ellipticity and azimuth change in time in a periodic or chaotic way [116]. In Fig. 2.5 this is seen as a periodic intensity modulation of both LP modes (region DS in the inset). The value of fractional polarization coefficient F.P. corresponding to this state is smaller than one.

When birefringence is comparable with the spin-flip rate, meaning that sublevel population dynamics becomes relevant, the scenario is slightly different. Unlike in the previous case, it is only the low-frequency mode that is stable just above the threshold. As shown in Fig. 2.6, when the current is increased, this mode loses stability and becomes elliptically polarized. Then it gives way to a state of mixed polarization (MX) involving periodic modulation of the intensities of the LP modes and of the total intensity [116]. The value of fractional polarization coefficient F.P. becomes smaller than one in this regime. For larger current the laser loses its coherence and the optical spectra become very broad, probably chaotic. In both scenarios, in the range

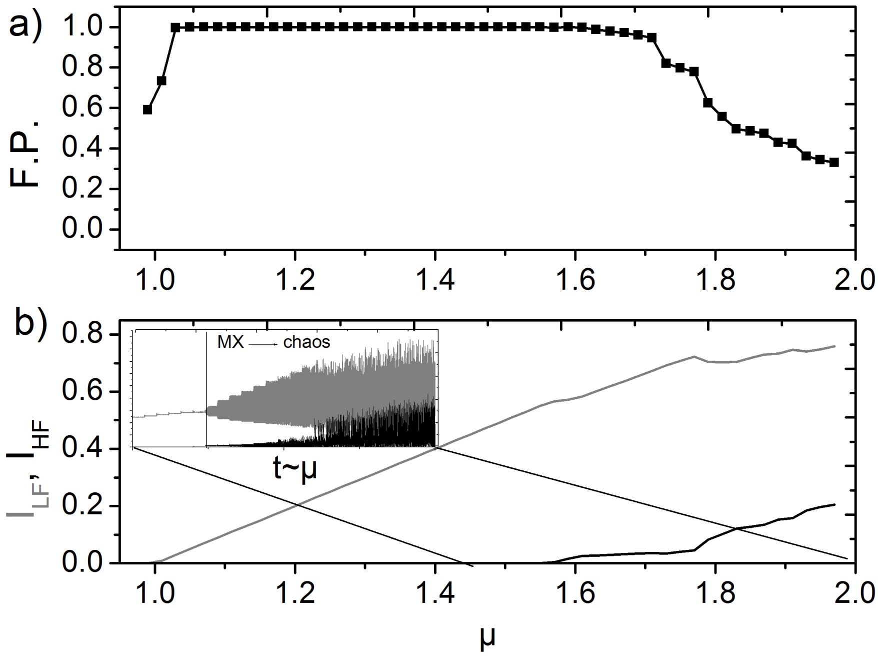

Figure 2.6: a) Fractional polarization coefficient *F.P.* as a function of the normalized pump current μ and b) the corresponding time-averaged polarization resolved power-current characteristics showing polarization instabilities involving state of mixed polarization (MX) and transition to chaotic emission. The inset shows polarization resolved power-current characteristics without time-averaging. The characteristics have been calculated by numerical integration of the SFM model equations [116] with the decay rate of the total carrier number $\gamma = 1$ ns^{-1}, birefringence $\gamma_{bf} = 10\gamma$, dichroism $\gamma_a = 0$, the linewidth enhancement factor $\alpha = 3$, the spin-flip rate $\gamma_S = 50$ ns^{-1} and the decay rate of the electric field in the cavity $\kappa = 300$ ns^{-1}.

of stable linear and elliptical polarization optical spectra, i.e. spectra of the optical field amplitude, possess single well-resolved peak. Due to the intensity modulation of the LP modes in the region involving dynamical states and state of mixed polarization there additionally appear small-amplitude sidebands. Moreover, in both cases transition from elliptically polarized emission to the emission involving dynamical states/state of mixed polarization appears through a Hopf bifurcation (see Sec. 4.1 for definition) [123, 124]. Polarization switching involving dynamical states has been studied experimentally in [125, 126]. Although the emitted light had residual ellipticity already at the lasing threshold, the authors showed that it did not influence the existence of the dynamical states. Indeed, before switching to the high-frequency LP mode the ellipticity angle starts increasing and then the dynamical states appear as manifested by the emergence of sidebands in the optical spectrum. The frequency of the sidebands has been attributed to the effective birefringence, i.e. the sum of the linear birefringence observed at the lasing threshold and nonlinear contributions due to saturable dispersion and spin dynamics. In the scenario involving state of mixed polarization the frequency of the sidebands is close to the beating frequency between the two LP modes [116].

Presented scenarios are based on the assumption that the dichroism is small, so that the gain is almost isotropic. Therefore, the information about the angle between the dichroism and birefringence does not change the overall description. In turns out however, that when both anisotropies are present in the laser and additionally their axes ale misaligned then the stationary solutions are elliptically polarized and their ellipticity increases with the misalignment [127]. Misalignment introduces mixing between otherwise linearly polarized modes and affects their stability, i.e. it decreases the stability domain of the higher gain mode and increases the stability domain of the orthogonal one [127]. Although it is not a focus of this dissertation, we would like to mention that elliptically polarized emission has also been observed for QW VCSELs placed in the magnetic field [121, 122]. In this case, the switching does not occur between orthogonal linearly polarized states but between orthogonal elliptically polarized states with small ellipticity.

2.1.4 Properties of QDs that may influence polarization properties of QD VCSELs

According to the SFM model polarization properties of QW VCSELs are determined by the interplay between the anisotropies, spin-flip processes and the linewidth enhancement factor. In regard to all of these mechanisms QDs and QWs are noticeably different and, therefore, these differences should somehow influence polarization characteristics of QD VCSELs. First of all, carriers in QDs are confined within a very small volume. Single particle energy spectrum that accounts solely for quantization energies will, therefore, be affected by the Coulomb electron-hole interaction (charge dependent) and exchange interaction (spin dependent). Ultimately, due to a close proximity of electron and holes, Coulomb interaction will result in bound complexes, such like excitons X, charged excitons (trions) X^+/X^-, neutral XX and charged biexcitons XX^+/XX^- etc. [128, 129], each with slightly different energy, see Fig. 2.7.

If we limit the problem to excitons only, the total angular momentum J_z of a heavy-hole exciton (which comprises an electron with the spin $s = \pm\frac{1}{2}$ and a heavy-hole with the angular momentum $j = \pm\frac{3}{2}$) can achieve one out of four values corresponding to degenerate states. States with $J_z = \pm 2$ are optically forbidden, and therefore they are commonly referred to as dark ones. Likewise, states with $J_z = \pm 1$ are accessible through a single photon absorption or emission and are, therefore, denoted as bright ones.

The electron-hole exchange interaction first, induces splitting between bright and dark states and then mixes the dark states and lifts their degeneracy forming a dark doublet $(|2> \pm |-2>)$[129]. Moreover, lowering of the confinement symmetry, resulting from structural elongation of QDs and strain-induced piezoelectric fields, mixes the bright states and produces a nondegenerate bright doublet of $X^x = (|1> + |-1>)/\sqrt{2}$ and $X^y = (|1> - |-1>)/i\sqrt{2}$. Although recombination of bright excitons results in left and right circularly polarized light, the mixed states in structures grown on (001) substrate are usually linearly polarized along the [110] and [1-10] crystallographic directions [129], see Fig. 2.8. The energy difference between these two states, commonly referred to as exciton fine-structure splitting (FSS), depends on structural properties of QDs and ranges from a few to few

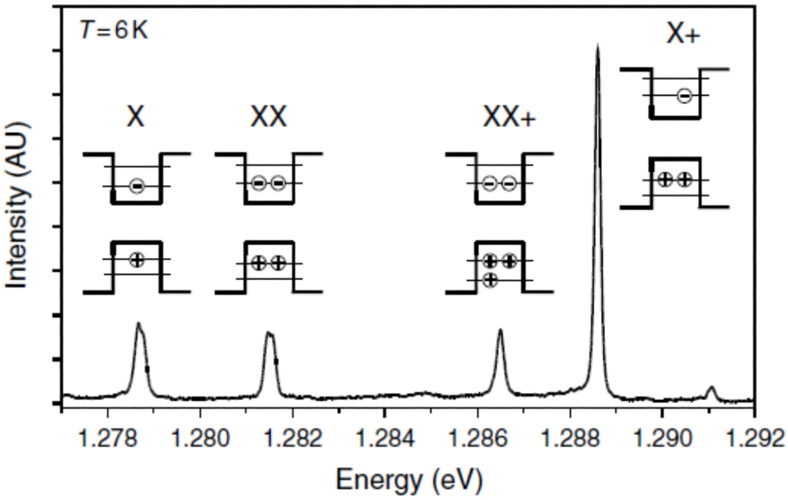

Figure 2.7: Cathodoluminescence spectra of a single-InAs quantum dot in a GaAs matrix. The emission lines correspond to different excitonic complexes, i.e. X excitons, XX biexcitons, XX^+ positively charged biexcitons, X^+, positively charged excitons (trion). Taken from [130].

hundreds of μeV in (InGa)As QDs [129, 131, 132].

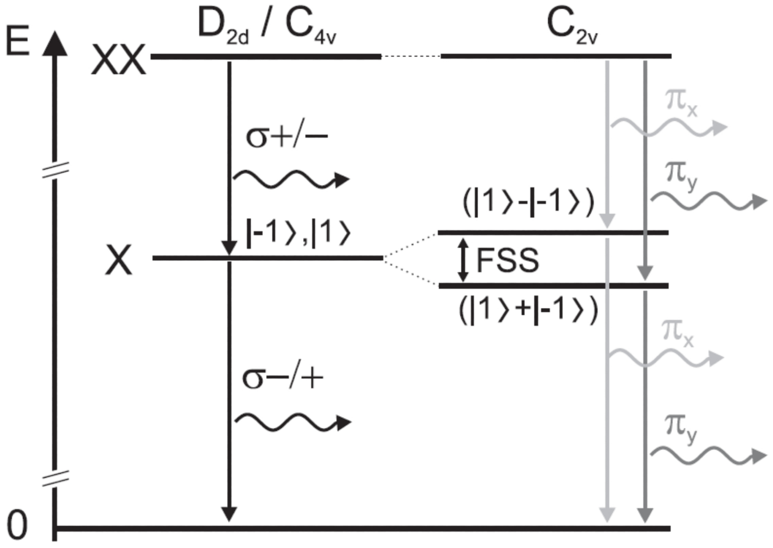

Figure 2.8: Effect of the exchange interaction on the exciton (X) bright states. XX denotes the biexciton ground state. $|J_z\rangle$ is the exciton total angular momentum, $\sigma\pm$ denotes circularly polarized light, and $\pi_{x/y}$ linearly polarized light with x = [110] and y = [1-10]. D_{2d}, C_{4v}, and C_{2v} indicate the confinement potential symmetry. Taken from [129].

In [88] shape anisotropy of self-assembled InGaAs QDs grown on GaAs(100) substrate have been proposed to stabilize polarization of QD VCSELs. The mean length in the [0-11] and [011] directions has been estimated to be 33 nm and 17 nm, respectively, resulting in lateral aspect ratio of 1.94, see Fig. 2.9a. The polarization-resolved photoluminescence spectra of such a QD ensemble show that for the QD emission component at 1000 nm the intensity along [0-11] is 1.37 times stronger than that along [011]. The shoulder peak at 920 nm, attributed to the wetting layer, does not show polarization dependence, see Fig. 2.9b. The authors reported that all the investigated devices showed stable, linearly polarized emission along the elongated [0-11] direction. However, these devices operated only at pulsed regime, i.e. without overheating. Since polarization properties of QW VCSELs can be greatly affected by temperature it cannot, therefore, be taken as granted that their polarization would remain stable during the operation in continuous wave regime at room temperature. Moreover, such large lateral aspect ratio is not a common feature of all QDs. For instance, SML QDs have symmetrical shape and lateral aspect ratio close to unity [10]. This shows that polarization properties of QD

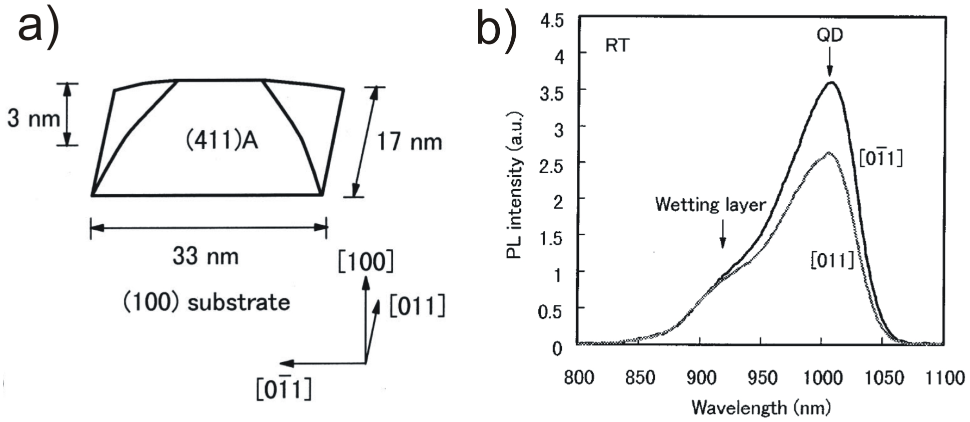

Figure 2.9: a) Estimated shape of $In_{0.5}Ga_{0.5}As$ QDs and b) their photoluminescence spectra at room temperature. Taken from [88]

VCSELs definitely deserve more detail investigation.

Shape anisotropy effects on the electronic properties of an ensemble of SML InGaAs/GaAs QDs are investigated in [133]. In the backscattering geometry, i.e. when the light propagates in the (001) direction, PL emission is predominantly polarized along the QD elongation direction, i.e. [1-10], with the polarization anisotropy coefficient $P = (I_{[1-10]} - I_{[110]}/(I_{[1-10]} + I_{[110]})$ of $P = 0.2$. Interestingly, this value is similar to the one calculated from Fig. 2.9b for elongated SK QDs.

Another feature of QDs that may influence polarization properties of QD VCSELs is slowing down of the carrier spin relaxation processes as compared to bulk or QW structures. In the framework of the SFM model these processes are expressed by the spin-flip rate [115]. In QWs, a linear polarization decay time for excitons is of a few tens of picoseconds [134, 135, 136]. In contrast, in QDs the exciton spin is maintained during the whole exciton lifetime and spin relaxation times τ_S as long as few nanoseconds have been reported [137, 138, 139, 140]. Such a difference between QWs and QDs has been attributed to the suppression of the D'yakonov-Perel mechanism [1][142], which is the most significant spin relaxation mechanism in QWs [136, 141]. Instead, electron spin relaxation takes place by hyperfine interactions with nuclei [141, 143, 144], and by acoustic phonon [139] and/or LO phonon processes [141]. It should be noted however, that such large values of the spin relaxation time have been measured at cryogenic temperatures. At higher temperatures τ_S decreases rapidly but still is of the order of few tens of picoseconds [139, 141].

Slowing down of the spin relaxation will influence the intradot carrier

---

[1] D'yakonov-Perel mechanism is associated with the spin splitting of the electron dispersion curve in crystals lacking a center of symmetry, e.g. GaAs, [141], which is equivalent to the presence of the effective magnetic field that causes the electron spin to precess.

dynamics. Indeed, there is only a finite number of carriers that can be located in a single QD. For instance, at the ground state energy level there is only one state for spin-down and another one for spin-up electrons. It, therefore, happens that two electrons with identical spin have to compete for the same quantum state [145, 146]. Only one of them can succeed and, consequently, the other one either flips its spin and relaxes to the spin-down ground state or remains on the excited state. Since the spin relaxation in QDs is slowed down, both process will lead to the so-called spin blocking, which can effectively enhance the excited state emission [146].

Finally, the polarization properties of QW VCSELs, specifically polarization stability, depend on the linewidth enhancement factor, i.e. when its value is zero the polarization switching does not occur [116]. Therefore, in the SFM description VCSELs with ideal QD ensemble should exhibit no polarization instabilities. However, size inhomogeneity and contributions of the excited states break the symmetry of the gain spectrum so that the values of the linewidth enhancement factor reported for QD lasers are comparable to those of their QW counterparts. It shows again that polarization properties of QD VCSELs deserve detail experimental study.

2.2 Experimental details

2.2.1 QD VCSELs used in the experiments

In our experimental study we have used three wafers of QD VCSELs. Two of them are based on dense arrays of SML QDs and the remaining one on QDs grown in Stranski-Krastanov mode. All the wafers were provided by Technical University of Berlin, Germany. Structures with SML QDs, characterized in detail in [75], were grown by molecular-beam epitaxy on GaAs(100) substrates. The bottom and top distributed Bragg reflectors (DBR) consist of 32 and 19 pairs, respectively. $3\lambda/2$-long cavity contains three stacks of SML QDs separated by 13 nm thick GaAs spacers. Submonolayer deposition was performed in 0.5ML InAs - 2.3ML GaAs cycles repeated ten times. The characteristic feature size and areal density of QDs estimated from transmission electron microscopy images are 30-50 nm and $(2\text{-}3)\times10^{10}$ cm^{-2}, respectively. The photoluminescence peak is centered at around 980 nm. Current aperture was implemented as an AlO_x layer placed at the p-side in the position of the field intensity node closest to the active region.

VCSELs with SK QDs, characterized in detail in [19, 87], were grown using metalorganic chemical vapor deposition (MOCVD) on Si doped GaAs (001) substrates. The active region of these intra-cavity contacted structures consists of three stacks of QDs separated by 35 nm thick spacers. Each stack comprises three layers of $\mathrm{In}_{0.5}\mathrm{Ga}_{0.5}\mathrm{As}$ QDs grown on GaAs wetting layer and overgrown with a 5 nm thick $\mathrm{In}_{0.5}\mathrm{Ga}_{0.5}\mathrm{As}$ QW. They are positioned at the antinodes of the field intensity of a 4λ cavity. The areal density of QDs estimated from transmission electron microscopy images is 7×10^{10} cm^{-2}. Similarly to SML QD VCSELs, current aperture was implemented as an AlO$_x$ layer. Both, bottom and top DBR mirrors are oxidized and consist of 7 and 6 pairs of AlO$_x$/GaAs, respectively.

2.2.2 Experimental set-up

Before testing, the wafers were mounted on a cooper holder which, in turn, was attached to a thermo-electric element. To ensure efficient heat removal the other side of the thermo-electric element was attached to a bulky cooper block. The temperature of the copper holder, and thus the temperature of the wafer, is controlled by an electronic feedback loop using thermistor placed in a drilled hole of the holder. The stability of the temperature control is of the order of few mK. Due to a lack of wire bonding, to provide the injection current to the contacts we need to use probes. Note however, that this solution has some disadvantages, e.g. the probes can be a source of external stress which can contribute to the inherent anisotropies of the devices hence influence their polarization properties [110, 111, 113]. As a DC-current source we use a power supplier included in the Pro8000 mainframe (module MLC 8050AG) (CTR, see Fig. 2.10). In the experiments with current-modulation the laser is driven by a combination of the DC bias with the RF current, the latter being created by a function generator. To collimate the light emitted by the VCSELs we use an anti-reflection coated aspherical lens (CL) with a focal length of 3.1 mm. To make sure that the polarization instabilities described in the following sections are not induced by the feedback from this lens, we have repeated the measurements with two additional lenses with focal lengths of 11 mm and 35 mm, respectively. The collimated light is reflected by a mirror (MR) and passes through an optical isolator (ISO). The latter works as a rotable polarizer and helps to avoid feedback from the facet of the optical fiber (OF).

We will limit our study only to QD VCSELs operating in a single transverse mode regime. To select such devices we need to be able to characterize their optical spectra and to this aim we use the optical spectrum analyzer Ando AQ6317B with maximum resolution of 0.01 nm. To characterize the region of polarization instability in more details we employ a piezoelectrically scanned plane mirror Fabry-Perot interferometer (FPI) (Burleigh) with a free spectral range of 30 GHz. Its finesse is typically larger than 160 however, the investigated QD VCSELs operate at the wavelengths that fall outside the FPI operation range and as a result the maximum finesse obtained in our experiment did not exceed 20. To measure polarization resolved power-current characteristics we use power meter Newport 2832-C. Since its bandwidth is only 47 kHz, to measure polarization resolved time series we use a digital oscilloscope Tektronix CSA7404 with the optical channel bandwidth of 2.4 GHz. Radio frequency (RF) spectra are measured with a power spec-

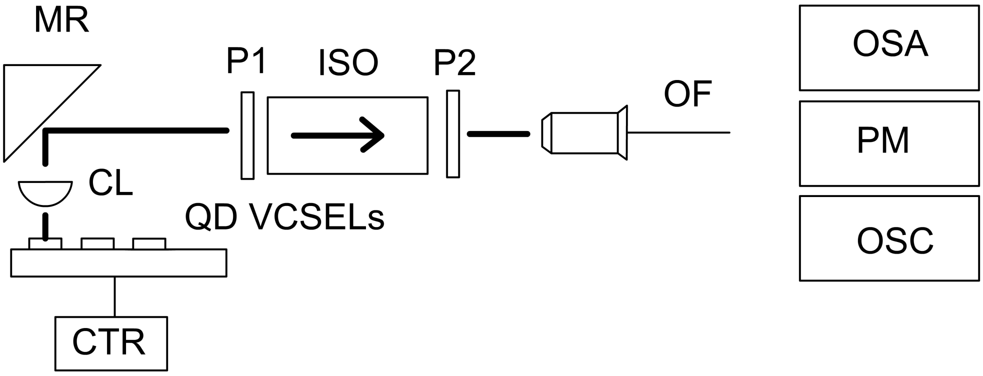

Figure 2.10: Experimental set-up. CTR: current driver and temperature controller, CL: collimator, MR: mirror, P1,P2: polarizers, ISO: optical isolator, OF: optical fiber, OSA: optical spectrum analyzer, PM: power meter, OSC: oscilloscope.

trum analyzer Anritsu MS2667C (bandwidth 7 kHz-30 GHz) and a 12 GHz bandwidth photodetector New Focus 1554-B. Signal from the photodetector needs to be amplified and to this aim we use two microwave amplifiers, each providing amplification of 20 dB.

2.3 Polarization properties of investigated QD VCSELs

We have investigated polarization properties of 50 single-transverse mode QD VCSELs: 24 with SK QDs and 26 with SML QDs. Five SK QD VCSELs abruptly switched their polarization to the orthogonal, linearly polarized mode when the wafer temperature was increased. Unlike in QW VCSELs however, switching has not been maintained in the consecutive measurements. Such behavior is described in Sec. 2.5. In the case of SML QD VCSELs, seven devices show very stable and reproducible polarization switching accompanied by polarization mode hopping between nonorthogonal, elliptically polarized states. Its characteristics are described in detail in Sec. 2.4. In the investigated range of currents and temperatures the remaining lasers exhibit stable, linearly polarized emission. Fig. 2.11 shows the polarization orientation of such SML and SK QD VCSELs. As it can be concluded from this figure, in the case of SK QD VCSELs polarization orientation changes from device to device. The distribution however, achieves two maxima at the x (90) and y (0) directions corresponding to the main crystallographic axes. In this regard SK QD VCSELs resemble QW devices. On contrary, polarization orientation of the investigated SML QD VCSELs is aligned with the y direction. Close to the lasing threshold this is also the case for the devices showing polarization

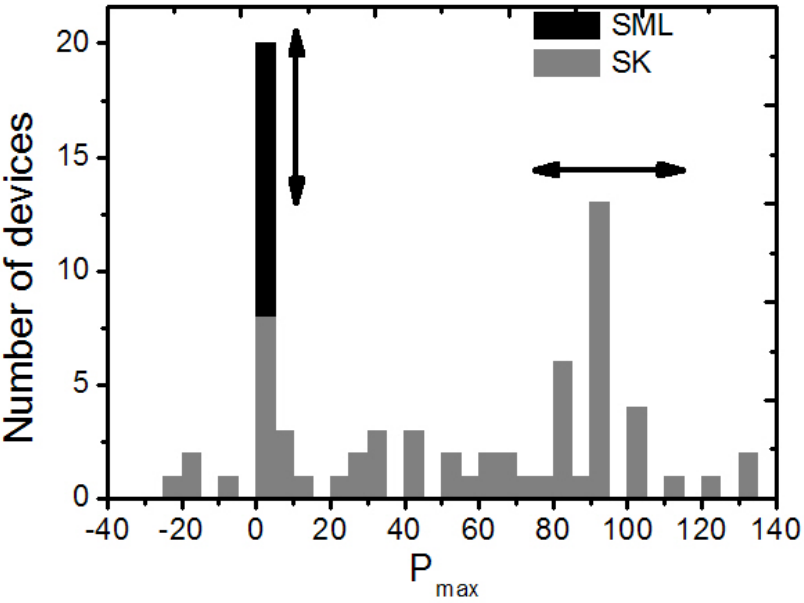

Figure 2.11: Distribution of polarization orientation P_{max} for SML (black) and SK (gray) QD VCSELs showing stable, linearly polarized emission.

instabilities.

2.4 Polarization switching in SML QD VCSELs

The output power as a function of the pump current of one of the SML QD VCSELs showing polarization instabilities is plotted in Fig. 2.12a. At a wafer temperature of 298K the threshold current is of 0.59 mA. Within the investigated range of currents the laser supports single transverse mode operation and emits at around 990 nm, see Fig. 2.12b. Polarization resolved power-current characteristics are shown in Fig. 2.13.

Close to the lasing threshold the laser emits linearly polarized light along the y-axis (dotted curve), which corresponds to the [0-11] or [011] crystallographic direction. At a current of 1.75 mA, referred to as point A in Fig. 2.13, the power measured at the orthogonal direction starts to grow. Since in the whole range of currents shown in Fig. 2.13 the laser operates in a single mode, the point A indicates a bifurcation to a stable, elliptically polarized emission (EP). As it is shown in Fig. 2.14a the orientation of the EP state does not coincide with the y-linearly polarized one. Instead, the polarization ellipse rotates so

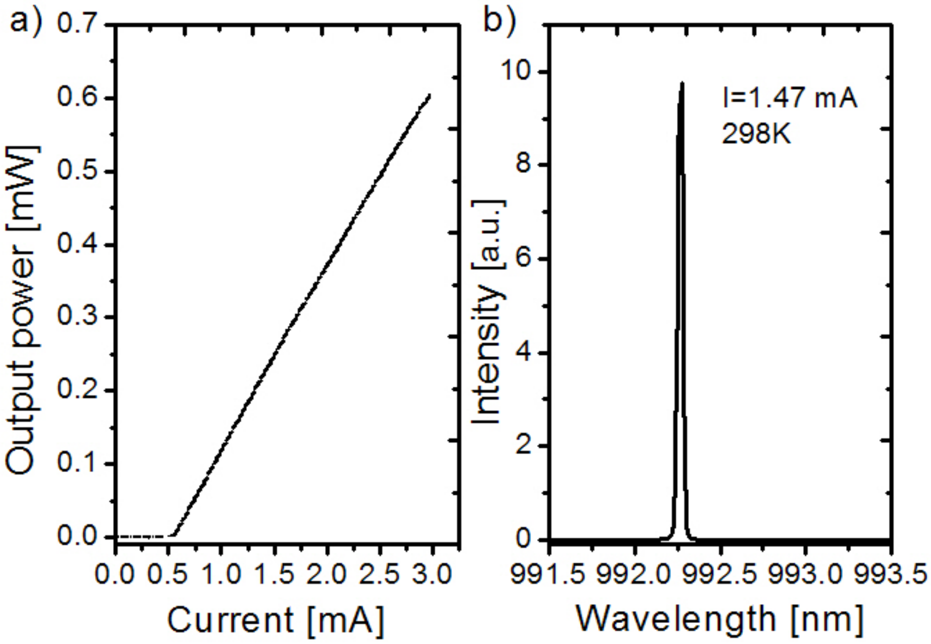

Figure 2.12: a) Output power as a function of the pump current for a SML QD VCSEL showing polarization instabilities. b) Optical spectrum at $I = 1.47$ mA.

that the difference between its major axis and the y direction (expressed as α in Fig. 2.14a) increases when the current is increased. The consecutive increments of the polarization angle are smaller and tend to saturate close to the I_S point, where the difference is maximum and amounts to 20 deg. Likewise, the ellipticity of the EP state, calculated as the ratio of the power corresponding to the minor and major axes of the polarization ellipse, increases after the point A and achieves its maximum of 8% close to I_S, see Fig. 2.14b. We would like to note that Fig. 2.14 corresponds to a SML QD VCSEL different from the one characterized in detail in this section. However, all SML QD VCSELs showing polarization instabilities exhibit the same transition to elliptically polarized emission and, therefore, Fig. 2.14 can be considered as representative for the whole group.

Observing the current dependence of the output power for the polarizer oriented along the x- and y- directions in Fig. 2.13, we see that there is a small abrupt increase for the y direction at the point I_S, complemented by a similar drop of the power in the x direction. This might result from exchange of the energy between the two polarization modes as it is the case in polarization switching in QW VCSELs. Indeed, when we deviate the transmission axis of the polarizer from the x and y directions, at a current larger than I_S we do

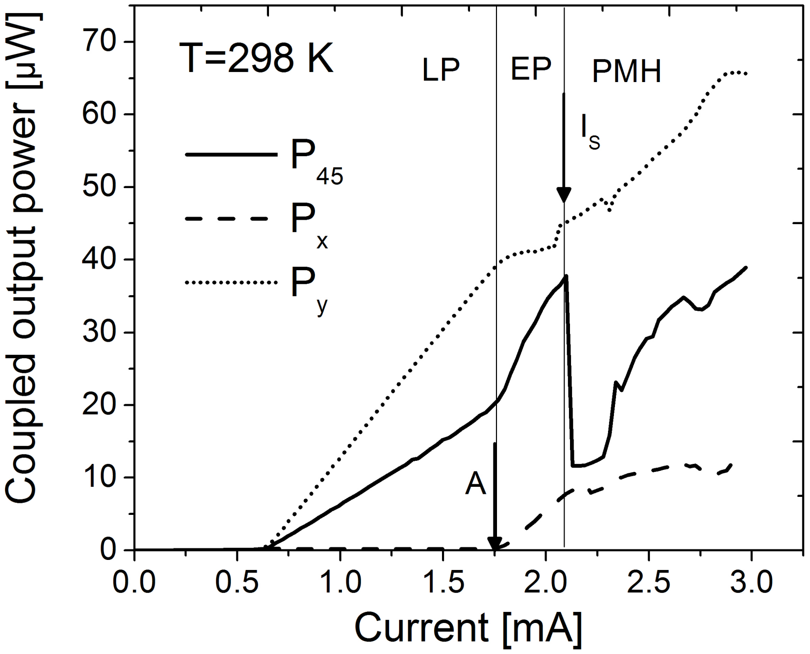

Figure 2.13: Polarization resolved power-current characteristics of SML QD VCSEL showing polarization instabilities. Polarization angle is denoted as a subscript, e.g. P_{45} means 45 deg with respect to the y axis.

observe such a large power drop. Point I_S starts a wide region of polarization mode hopping. The amplitude of hopping changes when turning the polarizer and achieves a maximum value at direction of 45 deg. In Fig. 2.13 the power versus current characteristics captured at such an orientation of the polarizer is represented by the solid curve.

To determine the polarization states between which the switching occurs we fix the current inside the switching region just after I_S (at 2.115 mA) and measure the power at various orientations of the polarizer. The results are plotted in Fig. 2.15. The dashed and dotted curves represent the maximum I_{max} and minimum I_{min} power at the switching, respectively (see also Fig. 2.16 for I_{max} and I_{min} definition). The solid curve shows the difference $I_{max} - I_{min}$, i.e. the amplitude of the switching. It achieves two maxima and two minima as a function of the polarizer orientation. The two minima correspond to the x and y directions, whereas the two maxima correspond to directions of 45 deg with respect to the $x(y)$ axes. The fact that the dotted curve never reaches zero suggests that the switching takes place between elliptically polarized states. This has been validated using a combination of a

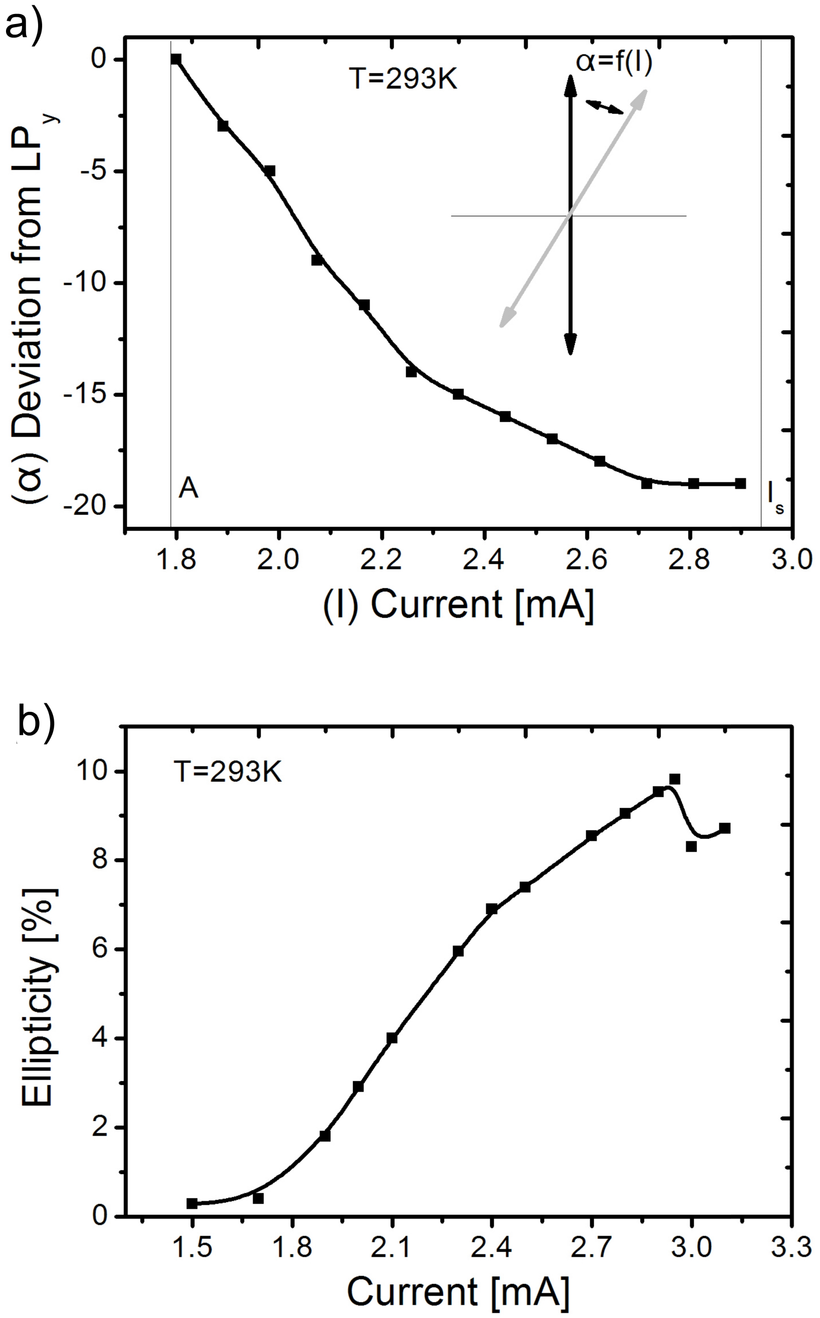

Figure 2.14: a) Current dependence of the angle α between the orientation of the y-LP mode and the major axis of the polarization ellipse of the EP mode. b) Current dependence of the ellipticity of the EP mode.

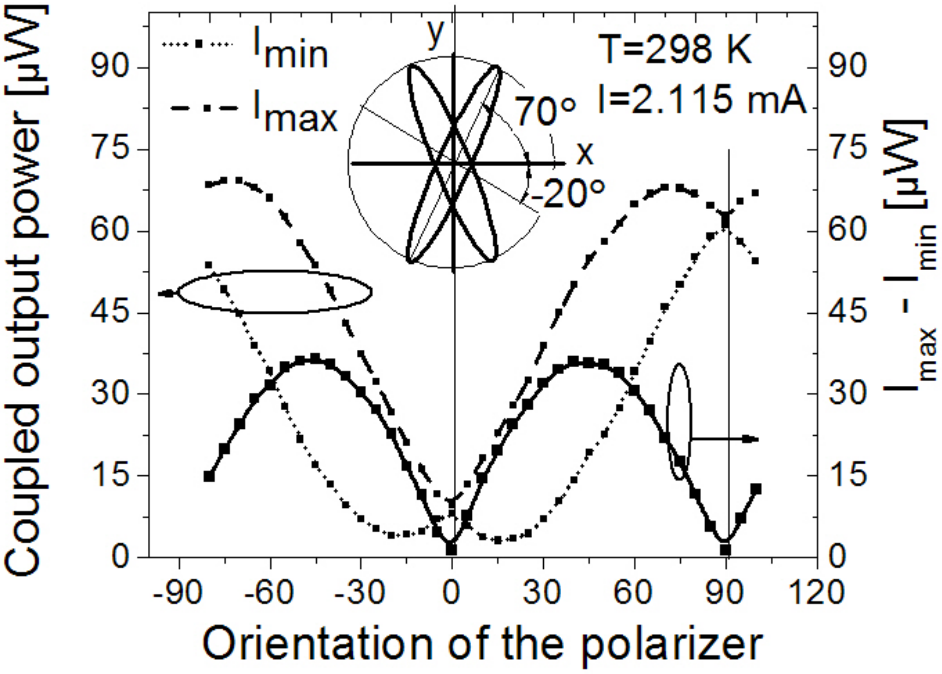

Figure 2.15: Maximum I_{max} (dashed curve) and minimum I_{min} (dotted curve) of the output power at the switching as a function of the polarizer direction, measured at a current of 2.115 mA and temperature of 298K. The solid curve shows the difference $I_{max} - I_{min}$, i.e. the amplitude of switching. The inset shows the orientation of the determined polarization ellipses between which polarization mode hopping takes place.

linear polarization and a quarter-wave plate. The ellipticity of the elliptically polarized states, estimated from Fig. 2.15, is of 6%. The positions of the two minima (± 20 deg) of the dotted curve correspond to the minor axes of the two polarization ellipses. Similarly, the positions of the two maxima of the dashed curve (± 70 deg) correspond to the major axes of these ellipses, see the inset in Fig. 2.15. The polarization switching, therefore, takes place between distinct polarization ellipses which main axes do not coincide with the orientation of the LP states. Furthermore, since the angle between their major axes is 40 deg, they are nonorthogonal, which is in contrast to polarization switching between orthogonal LP modes in QW VCSELs. Still another difference is that after the point I_S the emission is dominated neither by the LP mode that is suppressed close to the lasing threshold nor by the elliptically polarized mode that appears at the switching point. Instead, there is a random hopping between nonorthogonal, elliptically polarized modes which extends

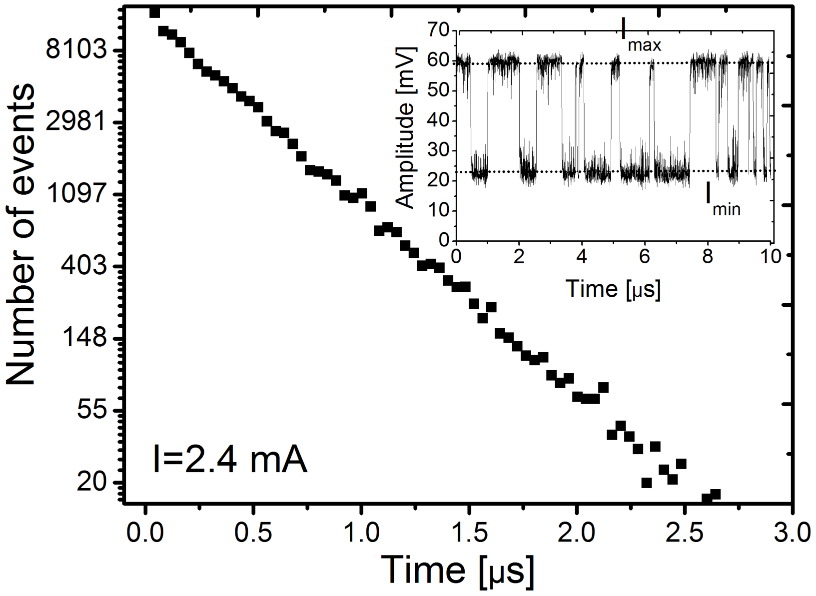

Figure 2.16: Semi-logarithmic plot for dwell time statistics at the current of 2.4 mA. The inset shows an example of time trace of the output power projected on the transmission axis of the polarizer of 45 deg.

over a very wide range of currents. The inset of Fig. 2.16 shows an example of a time-trace at a current of 2.4 mA. Since in the region of polarization mode hopping the total output power remains constant, we can expect that similarly to LP modes in QW VCSELs the two elliptically polarized modes exhibit antiphase dynamics, i.e. when one mode is switched on, the remaining one is switched off. Consequently, to characterize the observed polarization mode hopping it is enough to analyze the dynamics of only one of the modes. The time-trace shown in the inset of Fig. 2.16 has been captured at the orientation of the polarizer corresponding to the maximum amplitude of switching and, therefore, both states I_{max} and I_{min} correspond to linear projections of the two elliptically polarized states on this direction. To characterize polarization mode hopping we measure the distribution of the dwell time, i.e. the time that the system stays in one state before switching. The distribution is computed from an analysis of over 10^4 switchings. As it is shown in Fig. 2.16 the distribution is exponential, which agrees with what has been published for polarization mode hopping in QW VCSELs [147] and shows that the hopping is stimulated by noise. The average dwell time estimated from the distribution is of 20 ns. The dynamics is symmetric, i.e. the statistics of the dwell time is the same for both elliptically polarized states. Moreover, such symmetric

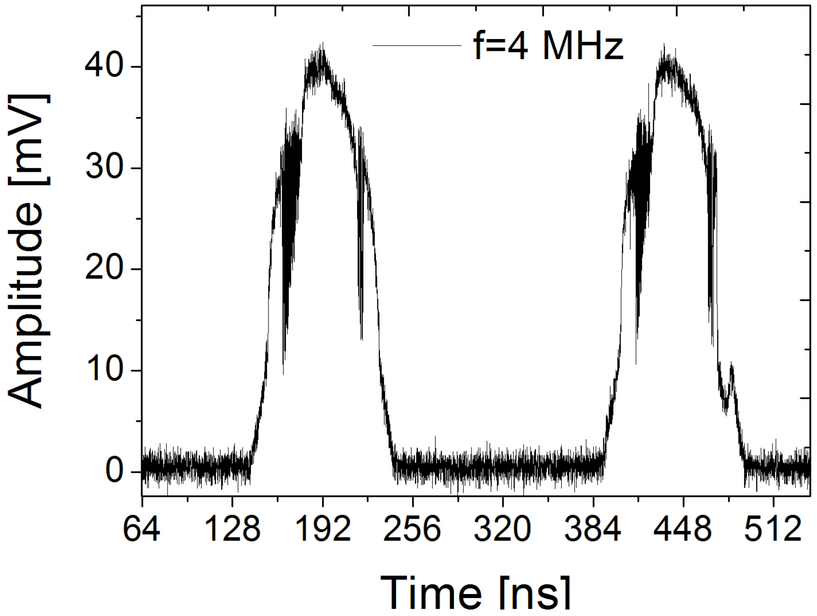

Figure 2.17: Polarization resolved output power at large-signal current modulation with a frequency of 4 MHz.

switching is maintained in the whole region of polarization mode hopping.

To check which physical mechanism may be responsible for the observed polarization switching we perform a large-signal current modulation, see Fig. 2.17. We match the amplitude of the modulation so that we cross the region of polarization mode hopping. The cut-off frequency, i.e. the frequency at which no switching is observed is determined in these measurements to be about 100 MHz. Since the intradot processes occur at a much faster timescale of a few tens of picoseconds we suspect that the switching is of thermal origin.

Detail study on the dynamics of polarization mode hopping in SML QD VCSELs is presented in Chap. 3.

2.5 Polarization switching in SK QD VCSELs

In the case of SK QD VCSELs, five out of 24 devices showed polarization instabilities. Their characteristics however, are different from what has been observed in SML QD VCSELs and resemble polarization switching between orthogonal LP modes in QW VCSELs. As it is shown in Fig. 2.18a, at the wafer temperature of 298K the laser emits linearly polarized light along P_{65} (subscript denotes polarization angle, e.g. P_{45} means 45 deg with respect to the y axis). We have checked that in the investigated range of currents it

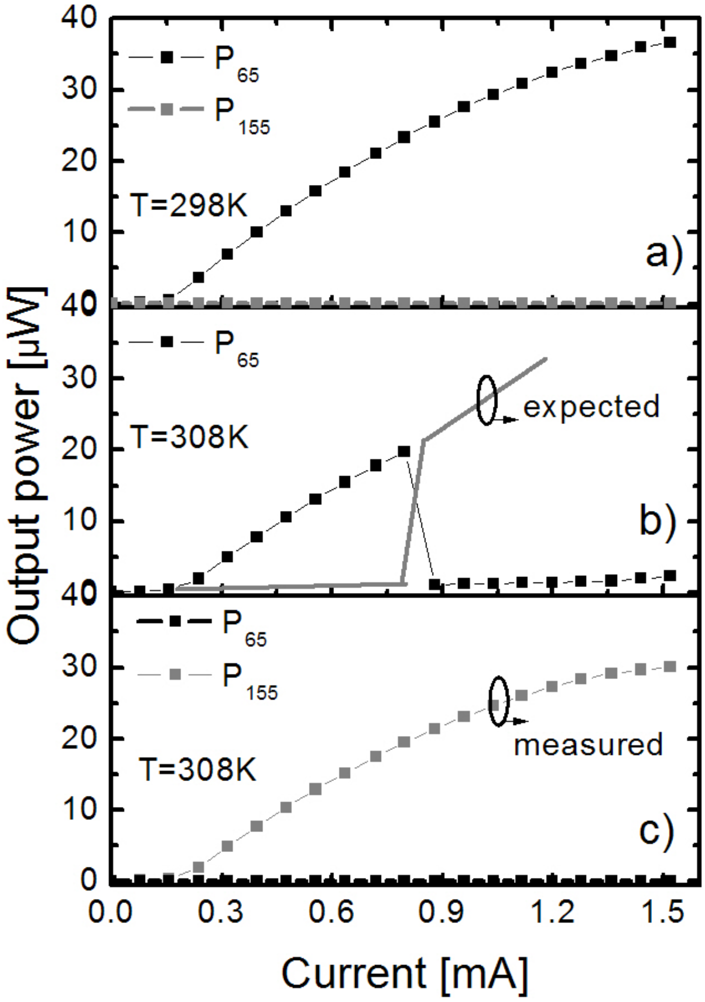

Figure 2.18: Polarization resolved power-current characteristics measured at a temperature of a) 298 K, b),c) 308K.

operates in a single transverse mode. Polarization instabilities are observed at higher temperatures. Specifically, as shown in Fig. 2.18b, at the wafer temperature of 308K when the pump current is increased the power of the lasing polarization component drops abruptly to zero. One can, therefore, expect that at the switching point the emission has switched to the orthogonal polarization mode aligned with P_{155}. If so, the power-current characteristics captured at this direction should follow the solid gray curve in Fig. 2.18b. The experimental data for this direction are shown in Fig. 2.18c.

It appeared, that in the consecutive measurements the LP mode that took over the emission at the switching point in Fig. 2.18b, became stable and dominant regardless of the wafer temperature and the pump current. In other words, polarization switching is not maintained in the consecutive measurements, whereas the polarization direction remains inverted.

2.6 Summary and conclusions

In summary, this chapter presents our experimentally results on polarization properties of SML and SK QD VCSELs. Among single-transverse-mode devices that in the investigated range of currents and temperatures exhibit stable linearly polarized emission, polarization orientation of SK QD VCSELs changes from device to device. The distribution, however, achieves two maxima at the x (90) and y (0) directions corresponding to the main crystallographic axes. In this regard SK QD VCSELs resemble QW devices. On contrary, polarization orientation of all the investigated SML QD VCSELs is aligned with the y direction. Close to the lasing threshold this is also the case for the devices showing polarization instabilities. Five SK QD VCSELs (out of 24 investigated) abruptly switched their polarization to the orthogonal, linearly polarized mode when the wafer temperature was increased. Unlike in QW VCSELs however, switching has not been maintained in the consecutive measurements but the polarization direction remained orthogonal to that before the single switching event.

Seven SML QD VCSELs (out of 26 investigated) show very stable and reproducible polarization switching accompanied by polarization mode hopping between nonorthogonal, elliptically polarized states. Close to the lasing threshold the emission is linearly polarized. At some current it changes to stable elliptical polarization. The ellipticity and the polarization angle increase as the current is increased. Next, the region of polarization mode hopping between elliptically polarized, nonorthogonal modes starts. The distribution of the dwell time at a fixed current is exponential, which suggests that the hopping is stimulated by noise. To check which physical mechanism may be responsible for the observed polarization switching we perform a large-signal current modulation. The determined cut-off frequency is about 100 MHz. Since the intradot processes occur at a much faster timescale of a few tens of picoseconds we suspect that the switching is of thermal origin.

Our results constitute first experimental evidence of polarization switching in QD VCSELs and motivate further theoretical and experimental study to understand their polarization dynamics.

Chapter 3

Polarization mode hopping in QD VCSELs

3.1 Polarization mode hopping as a stochastic process

Many dynamical systems under the influence of noise show bistable hopping between two metastable states [148]. Classical picture of such a behavior is given by the Kramers escape of a particle over a potential barrier [149]. Since detail studies on polarization switching in QW VCSELs show that it is often accompanied by a noise-driven polarization mode hopping [150], these devices represent an ideal system for experimental study of such noise effects. Indeed, this issue has already been investigated for solitary devices [147, 150, 151, 152, 153] as well as for VCSELs subject to feedback [154, 155, 156] and optical injection [157]. The general conclusion is that the average dwell time between consecutive polarization hops depends on the potential barrier between the wells corresponding to distinct polarization states, and the strength of the spontaneous emission noise initiating the hopping.

Polarization mode hopping in QW VCSELs, if present, is only observed when the laser is biased in the vicinity of the current of an abrupt polarization switching. Since the polarization switching current changes from device to device, the average dwell time can be of the order of nanoseconds in devices showing polarization switching close to the lasing threshold but can also reach few seconds far from threshold, where the emission is dominated by the stimulated recombination. Consequently, the polarization switching current and the average dwell time can be regarded as still another parameters characterizing a particular device.

Current dependence on the average dwell time in QW VCSELs has been validated experimentally using a hot-spot technique [158], which enables external manipulation of the inherent anisotropies determining the barrier potential of a single device [147]. This studies show that the average dwell time

t_{dw} increases by 8 orders of magnitude when shifting the switching current J to larger values [147, 150]. For a symmetric potential this relationship is given by [150]:

$$t_{dw} = \frac{2\pi}{J\delta}\mathrm{erf}(\frac{J}{2}\sqrt{\frac{\delta}{R_{sp}}})\mathrm{erfi}(\frac{J}{2}\sqrt{\frac{\delta}{R_{sp}}}) \tag{3.1}$$

where δ is a difference between cross- and self-gain saturation coefficients, R_{sp} is the spontaneous emission noise strength, whereas erf and erfi are the error function and the imaginary error function, respectively. Using asymptotic series expansion of the error functions, Eq. 3.1 can be simplified to:

$$t_{dw} = \frac{4}{J^2}\sqrt{\frac{\pi R_{sp}}{\delta^3}}\exp{(\frac{J^2\delta}{4R_{sp}})}. \tag{3.2}$$

In Chapter 2 we have shown that also QD VCSELs can exhibit polarization switching. Its characteristics however, are in contrast to what is commonly observed in QW VCSELs. Here we show that the polarization mode hopping that accompanies the observed switching is also different: it takes place in an exceptionally wide range of currents and when the current is increased the average dwell time decreases by 8 orders of magnitude without any external manipulation of the inherent anisotropies.

3.2 Experimental results

The essentials of the observed polarization switching of the QD laser used in this section (it is different from the laser investigated in Sec. 2.4) are reflected in the polarization resolved power versus current characteristics shown in Fig. 3.1 The total output power is represented by black squares. Close to the lasing threshold the laser emits linearly polarized light along the P_0-direction (LP_1-mode, open circles; polarization angle is denoted as a subscript, e.g. P_{45} means 45 deg with respect to the y axis). When the current is increased, at a point I_A the power measured at the P_{90}-direction (black triangles) starts growing. This direction corresponds to the orthogonal, linearly polarized mode that is suppressed close to threshold (LP_2). The point I_A, therefore, indicates the onset of stable, elliptically polarized emission (EP_1). When the current is further increased, after a point I_A, the polarization ellipse of the EP_1-mode rotates gradually, such that at the point I_S its major axis is aligned with P_{-20}-direction. Likewise, its ellipticity increases gradually to 10%. At the point I_S another elliptically polarized mode EP_2 appears and the region of polarization switching accompanied by polarization mode hopping between these two modes starts. The major axis of EP_2 is aligned with P_{20}-direction, which shows that the modes EP_1 and EP_2 are non-orthogonal [159].

The amplitude of switching changes as a function of the polarizer orientation and achieves maximum at P_{45}- and P_{-45}-directions. The power-current

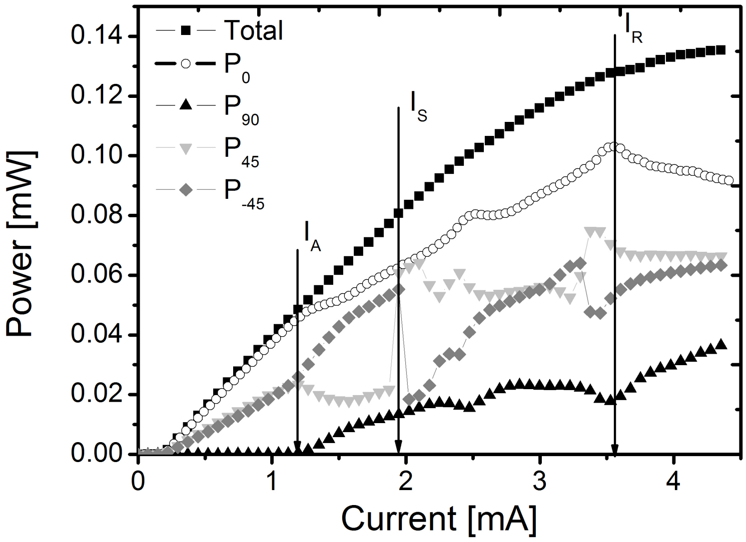

Figure 3.1: Polarization resolved power-current characteristics of the investigated QD VCSEL.

characteristics measured at these directions are represented in Fig. 3.1 by gray triangles and squares, respectively. The region of polarization mode hopping extends to a point I_R.

In order to have a better insight into the features of the observed polarization mode hopping, as a next step we present optical spectra captured with a piezoelectrically scanned plane mirror Fabry-Perot (FP) interferometer. Spectra shown in Fig. 3.2 are captured just after the point I_S, where the hopping is slower than the maximum bandwidth of the FP interferometer (50 Hz). The respective panels correspond to different orientations of the polarizer. All of them include a strong peak at frequency of 27 GHz and low-amplitude equidistant sidebands. We would like to note, that these sidebands appear slightly before the point I_S. As can be seen from Fig. 3.2, at the orientations of the polarizer denoted in the figure, the main spectral peak switches between two levels, which correspond to linear projections of the EP_1 and EP_2 modes. Such switching clearly shows that the main peak possesses an internal structure however, the resolution of the FP interferometer, estimated to be 2 GHz, is not enough to resolve the two modes spectrally. Nevertheless, the laser biased just after the point I_S stays in a given EP mode for a few seconds and, therefore, it is possible to find, with sufficient precision, the orientations of the polarizer at which the individual spectral components achieve their maxima. In the case shown in Fig. 3.2a, the peak represented by the black curve achieves maximum at P_{20} and, therefore, it corresponds

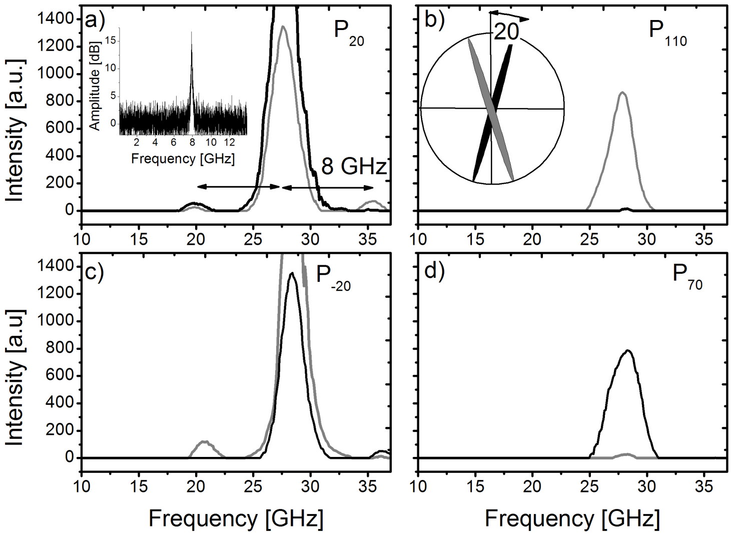

Figure 3.2: Polarization resolved optical spectra at $I = 1.85$ mA for different orientations of the polarizer (P). The inset in panel a) shows RF spectrum captured at P_{45}. Polarization angle is denoted as a subscript, e.g. P_{20} means 20 deg with respect to the y axis

to the mode which we have marked as EP_2. At a certain moment the laser emission switches to the EP_1-mode so that the amplitude of the main peak drops to a value corresponding to a linear projection of EP_1 mode on P_{20}, see the gray curve in Fig. 3.2a. Likewise, as shown in Fig. 3.2c, the EP_1-mode achieves its maximum at P_{-20} (gray curve). The black curve in this figure corresponds, therefore, to linear projection of EP_2 on P_{-20}. The so determined orientations of the major axes of the EP_1 and EP_2 modes prove their nonorthogonality. Fig. 3.2b shows FP spectra captured at orientation of the polarizer corresponding to the minor axis of EP_2, i.e. P_{110}, black curve. The gray curve in this figure represents a linear projection of EP_1 on P_{110}. Likewise, Fig. 3.2d shows FP spectra at P_{70}, which correspond to minor axis of the EP_1 mode, gray curve, and a linear projection of EP_2 mode, black curve, respectively. Both Fig. 3.2b and Fig. 3.2d prove, that the EP modes involved in polarization mode hopping, indeed, possess residual ellipticity.

As already mentioned, the main spectral component in Fig. 3.2 possesses low-amplitude, equidistant sidebands. They appear near the I_S point, which is manifested by a strong peak at 8 GHz in the radio frequency spectrum (RF), see the inset in Fig. 3.2a. Note, that similar observations have been reported for polarization switching involving dynamical states in QW VCSELs [126], i.e. the increase of the ellipticity angle close to the switching point has been

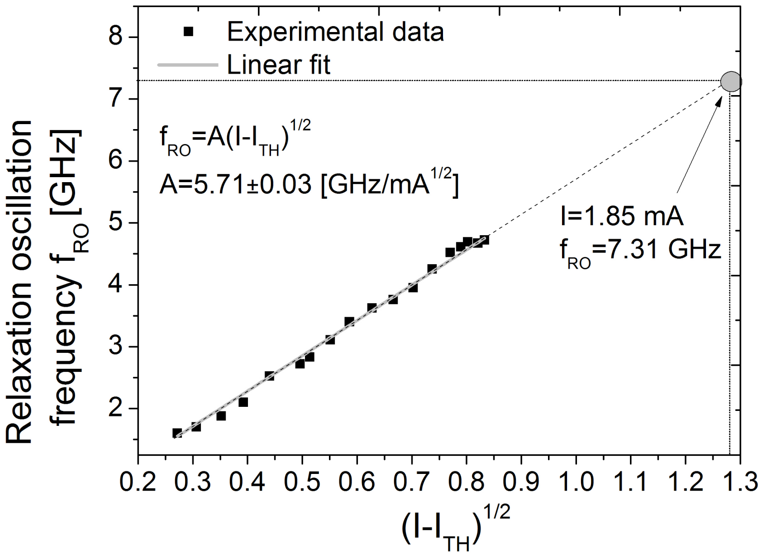

Figure 3.3: Relaxation oscillation frequency (black squares) as a function of the square root of the pump current. The solid gray curve is a linear fitting.

accompanied by the appearance of sidebands in the optical spectrum. Their frequency has been attributed to the effective birefringence expressed as the sum of the linear birefringence observed at the lasing threshold and the nonlinear contributions due to saturable dispersion and spin dynamics [126].

In Fig. 3.3 we show the relaxation oscillation frequency (f_{RO}) as a function of the square root of the pump current above threshold. A linear interpolation of the experimental data with:

$$f_{RO} = A\sqrt{I - I_{TH}} \tag{3.3}$$

gives a proportionality constant A of 5.71±0.03 GHz/mA$^{0.5}$. We then use Eq. 3.3 to extrapolate the value of the relaxation oscillation frequency at the current of 1.85 mA. The value of 7.31 GHz is close to the frequency of 8 GHz of the RF peak shown in Fig. 3.2a and, therefore, we attribute the sidebands to a low-amplitude time dependent modulation of the laser response at the frequency of the relaxation oscillations excited by polarization instabilities.

As already mentioned, the region of polarization mode hopping starts at the point I_S and extends over a wide range of currents up to I_R. This is in sharp contrast to polarization mode hopping in QW VCSELs, which occurs only when the laser is biased close to the abrupt polarization switching [150]. Another distinctive feature is its dynamics. Examples of time traces captured at various currents and the polarizer orientation of P_{45} are shown in Fig. 3.4. Just after I_S, at $I = 1.81$ mA, polarization mode hopping is asymmetric, i.e.

the laser stays most of the time in one EP mode and exhibits rapid switches to the other mode every few seconds, see Fig. 3.4a. At around $I = 2.0$ mA the hopping becomes symmetric, while the average dwell time decreases to microseconds, see Fig. 3.4b. At still larger currents the average dwell time decreases to nanoseconds (see Fig. 3.4c,d,e), although there is also a subtle increase at around $I = 3.2$ mA (see Fig. 3.4d).

Current dependence of the dynamics of the observed polarization mode hopping is summarized in Fig. 3.5. Contrary to the scaling of the dwell time in QW VCSELs, the average dwell time in QD VCSELs decreases with injection current. This decrease is by 8 orders of magnitude: from seconds to nanoseconds and is achieved without any modifications of the internal anisotropies. The observed scaling happens in polarization mode hopping range of currents as wide as 8 times the threshold current.

After the point I_R polarization mode hopping disappears, but, unlike in the polarization switching involving dynamical states in QW VCSELs, the laser does not switch to the LP_2 mode, i.e. polarization mode that is suppressed close to threshold. Instead, it exhibits two-mode emission with dominant LP_1, which also dominates before the onset of elliptically polarized emission, and weaker LP_2, see Fig. 3.6. Moreover, each LP mode is accompanied by a single low-amplitude peak of the same polarization. The RF spectrum shown in the inset of Fig. 3.6 includes two strong beating signals. One of them, at 5.58 GHz, corresponds to the frequency splitting between the two dominating LP modes and, therefore, can be regarded as corresponding to the birefringence splitting between these two modes. The remaining spectral component appears at 9.8 GHz and corresponds to the frequency splitting between LP mode and a small-amplitude peak of the same polarization, which can be again interpreted as slightly excited relaxation oscillations at this current.

3.3 Summary and conclusions

In this chapter we have presented experimental characterization of optical spectra and dynamics of polarization mode hopping in quantum dot vertical-cavity surface-emitting lasers. In contrast to what is observed in QW VCSELs, polarization mode hopping takes place between nonorthogonal elliptically polarized modes with frequency splitting smaller than 2 GHz and is observed in an exceptionally wide range of currents. Similarly to polarization switching involving dynamical states in QW VCSEL, the increase of the ellipticity of the lasing polarization component close to the point at which polarization switching starts has been accompanied by the appearance of sidebands in the optical spectrum. We attribute these sidebands to a low-amplitude time dependent modulation of the laser response at the frequency of the relaxation oscillations excited by polarization instabilities.

The most apparent difference between observed scenario and polarization

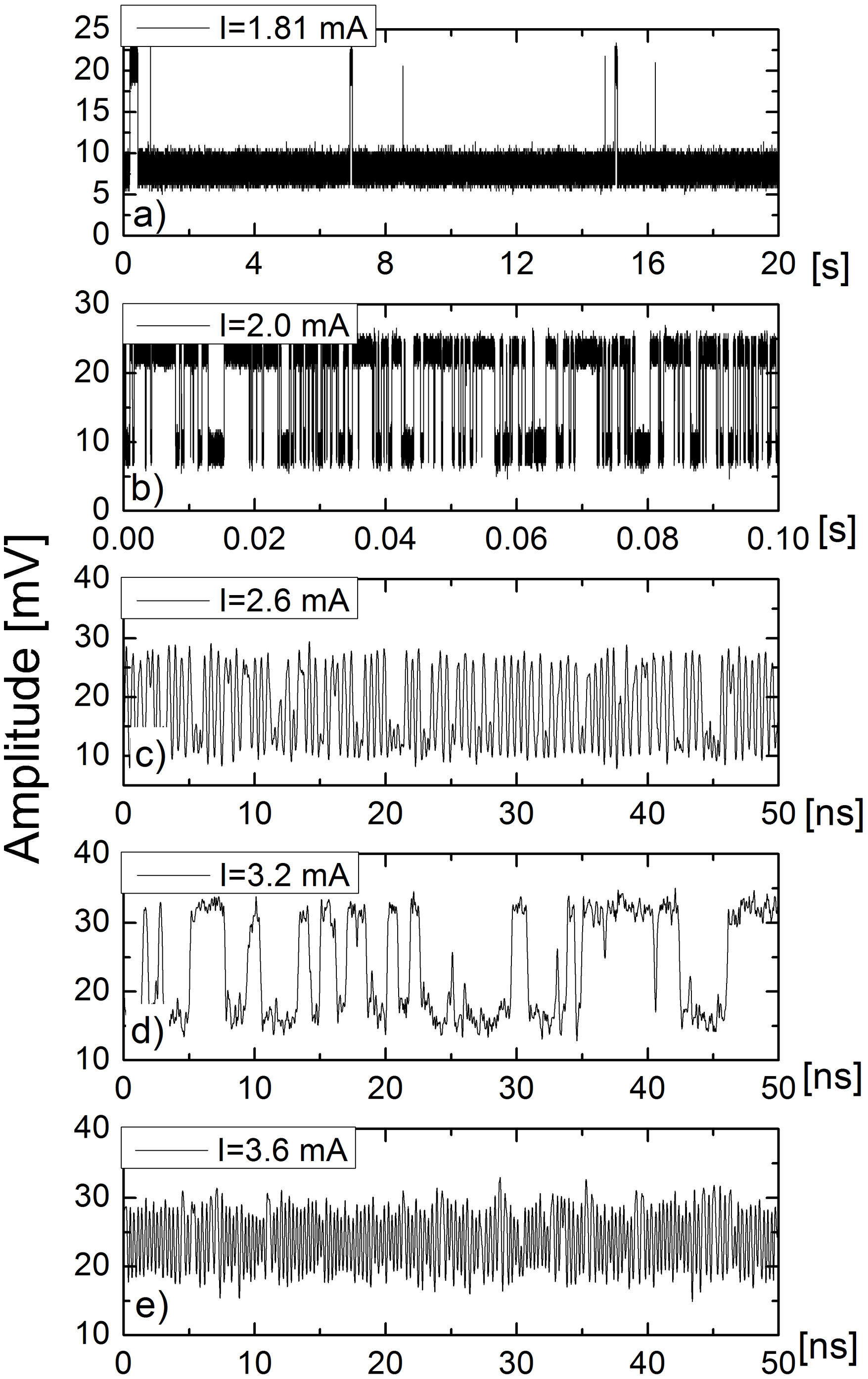

Figure 3.4: Time traces at the current of a) 1.81 mA, b) 2.0 mA, c) 2.6 mA, d) 3.2 mA, e) 3.6 mA at the polarizer direction corresponding to the maximum amplitude of switching, i.e. P_{45}.

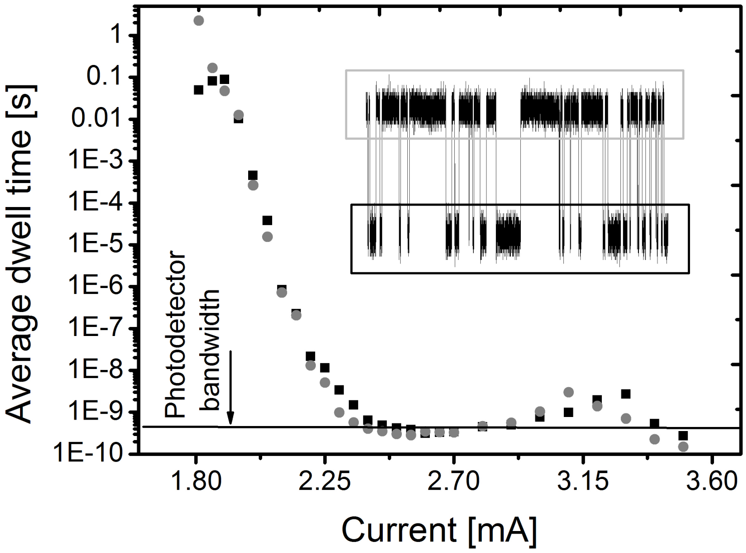

Figure 3.5: Experimental data for the current dependence of the average dwell time for both *EP* modes calculated from the time traces captured at the polarizer orientation of P_{45}.

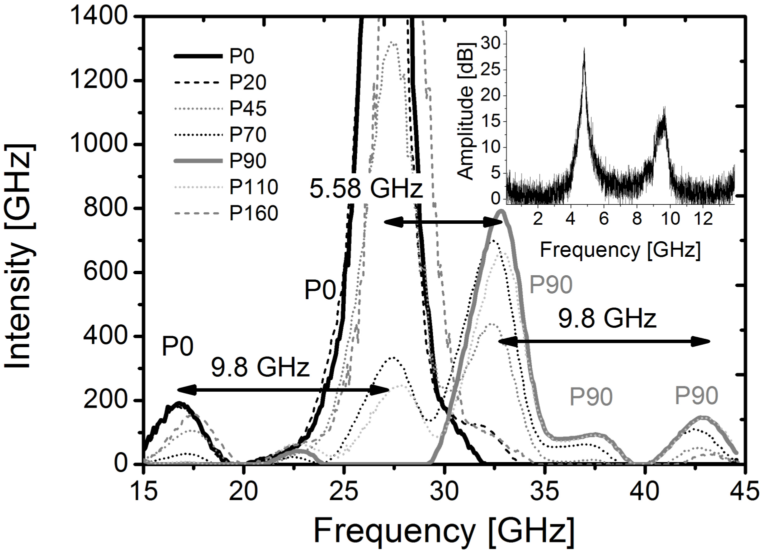

Figure 3.6: Polarization resolved optical spectra at $I = 4.45$ mA. The inset shows RF spectrum captured at P_{45}

switching involving dynamical states is that instead of switching to the *LP* mode that is suppressed close to threshold, after the region of polarization mode hopping the laser exhibits two-mode emission with dominant *LP* mode that dominates also before the onset of elliptically polarized emission, and a weaker orthogonal one. The frequency splitting between these two modes can be regarded as a measure of birefringence and is of 5.58 GHz. Each *LP* mode is accompanied by a single low-amplitude peak of the same polarization split in frequency by 9.8 GHz, which we again interpret as excitation of relaxation oscillations at this current.

Another distinctive feature of the observed polarization mode hopping is its dynamics. The average dwell time decreases when the current is increased. Interestingly, such behavior is observed without any external manipulation of the inherent anisotropies. To our best knowledge, this is the first observation of such a diversified, in terms of time scaling, dynamics of polarization mode hopping in a single VCSEL.

Chapter 4

Nonlinear dynamics of optically injected QD lasers

As any semiconductor laser, QD lasers are sensitive to both the light reflected back from the elements of the optical system (optical feedback), i.e. lenses, fiber facet etc., and to the light injected externally from another laser commonly referred to as master (optical injection). Their potentially small linewidth enhancement factor, however, makes them ideal candidates for the investigation of new dynamics not seen in QW EEL and QW VCSELs. In this and the following chapter we will focus on optically injected QD EEL. Basically, optical injection is used to stabilize the operation of the injected (slave) laser by locking its frequency to that of the master one [89]. However, many theoretical and experimental studies proved that under the unlocked conditions the slave laser can exhibit rich varieties of dynamics including four-wave mixing, period-doubling route to chaos, self-pulsations, excitability etc., and, therefore, it is an attractive configuration for fundamental bifurcation study of nonlinear optical systems [50, 90]. In this chapter we first give short overview on the bifurcations that we will encounter investigating nonlinear dynamics of optically injected QD laser system and then summarize recent experimental results on this topic. Next, we present theoretical model used to explain these findings and discuss our extension of this model which takes into account QD excited states. As a main part of this chapter we present our numerical results on the impact of the relaxation and the capture times on the dynamics of such a system. We put special attention to dynamics resulting in a pulsed output, i.e. excitability and self-pulsations and identify the role of the excited states in such an emission. Next, we study the dynamics of self-pulsation in the presence of spontaneous emission noise so that we can compare it with the dynamics experimentally reported for excitable pulses [160]. Specifically, we show how the interpose time distribution changes as a function of detuning and noise strength. Finally, we investigate the performance of a system in which an attenuated/distorted information signal acts as a master laser and switches a slave QD laser between the regions of locking and self-pulsations.

4.1 Bifurcations of optically injected semiconductor lasers

The behavior of an optically injected semiconductor laser depends on the properties of injected light, i.e. its power and frequency; specifically, the detuning from the slave laser frequency. For brevity, we will refer to them as injection strength S_m and detuning Δ, respectively. The most common approach to characterize the dynamics of such a system relies on detecting various bifurcations of stationary points and limit cycles[1] and presenting them on the so called bifurcation diagram, i.e. (S_m, Δ) plane. Note however, that the same term is sometimes used to refer to diagrams showing one phase space quantity plotted against a single bifurcation parameter. To distinguish between these two types of diagrams, we will refer to them as 2-parameter and 1-parameter bifurcation diagrams, respectively. 2-parameter bifurcation diagram for optically injected QW laser is presented in Fig. 4.1. Each curve corresponds to a specific bifurcation (a qualitative change in the behavior of the laser). SN (blue) is a saddle-node bifurcation, H (red) is a Hopf bifurcation, PD (green) are period doubling bifurcations, T (gray) is a torus bifurcation, SL (brown) is a saddle-node of limit cycles bifurcation. CMX (pink) refers to the regions of complex dynamics, possibly chaotic [162]. In the following paragraphs we will briefly characterize each of these bifurcations.

The locking region, where the slave laser emits at a constant power and at the frequency of the master laser, is bordered by the curves corresponding to bifurcations of stationary points, namely the Hopf and the saddle-node bifurcations [50]. Changes of any of the bifurcation parameters that shift the laser operation to the locking region by saddle-node bifurcation lead to a creation of two stationary points, namely a saddle and a node, see Fig. 4.2. They correspond to unstable and stable equilibrium, respectively, the latter being associated with the locked state. In optically injected QW lasers these two points are created in a saddle-node on limit cycle bifurcation, also known as a saddle-node on invariant circle [164]. The difference between these two bifurcations is explained in Fig. 4.3. In the situation shown in the left panel in Fig. 4.3a there are three coexisting solutions: saddle (white circle), node (black circle) and a limit cycle. When the bifurcation parameter changes the saddle approaches the node. Next, they coalesce and annihilate each other, see the

---

[1] Limit cycle is an isolated closed trajectory in the phase space, which means that the neighbouring trajectories spiral either toward (stable or attracting limit cycle) or away (unstable limit cycle) from it [161]. The existence of a stable limit cycle suggests that the system can exhibit self-sustained oscillations even in the absence of external forcing, whereas the amplitude of these oscillations does not depend on the initial conditions but on the structure of the system.

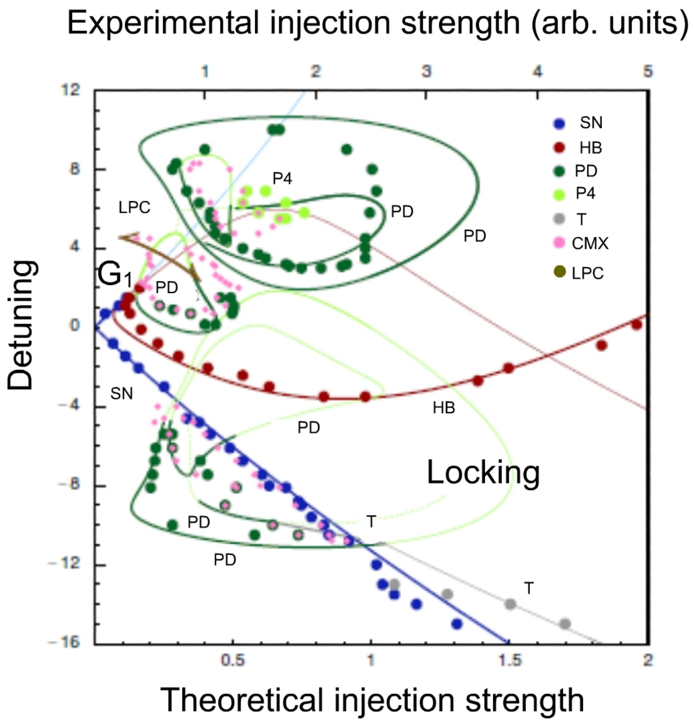

Figure 4.1: 2-parameter bifurcation diagram (plotted as curves) overlaid with the experimentally measured stability diagram (plotted as dots) for optically injected QW laser. Each curve corresponds to a specific bifurcation (a qualitative change in the behavior of the laser). SN (blue) is a saddle-node bifurcation, HB (red) is a Hopf bifurcation, PD (dark green) is period doubling bifurcation, P4 (light green) is period-4 bifurcation, T (gray) is a torus bifurcation, LPC (brown) is a saddle-node of limit cycles bifurcation. CMX (pink) refers to the regions of complex dynamics, possibly chaotic. G_1 is a codimension-2 point at which saddle-node and Hopf bifurcations cross each other. Taken from [162]. Note, that the detuning here is defined opposite to the convention used in the original paper on optical injection in QD lasers [95] and used in our modeling.

middle and the right panel in Fig. 4.3a. Because the node representing stable equilibrium disappears, the trajectory describing the evolution of the system jumps to the attracting limit cycle. In the saddle-node on limit cycle bifurcation (see Fig. 4.3b) the period of the limit cycle (which in optically injected QW laser exists outside the locking region due to wave-mixing effects) goes to infinity at the saddle-node bifurcation and becomes the so-called invariant circle, which connects both created stationary points. It is called invariant because any solution starting on the circle remains on it [164, 163]. When

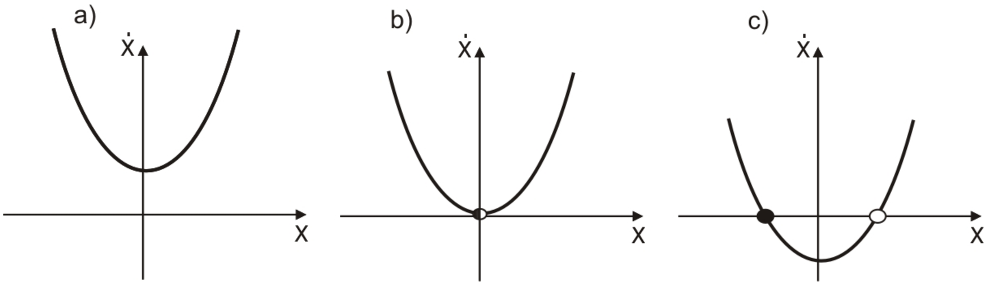

Figure 4.2: Typical example of a saddle-node bifurcation in the first order system given by: $\dot{x} = r + x^2$, where r is a bifurcation parameter. Changes of r lead to a creation of two stationary points, namely a saddle (white circle) and a node (black circle). They correspond to unstable and stable equilibrium, respectively. In reference to optically injected QW laser, changes of any of the injection parameters that shift the laser operation to the locking region by saddle-node bifurcation lead to a creation of a saddle and a node, the latter being associated with the locked state.

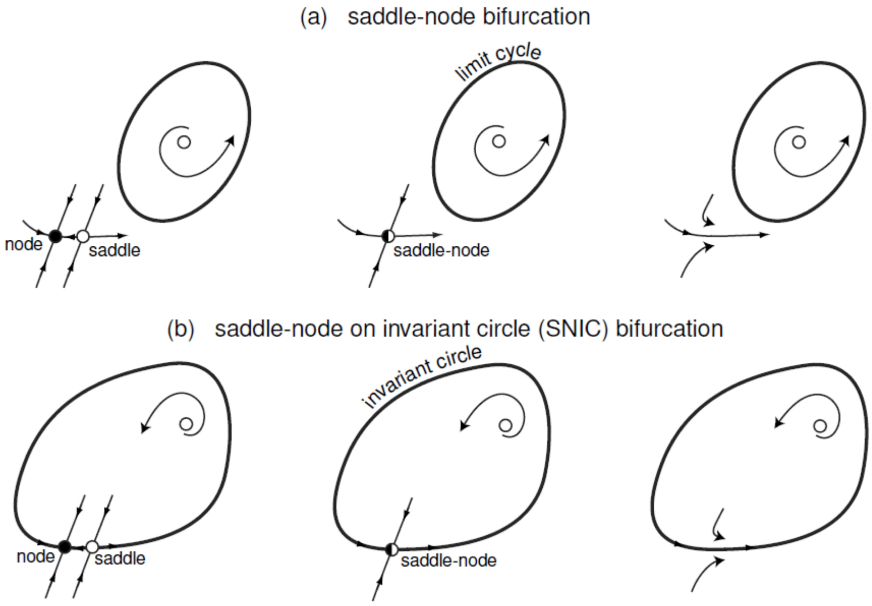

Figure 4.3: a) Saddle-node and b) saddle-node on invariant circle bifurcations. Taken from [163].

the locking region is left through the Hopf bifurcation, the stable equilibrium loses stability and gives way to an attracting limit cycle so that the laser shows intensity oscillations at the relaxation oscillation frequency. Both, the saddle-node and the Hopf bifurcation curves cross in the injection parameter plane at the codimension-two points[2] G_1 and G_2. The dynamics of the optically injected QW laser system becomes complex in the vicinity of these points [165, 166]. Moreover, the solutions emerging from the respective bifurcations invert their stability at such points.

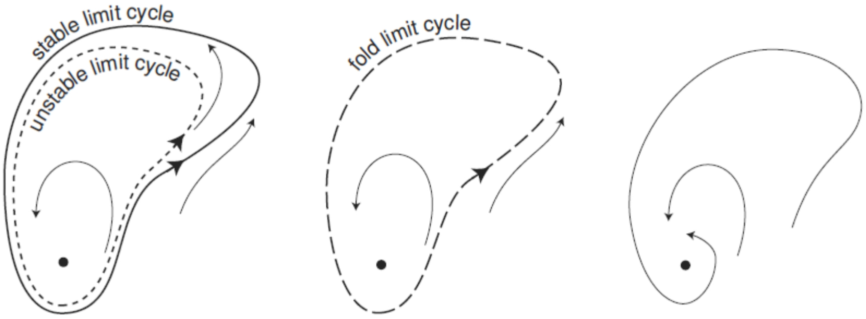

Figure 4.4: Saddle-node of limit cycle bifurcation. Taken from [163].

The limit cycle that is created at the Hopf bifurcation may undergo a period-doubling bifurcation at which, as its name suggests, the laser intensity starts oscillating with a doubled period. Moreover, the limit cycle may undergo a cascade of period-doublings which eventually leads to a chaotic behavior [167].

A stable limit cycle can disappear (or appear) through a saddle-node of limit cycles bifurcation. It is very similar to the saddle-node of stationary points. When the bifurcation parameter is changed, stable limit cycle is approached by the unstable one. At the bifurcation point they coalesce and then both disappear, see Fig. 4.4.

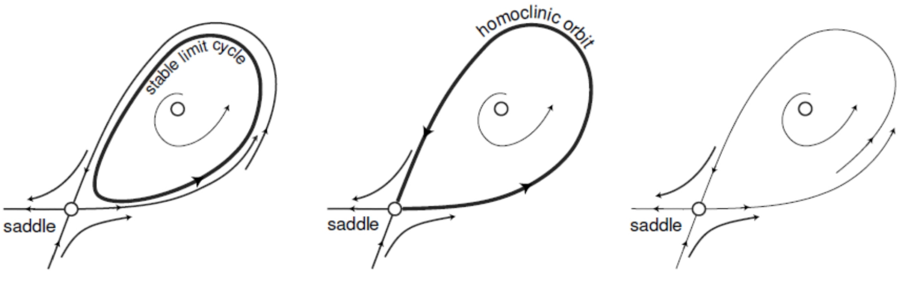

Figure 4.5: Saddle-homoclinic orbit bifurcation. Taken from [163].

---

[2] The term codimension-2 means, that to achieve this type of bifurcation one needs to tune two bifurcation parameters. Likewise, bifurcations achieved by tuning a single parameter are referred to as being codimension-1 [161].

The last bifurcation discussed in this section is a saddle homoclinic orbit bifurcation. It occurs when a saddle point collides with a periodic orbit. Note, that the saddle has one stable and one unstable direction on the phase plane. Both directions are associated with the orbits that are commonly referred to as stable and unstable manifold, respectively. At the bifurcation point, the periodic orbit connects both manifolds of the saddle and becomes a homoclinic orbit of infinite period, see Fig. 4.5.

In the presence of noise both, saddle-node on limit cycle and saddle-homoclinic orbit bifurcations can result in a pulsed behavior.

4.2 Optical injection in QD lasers: experimental background.

All the bifurcations described in Sec. 4.1 will be helpful to characterize the nonlinear dynamics of optically injected system with QD laser as a slave. First experimental and theoretical studies on this topic show [95, 160, 168], that QD laser can stably synchronize with the master over a significant detuning range, as in the region 3 in Fig. 4.6, but can also exhibits quite complex behavior, however, only on the positive unlocking boundary [95]. The latter includes regions where the laser responds to the injected optical signal in a form of the so-called single (6S) or double (6D) excitable pulses.

The concept of excitability is explained in Fig. 4.7. Unperturbed excitable system remains in the 'rest' state (full circle in middle-column plot) [169]. If it is optically injected semiconductor laser then the rest state corresponds to the locked state represented by a node. To fire excitable pulses the system also needs an unstable state (empty circle in middle-column plot), e.g. represented by a saddle point. Small perturbation will result only in a small-amplitude linear response so that the laser immediately returns to the locked state, see Fig. 4.7a. However, if the perturbation is strong enough to kick the system to the other side of the unstable point (of the unstable manifold of a saddle point [50]), then the response is strongly nonlinear and accompanied by a large excursion of the system variables through phase space before coming back again to the locked state [169]. As a results the laser fires a pulse, see Fig. 4.7b,c. The strength of the perturbation needed to fire a pulse, the so-called excitability threshold, is roughly given by the distance between the saddle and the node [50]. Since close to the saddle-node bifurcation this threshold becomes smaller, it becomes possible to observe excitable pulses stimulated by noise. While firing a pulse the system is refractory, which means that it takes a certain time before another excitable pulse can be fired, see Fig. 4.7d,e. Although excitability is quite common in nature [169, 170, 171] and has already been reported for a variety of laser systems including lasers with optical feedback [96], [97] and lasers with saturable absorber [98], the

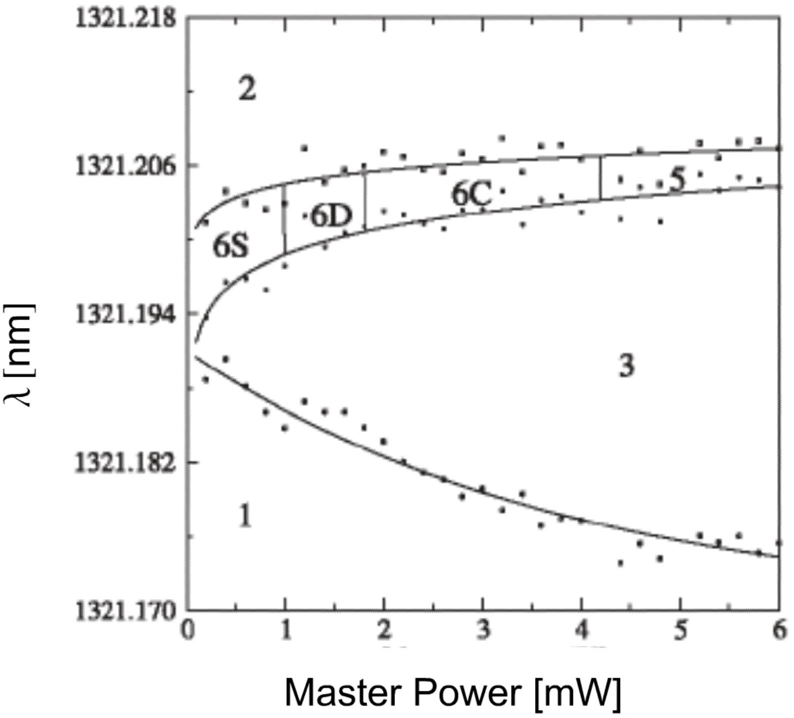

Figure 4.6: Experimental map of bifurcations for optically injected QD laser. Region 3 corresponds to locked operation, which means that the slave laser emits at a constant power whereas its frequency is locked to that of the master laser. In regions 1 and 2 the slave laser is unlocked. In regions $6S$ and $6D$ the laser fires single and double excitable pulses, respectively. Region $6C$ corresponds to a random switching between locked and unlocked states, whereas region 5 to random switching between two locked states. Taken from [95].

results presented in [95] constitute the first experimental observation of such a dynamics in optically injected laser system.

Despite being excitable, on the positive unlocking boundary QD lasers can also exhibit random switching between locked state and complex multi-pulse transient (region $6C$ in Fig. 4.6), between locked and unlocked states (region 5) and between two locked states. At large value of the injection strength the transition from locked to unlocked region occurs without any observed instabilities. As reported in [160], excitable pulses can also be observed on both positive and negative unlocking boundaries and to have such an emission one needs a laser with small linewidth enhancement factor and

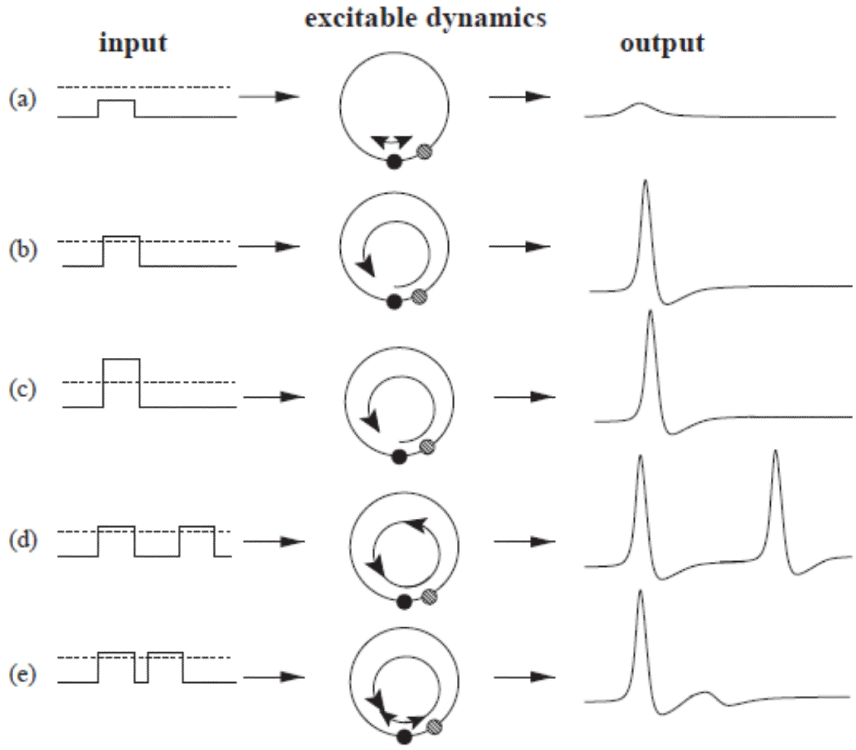

Figure 4.7: Schematic explanation of excitability. Left column represents perturbation, which cause different kinds of responses (right column). The excitability threshold is represented by a dashed line. The middle column represents phase space with the full and empty circles corresponding to stable and unstable states, respectively. a) Perturbation below the excitability threshold results in a small amplitude motion around the stable state. b) Input exceeding the threshold kicks the system to the other side of the unstable point which leads to a large-amplitude excursion of the system variables in the phase space. As a result the system fires a pulse. c) Increasing the strength of the perturbation does not change the shape of the spike significantly. d) and e) While firing a pulse the system is refractory, which means that if the input pulses are too close, the system does not respond noticeably to the second perturbation. Taken from [169].

highly damped relaxation oscillations. The shape of excitable pulses remains invariant over a wide range of injection parameters but the mean time between consecutive pulses depends strongly on the detuning [95], i.e. when the detuning is increased they become more frequent and more periodic. The distribution corresponding to rare pulses shows a Kramers-like exponential decay indicating random noise-induced escape, while the distribution close to

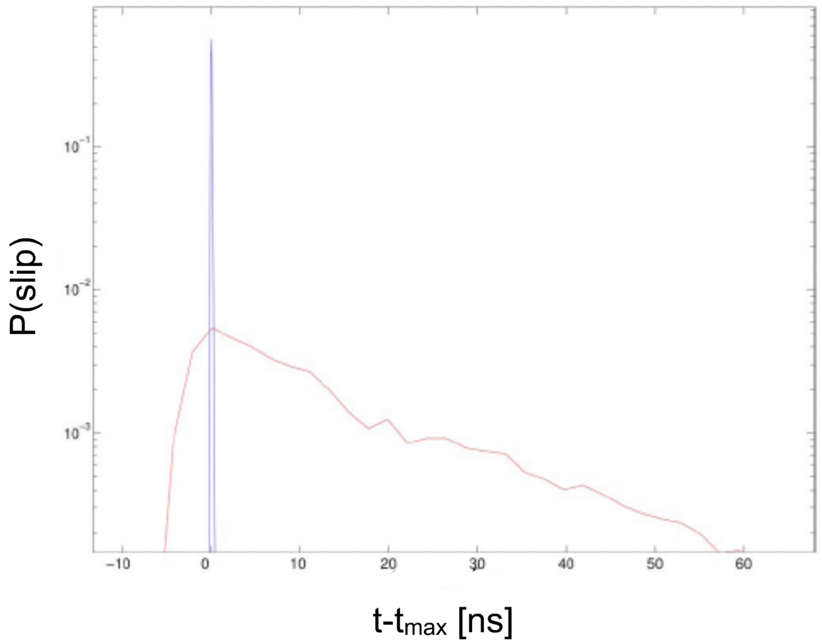

Figure 4.8: Probability distributions of the time between excitable pulses for different values of the detuning. The distribution corresponding to rare pulses shows a Kramers-like exponential decay indicating random noise-induced escape, while the distribution close to the unlocking boundary is sharply peaked. Taken from [160].

the unlocking boundary is sharply peaked, see Fig. 4.8. The pulses are observed over a wide range of detuning, i.e. from -620 MHz to -1.15 GHz and from 800 MHz to 1.15 GHz (the range of locking with no pulses was approximately 1.4 GHz). Since in the locking region the slave field oscillates at the master laser frequency and at a fixed relative phase, the observed excitability has been attributed to phase slips [160].

4.3 Theoretical model

As specified in Sec. 1.4, one of our goals is to better understand the overall dynamics of optically injected QD laser system by diving into the physics of QDs. Extensive studies on optically injected QW lasers proved that the dynamical properties of such a system can be well described by the rate equations [50, 89, 90]. They can be derived from a more fundamental, though still semi-classical, approach in which the laser field is treated classically and described by Maxwell's equations, whereas the gain medium is treated quantum mechanically. A rate equation model for optically injected QD lasers has been presented in [95]. It is expressed by three mutually coupled variables, namely the complex amplitude of the electric field E of the slave laser, the occupation probability N_w of the QW surrounding the QDs (as in DWELL structures) or the wetting layer considered as a QW, and the occupation probability of the QDs f_{QD}. f_{QD} is defined as the number of carriers in the QDs normalized to the product of the total number of QDs N_{QD} and the degeneracy of the energy level, whereas N_w as a number of carriers in the QW normalized to the number of quantum dots. The complete model reads:

$$\frac{\mathrm{d}E}{\mathrm{d}t} = \frac{1}{2}v_g g_0 (\frac{2f_{QD}-1}{1+\epsilon|E|^2} - \frac{\gamma_s}{v_g g_0})(1+i\alpha)E + iE\Delta + \sqrt{\frac{\gamma_s^2 S_m}{\hbar\omega}}, \tag{4.1}$$

$$\frac{\mathrm{d}N_w}{\mathrm{d}t} = -\gamma_N N_w + \frac{J_{QD}}{q} - 2C^0 N_w (1-f_{QD}), \tag{4.2}$$

$$\frac{\mathrm{d}f_{QD}}{\mathrm{d}t} = -\gamma_q f_{QD} + C^0 N_w (1-f_{QD}) - v_g \sigma (\frac{2f_{QD}-1}{1+\epsilon|E|^2})|E|^2. \tag{4.3}$$

The respective parameters and their values as used in the original paper [95] are summarized in Tab. 4.1.

The relationship between the optical gain coefficient g_0 and the interaction cross section of carriers in the dot with the electric field σ is given by [95, 172]:

$$\sigma = \frac{g_0}{2N_{QD}^{2D}}\frac{L}{\Gamma}, \tag{4.4}$$

where L is the thickness of the QD layer.

The first two terms on the right-hand side of Eq. 4.1 account for the net gain. The remaining terms describe the injected signal, that is, its frequency detuning from the slave laser frequency and its electric field amplitude. Eq. 4.2 for the occupation of the QW N_w accounts for the decay of carriers in the WL due to spontaneous and/or nonradiative recombination, the pumping and the capture of carriers to the QDs, respectively. Finally, the equation Eq. 4.3 for the occupation of QDs accounts for the decay of carriers in QDs due to spontaneous and/or nonradiative recombination, capture of carriers to QDs and stimulated recombination, respectively.

As it has been discussed in Sec. 1.2.4, due to a small energy level separation for holes in the valence band and the p-doping, which leads to an excess of holes in QDs, the capture, relaxation and escape rates for holes are much faster than the respective values for electrons. The model, therefore, assumes that the overall dynamics is governed only by electrons. Furthermore, there is only single, two-fold degenerate confined energy level in QDs - the ground state GS, see Fig. 4.9a. Carriers are first injected into the QW and then are captured into the QDs [95, 172]. Due to the Pauli blocking principle, the capture rate depends on the actual occupation of the QDs. Moreover,

Table 4.1: Summary of the parameters used in the models

Parameter	Unit	Value	Description
γ_s	ns^{-1}	590	Photon decay rate.
γ_N	ns^{-1}	1	Spontaneous/nonradiative carrier decay rate for carriers in QW.
γ_q	ns^{-1}	1	Spontaneous/nonradiative carrier decay rate for carriers in QDs.
C^0	ps^{-1}	1.02	Capture rate from the quantum well to the empty dot.
J_{QD}	A	6.73×10^{-10}	Pump current per QD.
σ	nm^2	0.6	Interaction cross section of the carriers in the dot with the electric field.
α		1.2	Linewidth enhancement factor.
q	C	1.602×10^{-19}	Electric charge.
v_g	m/s	0.833×10^{8}	Group velocity.
ϵ	m^3	2×10^{-22}	Gain saturation coefficient.
g_0	cm^{-1}	72	Linear optical gain coefficient.
ω	fs^{-1}	1.45	Master laser frequency.
Δ	GHz		Frequency difference between the slave and the master laser (detuning).
S_m	$\mathrm{J/m}^3$		Energy density of the master laser (injection strength).

the model assumes that the inhomogeneous broadening has a Gaussian shape with its FWHM being smaller than k_BT (T is the carrier temperature) and neglects any temperature effects on the population of QDs [173]. Since thermal escapes are neglected, carriers captured into the QDs either recombine spontaneously/nonradiatively or contribute to lasing. Even though such an approach can reproduce qualitatively well the experimental findings obtained at room temperature, the model seems to be better suited to describe QD laser operating in a low-temperature range with non-equilibrium distribution of carriers [174]. This is because in this regime WL does not reabsorb carriers already captured by QDs, which, in turn, can be regarded as if the QDs were decoupled from the WL and each other. As a result the occupation of the GS increases with increasing the pump current and, consequently, the laser can saturate to $f_{GS} = 1$. This is not the case for devices operating at room temperature [174] when thermal escapes are more probable. As shown in [31], the escape time τ_{esc} can be derived by assuming that the system reaches a quasi-Fermi equilibrium in the absence of external excitations so that when there is only single energy level within a QD the expression for the escape time takes the form:

$$\tau_{esc} = \frac{4}{C^0} \exp(\frac{E_{WL} - E_{QD}}{k_b T}) \tag{4.5}$$

Its value grows exponentially with the difference between the energy attributed to the wetting layer and the energy of carriers within QDs. In QD lasers the ratio of the capture and escape times is typically much smaller than one and under such conditions the escape term can be neglected [175, 176] allowing $f_{GS} = 1$. However, we would like to note that widely accepted models that allow $f_{GS} = 1$ at the room temperature [30, 31] have been shown to be successful in explaining many static and dynamical characteristics of QD lasers.

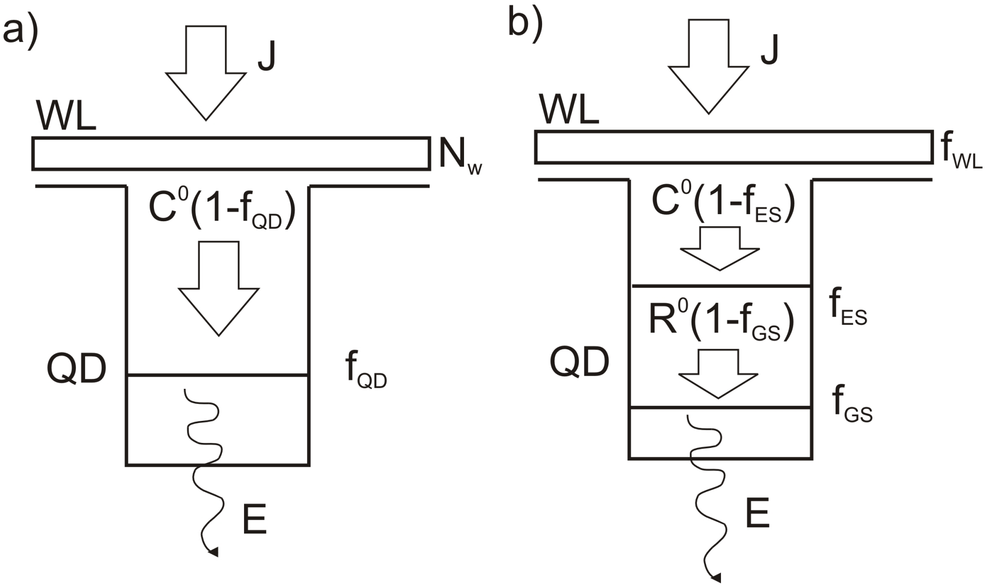

Figure 4.9: Schematic representation of a QD laser system as a) in the original model of optically injected QD laser [95] and b) in the extended model accounting for the intradot relaxation.

Theoretical analysis with the described model showed good qualitative agreement with the experiment [95] and, therefore, we have chosen it as a base for our further study. In particular we want to check how the nonlinear dynamics of optically injected QD laser is influenced by the intradot relaxation and to this aim we need to account for the excited states. In our approach, therefore, carriers captured from the wetting layer WL achieve the lasing QD ground state GS by successive transitions through a single QD excited state ES, see Fig. 4.9b. These processes are characterized by the capture τ_c and the relaxation times τ_o, respectively. Both time constants have already been shown to influence the performance of QD lasers in terms of modulation bandwidth and threshold current [57, 99, 100]. Similarly to [57], we assume that the ES

is four-fold degenerate and that the gain saturation comes naturally with the Pauli blocking terms. Since the original model proved to work well without accounting for thermal escapes, in our regular study we will also neglect this mechanism and focus only on the contributions of the excited states.

Extended model comprises single equation for the complex amplitude of the electric field E of the GS emission and three equations for the occupation probabilities f_{GS}, f_{ES}, f_{WL}, i.e. the number of carriers in the GS, ES and WL, respectively, normalized to the product of the total number of QDs, N_{QD}, and the degeneracy of the respective states (the number of carriers in the WL is normalized to the number of QDs only). The occupation probability of the ground state f_{GS} is, therefore, equivalent to f_{QD} of Eq. (4.1-4.3). The respective equations read:

$$\frac{\mathrm{d}E}{\mathrm{d}t} = \frac{1}{2} v_g g_0 (2f_{GS} - 1 - \frac{\gamma_s}{v_g g_0})(1 + i\alpha)E + i\Delta E + \gamma_s \sqrt{\frac{S_m}{\hbar\omega}} + E_{noise}, \tag{4.6}$$

$$\frac{\mathrm{d}f_{WL}}{\mathrm{d}t} = \frac{J_{QD}}{q} - \gamma_N f_{WL} - \frac{f_{WL}(1 - f_{ES})}{\tau_c}, \tag{4.7}$$

$$\frac{\mathrm{d}f_{ES}}{\mathrm{d}t} = -\gamma_q f_{ES} + \frac{f_{WL}(1 - f_{ES})}{4\tau_c} - \frac{f_{ES}(1 - f_{GS})}{\tau_o}, \tag{4.8}$$

$$\frac{\mathrm{d}f_{GS}}{\mathrm{d}t} = -\gamma_q f_{GS} + \frac{2f_{ES}(1 - f_{GS})}{\tau_o} - v_g \sigma (2f_{GS} - 1)|E|^2. \tag{4.9}$$

The noise term in Eq. 4.6, given by:

$$E_{noise} = \sqrt{2\beta_{sp}\gamma_q f_{GS} N_{QD}^{3D}} \varsigma \tag{4.10}$$

accounts for the spontaneous emission noise. ς in Eq. 4.10 is a white noise of unitary variance and zero mean value, whereas N_{QD}^{3D} is the volume density of QDs. The strength of the noise term is driven by the spontaneous recombination factor β_{sp}. $I = |E|^2$ represents the intensity (photons density) of the light emitted by the GS mode. Unless otherwise stated, the values of the model parameters are consistent with those given in Tab. 4.1.

Since each QD comprises two energy levels, there are two possible escape channels for carriers: from the ground state to the excited state and from the excited state to the wetting layer. As already discussed, the latter transition can usually be neglected. The escape to the excited state would require the inclusion of two additional terms in the model: one in the equation Eq. 4.8 for the occupation of the excited state:

$$+ \frac{f_{GS}(1 - f_{ES})}{2\tau_{esc}^{GS-ES}}, \tag{4.11}$$

and another one in the equation Eq. 4.9 for the occupation of the ground state:

$$- \frac{f_{GS}(1 - f_{ES})}{\tau_{esc}^{GS-ES}} \tag{4.12}$$

where τ_{esc}^{GS-ES} is the escape time to the empty excited state. It can be derived by assuming that the system reaches a quasi-Fermi equilibrium in the absence of external excitations and takes the following form [31]:

$$\tau_{esc}^{GS-ES} = \frac{1}{2R^0} \exp(\frac{E_{ES} - E_{GS}}{k_B T}) \tag{4.13}$$

Due to exponential dependence on the energy difference between the excited and the ground states, the escape time is typically few orders of magnitude larger than the relaxation time. Similarly to the relaxation and capture times, the actual escape time depends on the actual occupation of the respective energy levels. With regard to the occupation of the excited state, there are two limits on the escape time. In the first case the occupation of the excited state is close to saturation, $f_{ES} \sim 1$, so that carriers in the ground state cannot escape to the excited state and as a result the escape term can be neglected. We investigate optically injected QD laser operating under such conditions in Chap. 5. The other possibility is when the excited state is far from saturation, i.e. $f_{ES} \sim 0$ so that the escape term is driven by the actual occupation of the ground state. Since the escape time is typically few orders of magnitude larger than the relaxation time, it can be regarded as a small correction to the relaxation time and included in the model already in the relaxation term by effective relaxation time. In our model we, therefore, do not account explicitly for the escape terms. We would also like to stress, that the original model used to study optically injected QD laser shows good qualitative agreement with the experiment without accounting for thermal escapes [95].

To facilitate numerical calculations, we rewrite Eq. (4.6-4.9) in a dimensionless form using normalized field $F = E\sqrt{\frac{v_g \sigma}{\gamma_q}}$, normalized gain $a = \frac{1}{2}\frac{v_g g_0}{\gamma_q}$, normalized photon decay rate $\gamma = \frac{\gamma_s}{v_g g_0}$, normalized pump current $J = \frac{J_{QD}}{q\gamma_q}$, normalized capture rate to the empty ES $C^0 = \frac{1}{\tau_c \gamma_q}$, normalized relaxation rate to the empty GS $R^0 = \frac{1}{\tau_o \gamma_q}$, $B = \gamma_s \sqrt{\frac{v_g \sigma}{\hbar\omega\gamma_q^3}}$, and $t_1 = t\gamma_q$ as a normalized time. The resulting equations are as follows:

$$\frac{\mathrm{d}F}{\mathrm{d}t_1} = a(2f_{GS} - 1 - \gamma)(1 + i\alpha)F + i\frac{\Delta}{\gamma_q}F + B\sqrt{S_m} + F_{noise} \tag{4.14}$$

$$\frac{\mathrm{d}f_{WL}}{\mathrm{d}t_1} = J - f_{WL} - C^0 f_{WL}(1 - f_{ES}) \tag{4.15}$$

$$\frac{\mathrm{d}f_{ES}}{\mathrm{d}t_1} = -f_{ES} + \frac{C^0 f_{WL}(1 - f_{ES})}{4} - R^0 f_{ES}(1 - f_{GS}) \tag{4.16}$$

$$\frac{\mathrm{d}f_{GS}}{\mathrm{d}t_1} = -f_{GS} + 2R^0 f_{ES}(1 - f_{GS}) - (2f_{GS} - 1)|F|^2 \tag{4.17}$$

In our calculations the normalized pump current is fixed at $J = 6.25$.

To summary, we want to check the impact of the relaxation and the capture times on the dynamics of optically injected QD laser. To this aim we extend the model presented in [95] to account for the excited states and map the bifurcations of the system dynamics in the plane detuning vs. injection strength. We will put special attention to dynamics resulting in pulsed output, i.e. excitability and self-pulsations, which, if fast enough and well controlled, can become an all-optical source of modulated signal. In particular we want to identify the role of the excited states in the emission of self-pulsations. Next, we will study their dynamics in the presence of spontaneous emission noise so that we can compare it with the dynamics experimentally reported for excitable pulses [160]. Specifically, we want to check how the interpose time distribution changes as a function of the detuning and the noise strength. Finally, we would like to utilize such self-pulsations for all-optical signal regeneration. To this aim we will investigate the performance of a system in which an attenuated/distorted information signal acts as a master laser and switches a slave QD laser between the regions of locking and self-pulsations.

4.4 Influence of the relaxation and capture times on the dynamics of optically injected QD lasers.

We first investigate the influence of the two main time constants that determine the QD laser dynamics, namely the capture and relaxation times. To this aim we use the continuation and bifurcation software AUTO-07P [177]. The results for the relaxation rate are presented in Fig. 4.10. All three 2-parameter bifurcation diagrams contain a saddle-node SN bifurcation curve, a Hopf HB bifurcation curve, a homoclinic HOM bifurcation curve, a period doubling PD bifurcation curve and the curve corresponding to a saddle-node bifurcation of limit cycles LPC. The locking region is bordered by parts of the SN and HB curves for a negative detuning, and a branch of the SN curve that verges with the region of a limit cycle LC for a positive detuning.

Comparing the bifurcation diagrams in Fig. 4.10 one can conclude that the relaxation rate strongly influences the size of regions of solutions emerging from the respective bifurcations. When the transitions from the ES to the GS are fast enough our model recovers the results presented in [95]. A lower relaxation rate broadens the locking region and shifts the position of point G_1, where the SN and HB curves are tangent, to a lower injection strength. It is demonstrated in the next section that the laser behavior outside the locking region is different on both sides of point G_1. We have checked that the capture time does not influence the dynamics of the system in the investigated range, that is, 1-10 ps. In Fig. 4.10 the homoclinic bifurcation curve overlaps with parts of the SN curve that border the locking region. However, at certain values of the injection strength, the homoclinic bifurcation curve leaves the

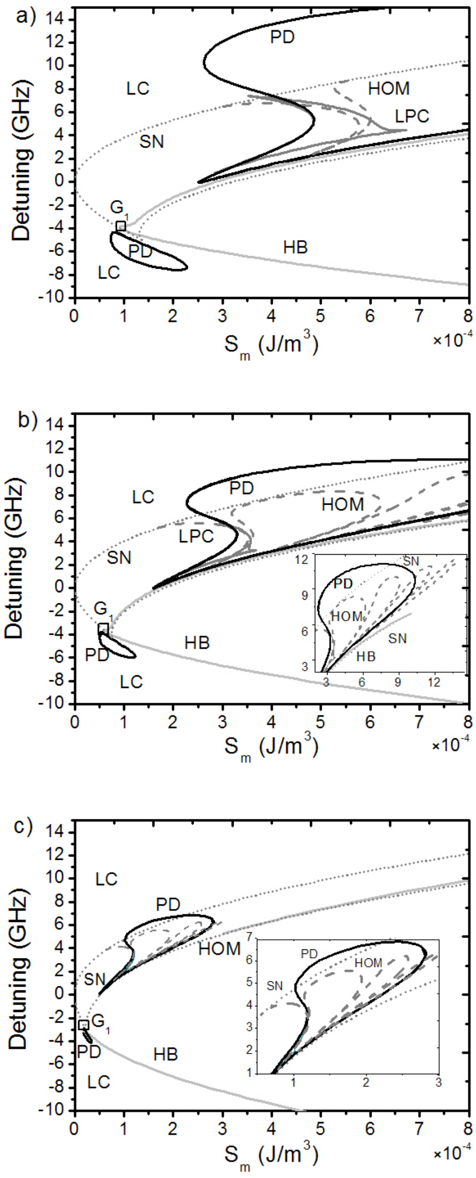

Figure 4.10: 2-parameter bifurcation diagram of equilibria and limit cycles when the normalized relaxation rate R^0 is equal to a) 1020, b) 500, c) 200. The normalized current amounts to J=6.25. Solid, light gray curve HB - Hopf bifurcation, dotted gray curve SN - saddle-node bifurcation, solid black curve PD - period doubling bifurcation, solid, dashed gray curve HOM - homoclinic curve, solid gray curve LPC - saddle-node bifurcation of limit cycles, LC - limit cycle, G_1 - saddle-node-Hopf bifurcation point.

SN curve and forms the so-called homoclinic tooth (HOM), which penetrates into the locking region. It has been shown for optically injected QW lasers [178, 179, 180], that the homoclinic bifurcation constitutes a boundary between two different dynamics resulting in a pulsed output, namely excitability and self-pulsation. In other words, close to the homoclinic bifurcation curve, before the onset of self-pulsations, the laser is excitable, that is, sufficiently strong perturbation, e.g. noise, can force the system to fire pulses. It has already been discussed in Sec. 4.2 that there are two mechanisms leading to excitability, i.e. saddle-node on limit cycle and saddle-node homoclinic orbit bifurcations. In close proximity to the homoclinic tooth excitability is associated with the latter one [179]. As demonstrated in [95], close to the homoclinic tooth, optically injected QD laser can fire single or double excitable pulses, the latter being related to a nearby period doubling bifurcation. Examples of such pulses are shown in Fig. 4.11a,b. We triggered the system by suddenly changing its variables (the duration of such perturbation is 0.1 ns) so that the laser is kicked out from the attractor corresponding to a locked state and makes a quick excursion along the unstable manifold of the saddle [181] back to the attractor. Both fixed points emerge from a nearby saddle-node bifurcation. Inside the homoclinic tooth the laser either can be locked or can exhibit self-pulsations associated with the attracting limit cycle. Unperturbed laser remains in the locked state and, therefore, to observe self-pulsations inside the homoclinic tooth the system needs to be kicked out of the attractor corresponding to the locked state to the vicinity of attraction of the limit cycle. Such bistable behavior is presented in Fig. 4.11c.

As shown in Fig. 4.10b,c, at lower relaxation rates additional teeth arise and mostly fill the region bordered by the period doubling bifurcation curve. Contrary to the main homoclinic tooth however, the consecutive homoclinic teeth are not tangent to the SN curve. The regions of respective solutions shrink so that the laser dynamics are greatly reduced to locking and periodic oscillations in the unlocked region. This is consistent with recent experimental findings [182].

The slave laser is also excitable away from the homoclinic tooth, in close proximity to parts of the SN that overlap with the homoclinic bifurcation curve. Excitability there is related to the saddle-node on limit cycle bifurcation [179]. As such parts exist for both positive and negative detuning, the laser can exhibit this type of excitability on both sides of the locking region. This has been shown experimentally in [160]. Since the homoclinic bifurcation constitutes a boundary between excitability and self-pulsations one can expect that outside the locking region, close to the SN curve, the slave laser will exhibit self-pulsations. We investigate this issue in Sec. 4.5.

4.5 Self-pulsations due to the bottleneck phenomenon.

So far we have analyzed 2-parameter bifurcation diagrams computed with AUTO. This software allows us to continue steady and time-periodic solu-

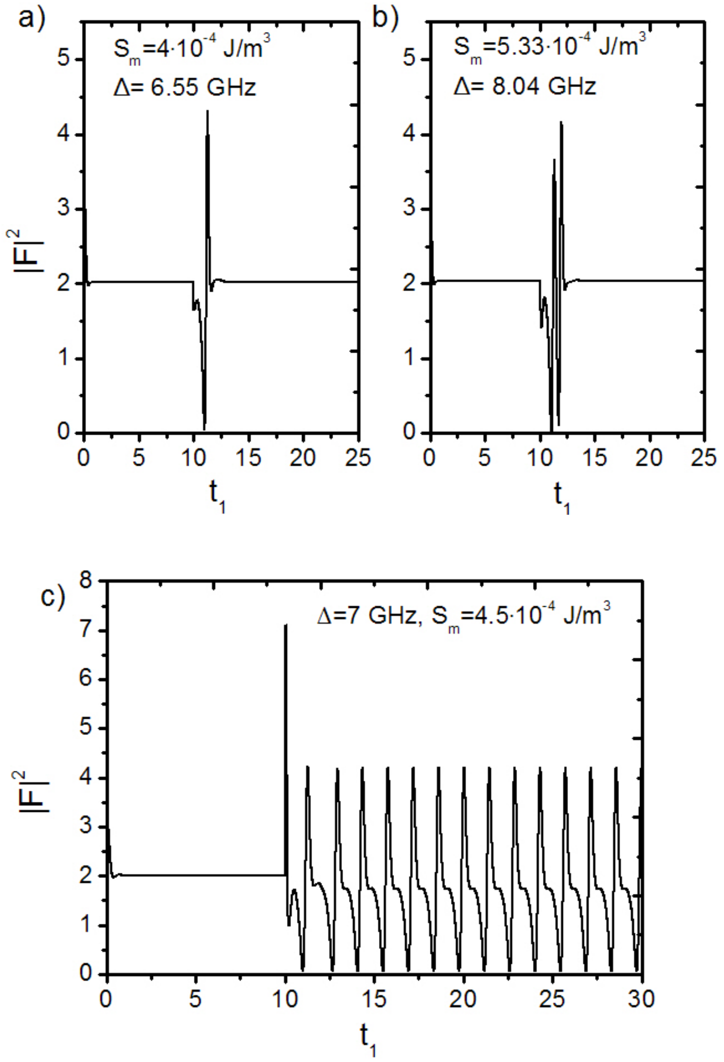

Figure 4.11: Example of triggered a) single-pulse excitability ($\Delta = 6.55$ GHz, $S_m = 4 \times 10^{-4}$ J/m^3) b) double-pulse excitability ($\Delta = 8.04$ GHz, $S_m = 5.33 \times 10^{-4}$ J/m^3). c) Bistability between the attractor corresponding to the locked state and the attracting limit cycle associated with the self-pulsations inside the homoclinic tooth. $S_m = 4.5 \times 10^{-4}$ J/m^3, $\Delta = 7.0$ GHz.

tions of a dynamical system, and detect their stability changes and, therefore, bifurcations. An alternative approach for detecting bifurcations is to analyze intensity time-traces obtained from direct numerical integration for different values of a bifurcation parameter. Therefore, to calculate the complete bifurcation diagrams, such as those presented in Fig. 4.10, one needs to run many computations starting at different points in the (Δ, S_m) plane. We use this method to analyze the behavior of the slave laser outside the locking region but in close proximity to branches of the SN curve that border the locking region. We will refer to such diagrams as extrema maps. The resulting map is presented in Fig. 4.12 (the parameters are consistent with those used to

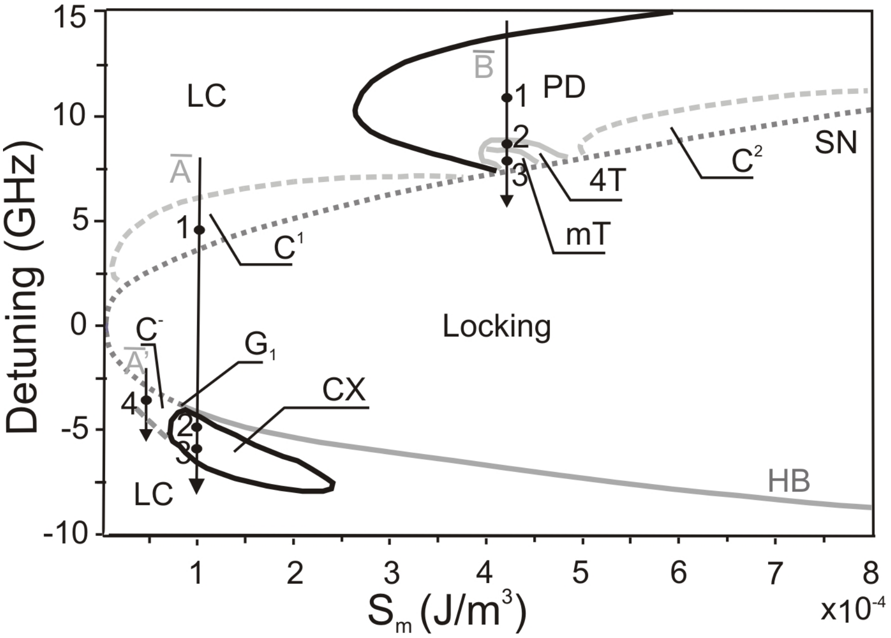

Figure 4.12: Extrema map for optically injected QD laser obtained by analyzing the time traces of $|F|^2$ for the relaxation rate of $R = 1020$. Inside LC the laser exhibits period-one time-periodic oscillations associated with the limit cycle, inside PD - period-two time-periodic oscillations, $C^{1,-}$ correspond to single-pulse self-pulsations for positive and negative detuning, respectively, C^2 corresponds to double-pulse self-pulsations, $4T$ corresponds to period-four time periodic oscillations, mT corresponds to chaotic oscillations. Region CX corresponds to a set of injection parameters bordered by the period doubling bifurcation curve PD in Fig. 4.10a. Inside this region the slave laser exhibits quite diversified dynamics including period-one and period-two time-periodic, and chaotic oscillations. SN - dotted gray line - saddle-node bifurcation, HB - solid light gray curve - Hopf bifurcation, G_1 - saddle-node-Hopf bifurcation point.

calculate the 2-parameter bifurcation diagram presented in Fig. 4.10a). It should be stressed here, that this extrema map accounts only for stable solutions. Similarly to Fig. 4.10a, we can distinguish regions of time periodic solutions (LC), double-period solutions (PD) and locking. The new information brought by Fig. 4.12 is the presence of regions C^-, C^1, C^2, $4T$, mT and CX. The first three regions correspond to deterministic single-pulse (C^-, C^1) and double-pulse (C^2) self-pulsations. They are not associated with a new bifurcation but with a change of the waveform and to highlight the difference they are bordered by gray, dashed curves in Fig. 4.12. Regions $4T$ and mT correspond to period-four time-periodic and chaotic oscillations, respectively. Region CX corresponds to a set of injection parameters bordered by the period doubling bifurcation curve PD in Fig. 4.10a. As shown later, inside this region the slave laser exhibits quite diversified dynamics including period-one and period-two time-periodic, and chaotic oscillations. To characterize all the new regions we compute 1-parameter bifurcation diagrams showing different extrema (both maxima and minima) in the time traces of $|F|^2$ as a function of the detuning. A bifurcation diagram crossing the regions C^1, CX and C^- along the arrow $\bar{A}$ and the corresponding time traces are presented in Fig. 4.13 and Fig. 4.14, respectively. The top plot in Fig. 4.13 corresponds to sweeping of the detuning from negative toward positive values, whereas the bottom plot corresponds to the opposite direction of sweeping.

We first describe the bifurcation diagram for positive detuning. As can be concluded from a comparison between the top and bottom plots in Fig. 4.13, the system dynamics are indifferent to the sweeping direction. At a large value of the detuning the laser exhibits period-one time-periodic oscillation LC. When the detuning decreases, in region C^1 the waveform of these periodic oscillations changes (see the time trace in Fig. 4.14-1 corresponding to the gray dot no. 1 on the top plot of Fig. 4.13) so that it resembles single excitable pulses in Fig. 4.11a. Inside C^1 the algorithm used to analyze time-traces of $|F|^2$ detects two additional local extrema between those corresponding to an unbroken limit cycle associated with periodic oscillations in LC (both plots in Fig. 4.13). These additional extrema correspond to strongly damped, low-amplitude oscillations that follow the main spike (see Fig. 4.14-1). Below C^1, close to the SN curve, the slave laser can fire excitable pulses related to the saddle-node on limit cycle bifurcation. We, therefore, classify solutions in C^1 as deterministic single-pulse self-pulsations.

For negative detuning the 1-parameter bifurcation diagram reveals a strong dependence on the sweeping direction. In addition, Fig. 4.12 shows that the behavior of the slave laser for negative detuning should vary on different sides of the point G_1. On its high-injection-strength side the locking region is bordered by the Hopf bifurcation curve. In the top plot of Fig. 4.13, when the HB curve is approached from a large, negative value of the detuning, the laser first exhibits period-one time-periodic oscillations LC and then enters the region CX. To describe its behavior inside CX, we divided this region into

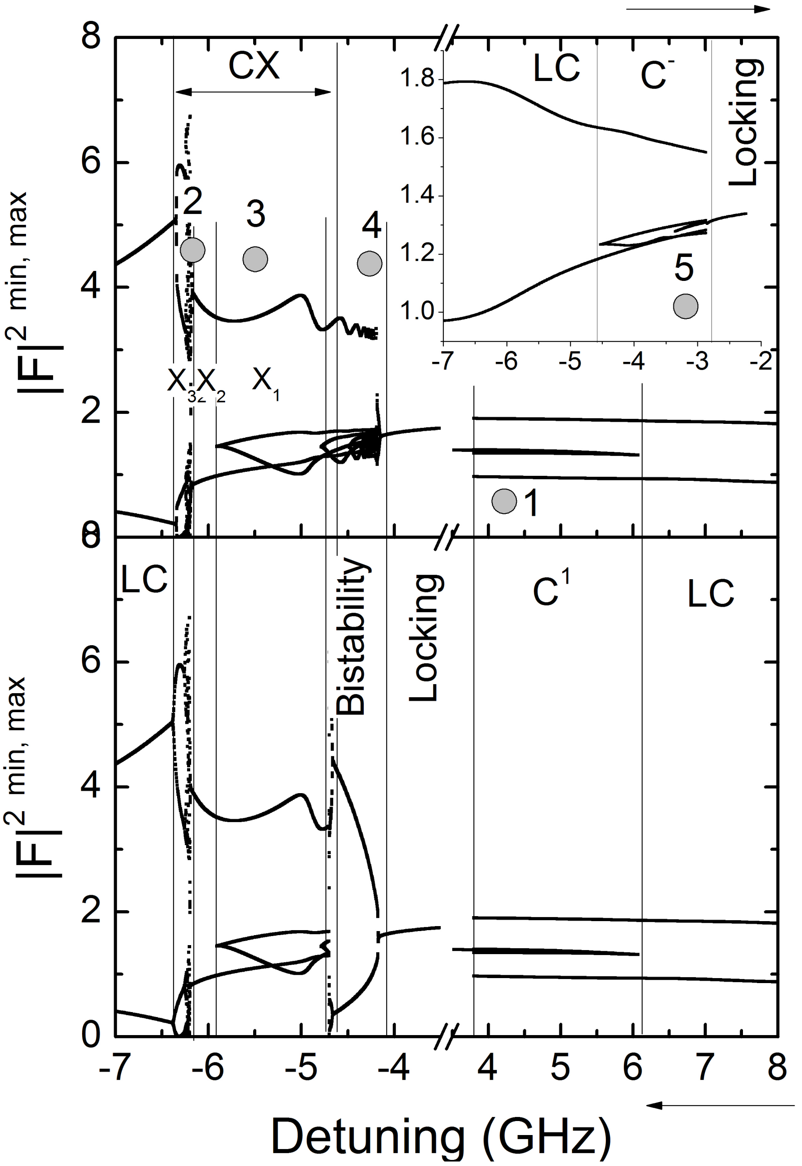

Figure 4.13: 1-parameter bifurcation diagrams for $S_m = 10^{-4}$ J/m^3 (the inset shows bifurcation diagram for $S_m = 0.5 \times 10^{-4}$ J/m^3) when sweeping the detuning either from negative to positive (top plot) or from positive to negative (bottom plot) values.

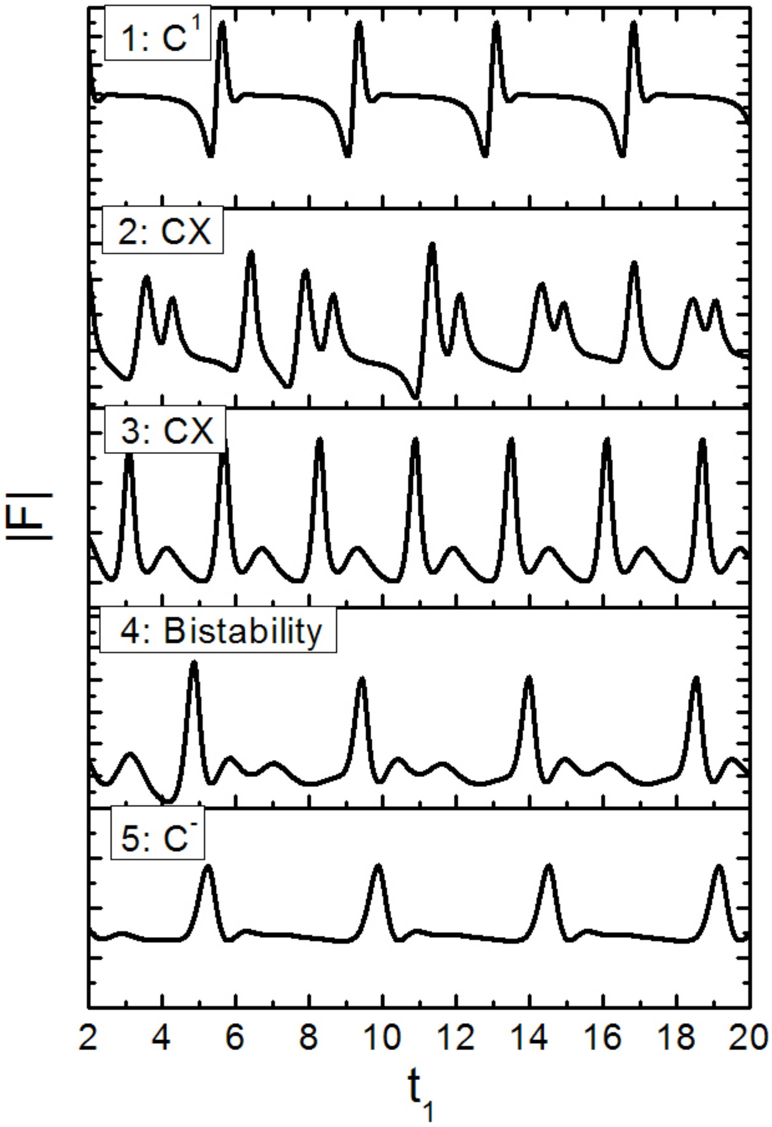

Figure 4.14: Examples of time traces along the arrows A and A' in Fig. 4.12. 1: $\Delta = 4.2$ GHz, 2: $\Delta = -6.177$ GHz, 3: $\Delta = -5.5$ GHz, 4: $\Delta = -4.5$ GHz, 5: $\Delta = -3.2$ GHz.

subregions $X_1 - X_3$. Inside X_3 the waveform of periodic oscillations from LC undergoes period-doubling cascade to chaos (see Fig. 4.14-2 for the chaotic time trace corresponding to the gray dot no. 2 in the top plot in Fig. 4.13). Consecutively, in the narrow range of the detuning corresponding to X_2, the laser again exhibits period-one time-periodic oscillations and then, in the subregion X_1, period-two time-periodic oscillations as in Fig. 4.14-3 corresponding to the gray dot no. 3 in the top plot in Fig. 4.13. At still smaller detuning, close to the boundary of CX, there is a region of bistability (see Fig. 4.13). In this region, when sweeping the detuning from negative toward positive values, the system fires pulses followed by damped, low-amplitude oscillations, as in Fig. 4.14-4 corresponding to the gray dot no. 4 in Fig. 4.13. This shows that the dynamics of the system is influenced by the saddle-node bifurcation. Indeed, as shown in Fig. 4.10a, the SN curve first crosses the HB curve at point G_1 and then it enters the unlocked region. The region of bistability, therefore, extends to the injection strength reached by the SN curve in the unlocked region. The alternative solution in the region of bistability corresponds to period-one time-periodic oscillations (not shown). Such behavior is possible when the detuning changes from positive toward negative values.

On the low-injection-strength side of point G_1, the locking region is bordered by the saddle-node bifurcation. A 1-parameter bifurcation diagram along the arrow $\bar{A}'$ in Fig. 4.12 is shown in the inset in the top plot in Fig. 4.13. Inside C^- the laser fires pulses as demonstrated in Fig. 4.14-5 corresponding to the gray dot no. 5 in Fig. 4.13. We consider these pulses as deterministic self-pulsations for negative detuning.

A 1-parameter bifurcation diagram along the arrow $\bar{B}$ in Fig. 4.12 is presented in Fig. 4.15. The limit cycle first undergoes period doubling bifurcation PD (see also the time trace in Fig. 4.16-1) and then enters regions $4T$ and mT of period-four time-periodic and chaotic oscillations, respectively (see the time traces in Fig. 4.16-2,3).

In a region C^2 the laser exhibits double-pulse self-pulsations (see also the time trace for the amplitude of the electric field in Fig. 4.18) resembling the double-pulse excitability in Fig. 4.11b.

We would like to stress that the self-pulsations in regions $C^{1,2,-}$ are observed deterministically, without the need for an additional perturbation, unlike the self-pulsations that appear inside the homoclinic tooth (and shown in Fig. 4.11c). These self-pulsations result from the so-called bottleneck [161]. In this mechanism, after the saddle-node bifurcation a saddle remnant (or "ghost") can continue influencing the system, although the two fixed points involved in the bifurcation annihilate. In Fig. 4.17a we show the phase diagrams corresponding to the regions below C^1 and inside of C^1 (coordinates of the fixed points have been calculated by DsTool [183]). Indeed, inside C^1 the shape of the attractor is influenced by the "ghost" of a saddle. Moreover, as shown in Fig. 4.17b, the time difference between consecutive pulses in region C^1 follows an inverse square root law as a function of the detuning, which is

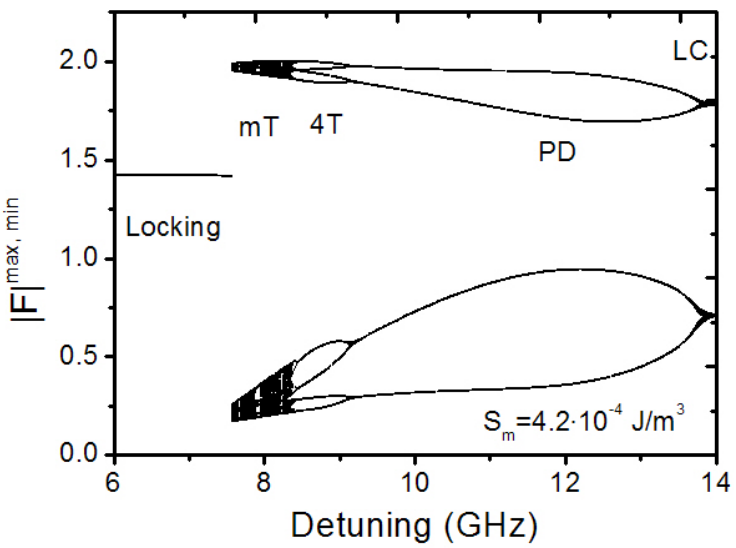

Figure 4.15: 1-parameter bifurcation diagram for $S_m = 4.2 \times 10^{-4}$ J/m^3.

also characteristic of the bottleneck phenomenon [184]. In the deterministic system (the noise term in Eq. 4.6 is neglected) the pulses are periodic regardless of the detuning. The repetition rate on the edge between C^1 and LC is of 0.5 GHz. The same behavior can be observed in regions C^- and C^2. Interestingly, the increase of the repetition rate when the detuning is increased is consistent with experimental observations for excitable pulses [160].

An important question here is how the QD ES contributes to the emission of the self-pulsations. Temporal changes of the occupation of the respective energy levels for a laser exhibiting double-pulse self-pulsations C^2 are shown in Fig. 4.18. With the parameter setting used in the model the GS, which is represented by the dot-dashed curve, is saturated. The ES, represented by the dotted line, is far from saturation and it seems that the shape of the emitted signal is determined mainly by moderate changes in the occupation of this state.

4.6 Effect of spontaneous emission noise on the dynamics of self-pulsations

Excitable pulses can be fired only if the system is subject to a sufficiently strong perturbation, e.g. noise, so that the excitability threshold can be overcome. As characterized in Sec. 4.5, self-pulsations resemble the excitable pulses in Fig. 4.11a,b but can exist even in the absence of noise. In experiments

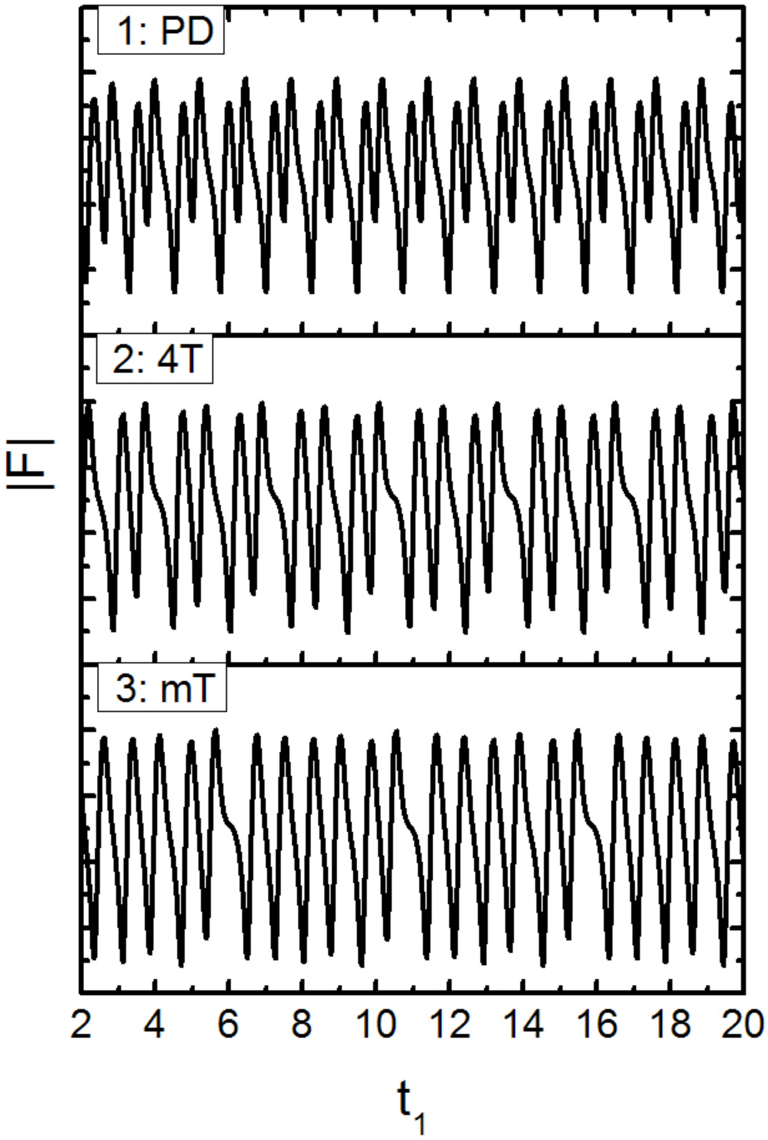

Figure 4.16: Examples of time traces along the arrows B in Fig. 4.12. 1: $\Delta = 11.0$ GHz, 2: $\Delta = 8.8$ GHz, 3: $\Delta = 8.0$ GHz.

noise is inherent to the lasing emission and it is therefore difficult to distinguish between excitability and self-pulsation by looking only at the intensity waveforms. To make our analysis complete, in this section we show that the self-pulsations, when accounting for spontaneous emission noise in the model,

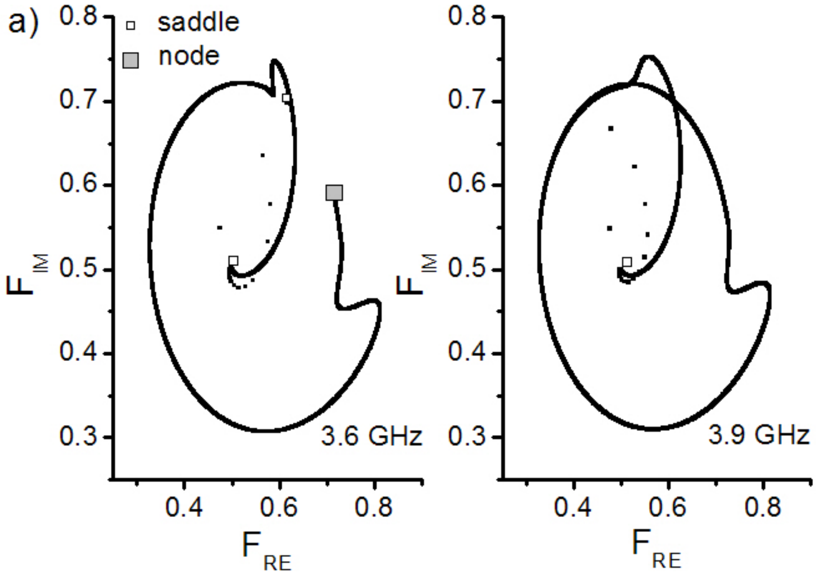

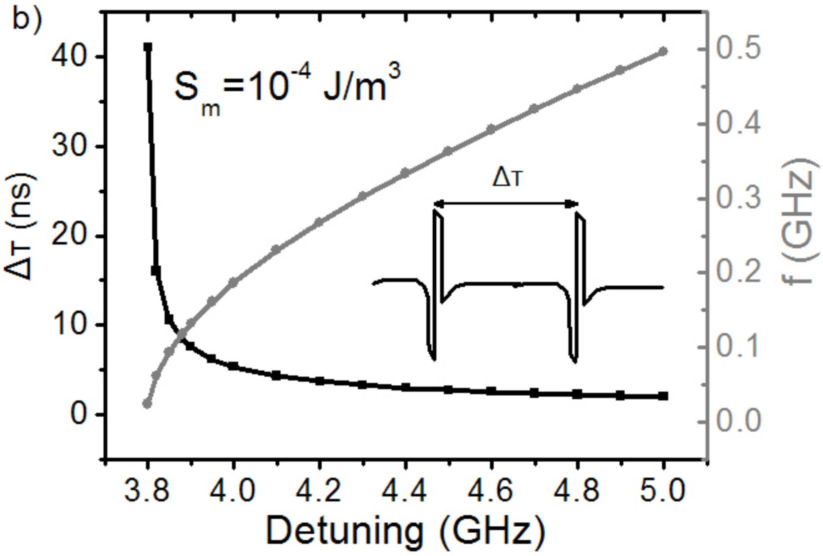

Figure 4.17: a) Phase diagrams for $S_m = 10^{-4}$ J/m^3 and $\Delta = 3.6$ GHz (left), $\Delta = 3.9$ GHz (right). b) Time difference (and corresponding frequency, f) between consecutive pulses in the region C^1 as a function of the detuning.

have statistical characteristics similar to those observed experimentally for the excitable pulses [160]. Time traces for different values of the detuning in the presence of the spontaneous emission noise are shown in Fig. 4.19. Compared

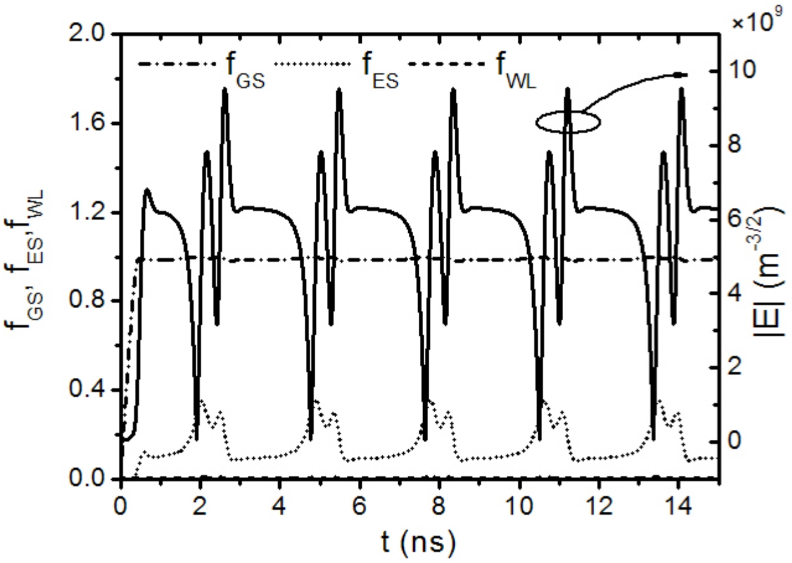

Figure 4.18: Temporal changes of the occupation probabilities of the respective energy levels when the slave laser exhibits double-pulse self-pulsations ($\Delta = 9.4$ GHz, $S_m = 6 \times 10^{-4}$ J/m^3)

to the case without noise, the time between consecutive pulses for a fixed value of the detuning is no longer constant. Nevertheless, the repetition rate still increases with the detuning. Interpose time distributions for two values of the detuning corresponding to the edge between locking and C^1, and between C^1 and LC are presented in the inset in Fig. 4.19. In the former case (black distribution) the interpose time follows a positively skewed normal distribution. In the latter case (grey distribution) the distribution is sharp, while its mean is shifted toward smaller values. This behavior is consistent with that reported in [160] in the regions considered to be excitable.

The interpose time distribution for double-pulse self-pulsations is shown in Fig. 4.20. Two, well-resolved peaks correspond to the time between consecutive double-pulse self-pulsations and to the time between spikes within a single double-pulse self-pulsation. Analyzing the number of peaks of such a distribution has been proposed as a way to detect and distinguish between different types of multipulse excitabilities in an experiment [181]. It can be concluded from the inset in Fig. 4.20 that the noise can break the regularity of self-pulsations as, for example, in the time slot between 492 and 495 ns, where a double pulse is lost at the expense of more periodic oscillations.

In Fig. 4.21 the influence of spontaneous emission noise on the standard deviation σ (Fig. 4.21a) and the mean $< T >$ (Fig. 4.21b) of the interpose time

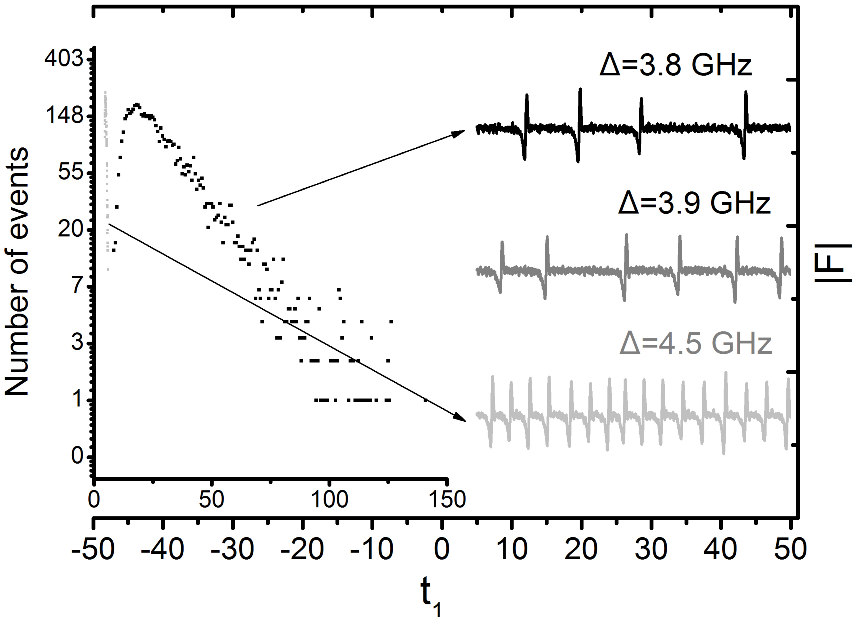

Figure 4.19: Time traces for different values of the detuning in the presence of spontaneous emission noise, $S_m = 10^{-4}$ J/m^3. The inset: semi-logarithmic plot for the distribution of the interpose time for the detuning of 3.8 GHz (black distribution) and 4.5 GHz (gray distribution).

distribution for different values of the detuning is presented. For a detuning of 3.8 GHz, which is at the saddle-node bifurcation curve bordering the locking region for positive detuning, the noise influences both σ and $< T >$. Although for a very small noise, when $\beta_{sp} < 10^{-8}$, the pulses are periodic (see also the time trace in Fig. 4.21c-1), this periodicity is rapidly broken at slightly larger value of noise. At $\beta_{sp} = 10^{-7}$, σ achieves its maximum and then decreases with increasing noise. The mean of the distribution decreases monotonously with increasing noise, after, however, a sharp decrease for $\beta_{sp} < 10^{-6}$. Such behavior indicates that close to the locking region the spontaneous emission noise influences the dynamics of self-pulsations in the same way as the detuning does, that is, it shifts the mean toward smaller values and makes the pulsations more and more periodic (Fig. 4.21c-3,4). In contrast, for a detuning of 3.9 GHz the noise seems not to influence the mean. The standard deviation increases for $\beta_{sp} < 10^{-6}$ and then saturates. For $\beta_{sp} = 10^{-4}$ the output signal becomes very noisy so that both the mean and the standard deviation approach zero (see Fig. 4.21c-5). A noise induced resonance of the time between pulses has not been observed when accounting only for the spontaneous emission noise. Whether another external additive noise source (such

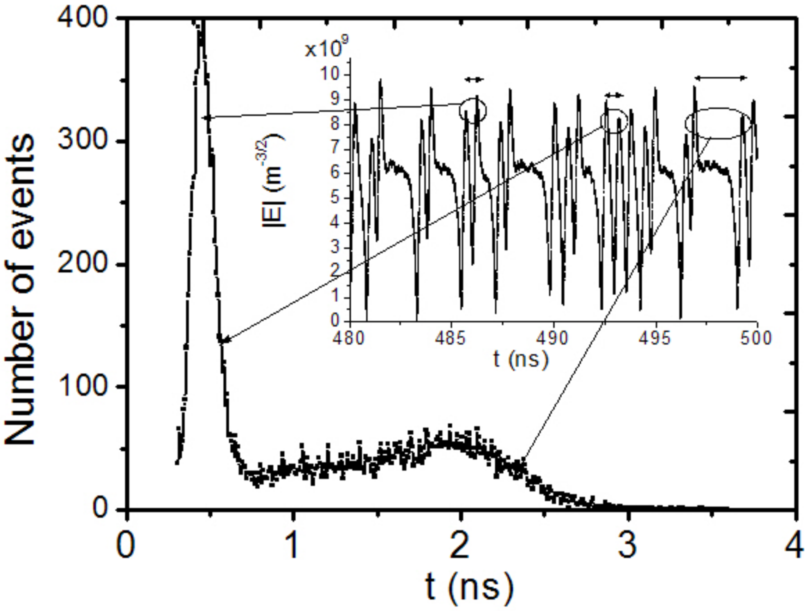

Figure 4.20: Statistics of the interpose time for the double pulse self-pulsations. ($\Delta = 9.6$ GHz, $S_m = \times 10^{-4}$ J/m^3)

as one added to the injection current) can bring the system to a coherence or stochastic resonance behavior [185], [186] is an interesting question for a future work.

4.7 Self-pulsations utilized for all-optical signal processing

The regions of self-pulsations C^1 and C^2 are large enough to be observed experimentally. One can therefore think about utilizing them for all-optical signal reshaping or regeneration. The basic ideal of such a system is schematically shown in Fig. 4.22. Attenuated or/and distorted information signal acts as a master laser. If the system is properly calibrated, the slave laser can be switched by the information signal between the regions of self-pulsation and locking. Among those two regimes, for a fixed value of the detuning, it is the locking that requires higher injection strength (see Fig. 4.12). Consequently, the system produces negative logic output signal, i.e. it fires pulses when the information signal takes logical 0, and is locked when the information signal takes logical 1. In this approach we assume that the frequency of the information signal is constant. The performance of the system is analyzed in

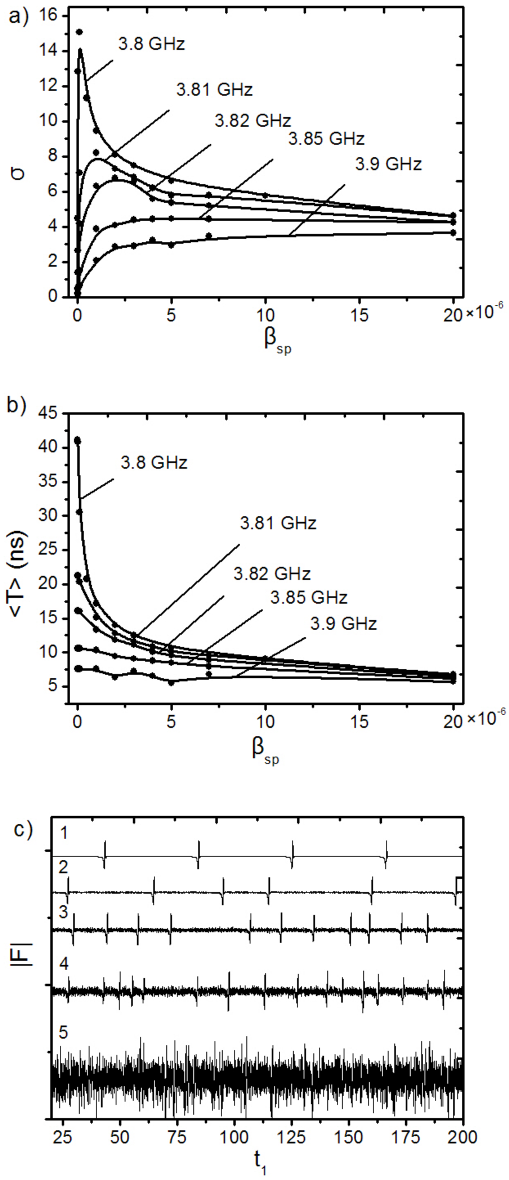

Figure 4.21: a) Standard deviation σ and b) mean $< T >$ of the interpose time distribution as a function of the spontaneous recombination noise strength. $S_m = 10^{-4}$ J/m^3. c) Time traces at the detuning of 3.8 GHz and 1: $\beta_{sp} = 0$, 2: $\beta_{sp} = 10^{-7}$, 3: $\beta_{sp} = 10^{-6}$, 4: $\beta_{sp} = 5\ 10^{-6}$, 5: $\beta_{sp} = 10^{-4}$.

terms of the maximum bit rate and the error factor (defined as a fraction of incorrectly detected bits to the total number of bits). In our simulations the testing sample is random and consists of 1000 bits.

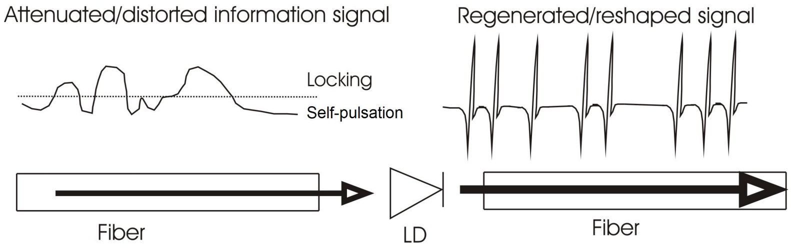

Figure 4.22: The scheme of a system utilizing self-pulsations to all-optical signal processing.

The operation of the system is explained in Fig. 4.23. The information signal is represented by a light gray line. For the sake of simplicity we show only 16 bits. When the information signal is at 0 state the system fires a pulse, e.g. bit number 1. The detection algorithm checks whether in the time slot corresponding to this bit the output signal surpasses some reference level. If so, this bit is classified as logical 1 (the system produces negative logic output signal). The value of the decision level is adjusted in such a way that the results are not affected by the noise. In the time slot corresponding to logical 1 of the information signal the laser is switched to the locking region, e.g. bit number 2. In the time slot corresponding to this bit the detection algorithm expects that the reference level is not crossed, otherwise we will classify this bit as an error, e.g. bit number 6. In Fig. 4.23, four bits have been transmitted incorrectly, which corresponds to an error factor of 0.25.

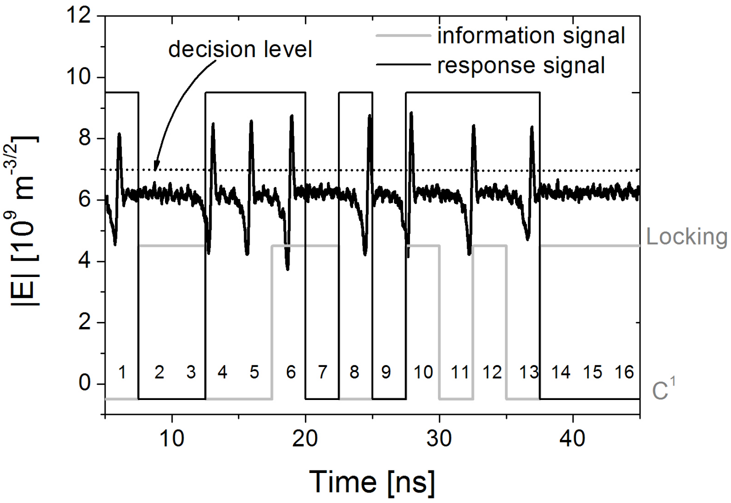

Figure 4.23: Example of the system operation.

As it has been shown in Sec. 4.5, dynamics of self-pulsations depends on the injection parameters. One can therefore expect that these parameters will also determine the overall performance of the proposed system. Fig. 4.24a,b show the error factor as a function of the detuning and of the bit rate, respectively. The results suggest that all these factors are closely related. For a given detuning, the minimum of the error factor is achieved at a bit rate corresponding to the mean of the interpose time distribution in the presence of noise. In other words, when the information signal changes faster than self-pulsations can be fired (at a given detuning) then the error factor increases rapidly. According to Fig. 4.18, the maximum frequency of self-pulsations is around 0.5 GHz and, therefore, this value can be considered as a maximum bandwidth of the system.

The response of the system to the information signal is not immediate, and this delay influences the value of the error factor. For example, in Fig. 4.23 we will classify bits number 9 and 10 as errors. This is because the system is not able to fire two pulses at once in such a short time interval. Specifically, self-pulsations in $C^{1,-,2}$ result from the bottleneck phenomenon, which deforms otherwise sinusoidal waveform of the limit cycle LC. Consequently, during the time the system spends getting through the bottleneck it is inert, i.e. it can not fire pulses. In Fig. 4.23 this is the case within the time corresponding to the bit number 9 where the system is inert after firing a delayed pulse in the previous time slot. Interestingly, it seems that the system remembers the perturbation and fires a pulse in the following interval. We will refer to a delayed response to a perturbation as an activation time.

The situation explained with bits number 9 and 10 suggests that the error factor could be decreased if the detection algorithm would account for the inherent activation time of the pulses. We, therefore, propose a correction method that is based on an a-priori computation of the statistics of the activation time of the system, and in particular on the computation of a mean activation time. The distribution of the activation time is plotted in Fig. 4.25, for the same detuning value as used in Figs. 4.23,4.24b. The mean activation time is then used to delay the reshaped/regenerated signal with respect to the input information signal; see Fig. 4.26. In this particular case the delay amounts to $\Delta T = 1.45$ ns. Above the plotting area of Fig. 4.26 we give logical states of the information (gray) and output (black) signals. All bits have been transmitted correctly, which proves that the correction helps to reduce the error factor. We have checked that due to this correction the bandwidth of the system can be improved to 1 GHz.

4.8 Summary and conclusions

In summary, we have expanded a theoretical model for optically injected QD lasers to account for the excited states and intradot transitions of carriers. The

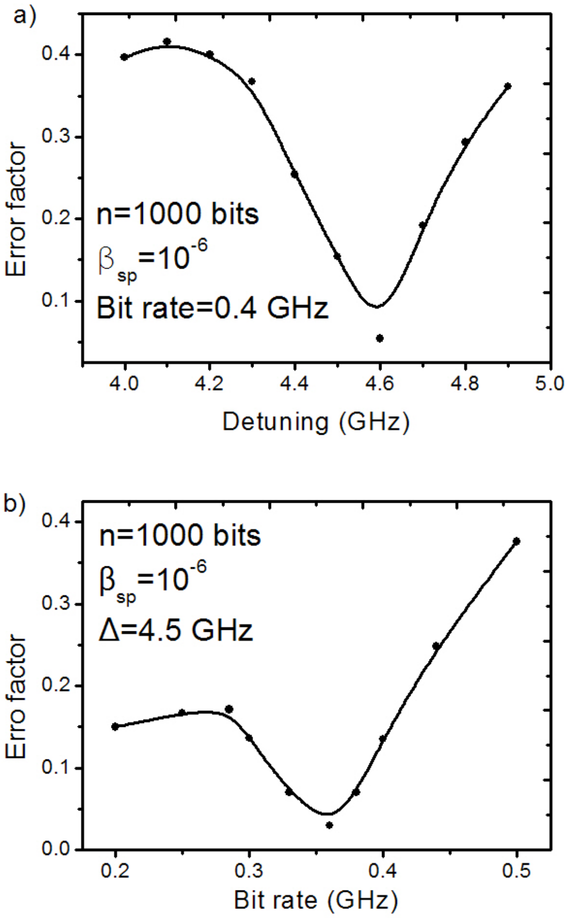

Figure 4.24: The error factor as a function of a) the frequency detuning (for fixed bit rate of the information signal) and b) the bit rate of the information signal (for fixed detuning).

model allows us to check the influence of the main time constants, namely the capture and relaxation times. Our results show that the dynamics of optically injected QD laser are determined mainly by the relaxation time. Among other things it scales the regions of locking and single and double-period solutions. The capture time has a minor impact on the dynamics. Bifurcation maps calculated with continuation and bifurcation software have been compared with the bifurcation map obtained by analysis of the intensity time traces. With the latter method, within the regions of periodic solutions we are able to identify subregions where the laser deterministically fires a time-periodic sequence of single or double pulses resembling excitable ones. We refer to these solutions as deterministic self-pulsations resulting from the bottleneck

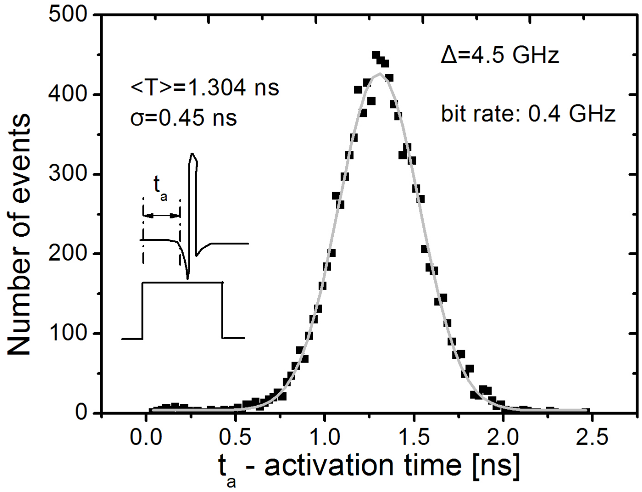

Figure 4.25: Distribution of the activation time.

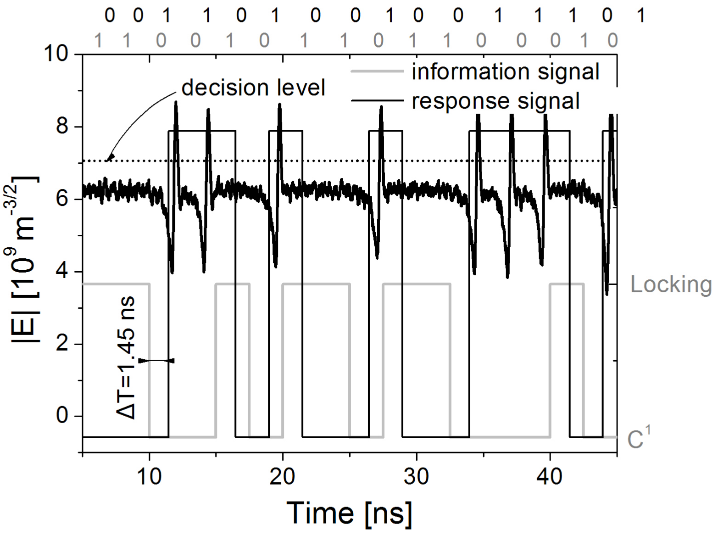

Figure 4.26: Operation of the system with a correction applied to the detection algorithm.

phenomenon [161], [184]. Regions of single-pulse self-pulsations appear for both positive and negative detuning. Our results suggest that such emission is mainly determined by fluctuations in the occupation of the excited states.

To have complete comparison between the dynamics of self-pulsations and excitable pulses we have accounted for the spontaneous emission noise in the model. In both, deterministic and stochastic systems the interpose time changes with the detuning according to an inverse square root scaling low. However, in deterministic system the pulses are periodic regardless of the detuning which is not the case in the presence of noise. In such a case, close to the SN curve the interpose time follows positively skewed normal distribution. The distribution becomes sharp for higher values of the detuning when the unbroken limit cycle is being approached. Described behavior is consistent with the experimental findings for excitable pulses [160].

We also show that in the nearest proximity of the SN curve the noise strength influences the dynamics of self-pulsations in the same way as the detuning does, that is, it shifts the mean toward smaller values and makes the pulsations more and more periodic. In contrast, for larger values of the detuning, in a given range of realistic spontaneous emission noise levels, the mean and the standard deviation saturate so that the dynamics of self-pulsations seem not to be affected by the noise. A noise induced resonance of the time between pulses has not been observed when accounting only for spontaneous emission noise. Whether another external additive noise source (such as one added to the injection current) can bring the system to a coherence or stochastic resonance behavior is an interesting question for a future work.

Finally, we have studied the performance of an optically injected QD laser used for all-optical signal reshaping or regeneration. In our approach, the information signal acts as a master laser and switches the slave QD laser between the regions of locking and self-pulsations. The maximum bit rate of such a system is determined by the mean of the interpose time distribution for a given noise strength. In the deterministic system it amounts to 0.5 GHz. Since during the time that the system spends getting through the bottleneck it is inert, i.e. it can not fire pulses, the response of the system to the information signal is not immediate, and this delay influences the value of the error factor. We, therefore, propose a correction method that is based on an a-priori computation of the statistics of these delays (activation time), and in particular on the computation of its mean value. This value is then used to delay the reshaped/regenerated signal with respect to the input information signal. Our results show that such correction can improve the maximum bandwidth of the system to 1 GHz.

Chapter 5

Optically injected QD laser lasing simultaneously from the ground and the excited state

5.1 Introduction

Optically injected QW lasers show rich variety of behavior including stable locking, bistability, excitability, period doubling route to chaos etc. [50, 89, 91, 92]. All these dynamics are well understood now and can be modeled by single mode rate equations [50]. There are however, circumstances in which the multitude dynamics has to be taken into account. A good example is polarization dynamics of VESSELS. Even in single-transverse mode devices there exist two orthogonal, linearly polarized components with frequency splitting of a few HZ determined by birefringence. Comprehensive study of bifurcations of dynamics of a two-polarization mode VCSEL subjected to orthogonal optical injection (polarization of injected light is orthogonal to the one of the solitary VCSEL) has been presented in [90, 101, 102]. It unveiled new bifurcations beyond those found in the single-mode model such as Hopf bifurcation on a two-mode solution and transcritical bifurcation between two-mode and single-mode solutions [101].Another example is a QW EEL supporting emission of two longitudinal modes with THz frequency spacing achieved by special cavity design [103]. Optical injection in such a two-color laser revealed the importance of torus bifurcation in the route to two-mode antiphase dynamics with short-pulse packages and optical chaos.

In this chapter we undertake theoretical study of nonlinear dynamics induced by optical injection in another two-mode laser system, namely QD laser. In these devices the finite number of QDs within the active region and the discrete energy structure of QDs can lead to saturation of the ground state

(GS) at moderate currents. In such case the occupation of the excited states (ES) grows with current and the laser can start to lase from these states too. Simultaneous emission from both states has been demonstrated for a solitary QD laser in [31, 104], but has also been studied for a QD laser subjected to optical feedback [105] and for dual-wavelength mode-locking [106].

Injected carriers attain the GS and ES with rates determined by the relaxation and capture times, respectively. These times are expressed by fixed values τ_0 and τ_c corresponding to an empty destination state, i.e. $j = ES$ for capture process and $j = GS$ for relaxation, divided by the Pauli exclusion term $(1 - f_j)$ that makes the relaxation and capture times dependent on the actual occupation of the destination state f_j. We will show in this chapter that oscillations of the GS occupation caused by optical injection lead to modulation of the relaxation time and consecutively to oscillations in the occupation of the ES. Such modulation can lead to emission of picosecond pulses from the ES, which is associated with a gain switching mechanism.

5.2 Theoretical model

To account for the presence of the ES we extend the theoretical model presented in [95] in a similar fashion as in Sec. 4.3. Furthermore, to allow lasing from both states, we add an additional equation for the field of the ES mode. Contrary to the case of multi-mode QW EEL [103], in our QD laser model different modes are associated with separate reservoirs of carriers corresponding to the ES and GS. These reservoirs are coupled through the relaxation process and are filled up in a cascade manner with different rates determined by the relaxation and capture times that depend on the actual occupation of the respective states, see Fig. 4.9b. We assume that due to the large (THz) frequency spacing between the GS and ES the injected light interacts directly only with the GS mode. Nevertheless, the injected light can affect the uninjected ES mode indirectly, by modifying the relaxation time depending on the actual occupation of the GS due to the Pauli blocking term. The complete set of equations reads:

$$\frac{dE_{ES}}{dt} = \frac{1}{2}v_g g_{ES}(2f_{ES} - 1 - \frac{\gamma_s}{v_g g_{ES}})(1 + i\alpha)E_{ES}, \tag{5.1}$$

$$\begin{aligned} \frac{dE_{GS}}{dt} &= \frac{1}{2}v_g g_{GS}(2f_{GS} - 1 - \frac{\gamma_s}{v_g g_{GS}})(1 + i\alpha)E_{GS} \\ &\quad + i\Delta E_{GS} + \gamma_s\sqrt{\frac{S_m}{\hbar\omega}}, \end{aligned} \tag{5.2}$$

$$\frac{df_{WL}}{dt} = \frac{J_{QD}}{q} - \gamma_N f_{WL} - \frac{f_{WL}(1 - f_{ES})}{\tau_c^0}, \tag{5.3}$$

$$\begin{aligned}\frac{df_{ES}}{dt} &= -\gamma_q f_{ES} + \frac{f_{WL}(1-f_{ES})}{4\tau_c^0} - \frac{f_{ES}(1-f_{GS})}{\tau_o^0} \\ &\quad -v_g\sigma(2f_{ES}-1)|E_{ES}|^2, \end{aligned} \tag{5.4}$$

$$\begin{aligned}\frac{df_{GS}}{dt} &= -\gamma_q f_{GS} + \frac{2f_{ES}(1-f_{GS})}{\tau_o^0} \\ &\quad -v_g\sigma(2f_{GS}-1)|E_{GS}|^2. \end{aligned} \tag{5.5}$$

The square of the amplitude of the electric field, i.e. $|E_{GS,ES}|^2$, describes the density of photons and is proportional to the intensity of light emitted by the GS/ES mode [1] $I_{GS,ES}$. Therefore, for the sake of brevity, in the remaining part of this chapter the density of photons is called *intensity.*

The capture time $\tau_c = \frac{\tau_c^0}{1-f_{ES}}$ and relaxation time $\tau_o = \frac{\tau_o^0}{1-f_{GS}}$ are determined by the fixed values τ_c^0 and τ_o^0 corresponding to the empty ES and GS, respectively, and by the actual occupation of the ES and GS. The linear optical gain coefficient is $g_{GS} = 72$ cm^{-1} for the GS and $g_{ES} = 2g_{GS}$ for the ES. Unless otherwise stated, the values of the remaining parameters are consistent with those given in Tab. 4.1 of Sec. 4.3.

To facilitate numerical calculations, we rewrite Eq. (5.1-5.5) in a dimensionless form using normalized field $F_{GS,ES} = E_{GS,ES}\sqrt{\frac{v_g\sigma}{\gamma_n}}$, normalized gain coefficient $a_{GS,ES} = \frac{1}{2}\frac{v_g g_{GS,ES}}{\gamma_n}$, normalized photon decay rate $\gamma_{GS,ES} = \frac{\gamma_s}{v_g g_{GS,ES}}$, normalized pump current $J = \frac{J_{QD}}{q\gamma_n}$, normalized capture rate to the empty ES $C^0 = \frac{1}{\tau_c^0\gamma_n}$, normalized relaxation rate to the empty GS $R^0 = \frac{1}{\tau_o^0\gamma_n}$, normalized detuning $\Delta' = \frac{\Delta}{\gamma_n}$, and $B = \gamma_s\sqrt{\frac{v_g\sigma}{\hbar\omega\gamma_n^3}}$. Time is normalized to the carrier decay rate γ_n, i.e. $t' = t\gamma_n$. Since the phase of the (uninjected) ES mode decouples from the rest of equations, Eq. (5.1) for the complex-valued amplitude, E_{ES}, can be replaced by an equation for the real-valued intensity, I_{ES}. The final set of equations reads:

$$\frac{dI_{ES}}{dt'} = 2a_{ES}(2f_{ES}-1-\gamma_{ES})I_{ES} \tag{5.7}$$

$$\begin{aligned}\frac{dF_{GS}}{dt'} &= a_{GS}(2f_{GS}-1-\gamma_{GS})(1+i\alpha)F_{GS} \\ &\quad +i\Delta' F_{GS} + B\sqrt{S_m} \end{aligned} \tag{5.8}$$

---

[1] From definition, the intensity of light is related to the density of photons $|E|^2$ by:

$$I = \frac{v_g\alpha_m h\nu V_{cav}}{A}|E|^2, \tag{5.6}$$

where v_g is group velocity, α_m accounts for mirror losses, $h\nu$ is the energy of the emitted photons, V_{cav} is the cavity volume, A represents the beam cross section area.

$$\frac{df_{WL}}{dt'} = J - f_{WL} - C^0 f_{WL}(1 - f_{ES}) \tag{5.9}$$

$$\begin{aligned}\frac{df_{ES}}{dt'} &= -f_{ES} + 0.25C^0 f_{WL}(1 - f_{ES}) - R^0 f_{ES}(1 - f_{GS}) \\ &\quad -(2f_{ES} - 1)I_{ES}\end{aligned} \tag{5.10}$$

$$\frac{df_{GS}}{dt'} = -f_{GS} + 2R^0 f_{ES}(1 - f_{GS}) - (2f_{GS} - 1)|F_{GS}|^2 \tag{5.11}$$

5.3 Analytical expressions for the steady state occupations of the ground and excited states and the mode intensities in a free-running QD laser

We present here a steady-state solutions of Eq. (5.7-5.11) for a solitary QD laser, i.e. the time-derivatives and the last two terms in Eq. 5.8 are set to zero.

5.3.1 Ground state emission

At the threshold for the GS mode emission, the GS gain balances the losses:

$$f_{GS} = \frac{\gamma_{GS} + 1}{2} \tag{5.12}$$

With the time derivatives at the left hand side of Eg. 5.9 put to zero, the steady state occupation of the WL reads:

$$f_{WL} = \frac{J}{1 + C^0(1 - f_{ES})} \tag{5.13}$$

Similarly, putting to zero the time derivatives at the left hand side of Eg. 5.10 and then plugging in Eq. 5.13 for f_{WL} we obtain quadratic equation for the steady state occupation of the ES, i.e.:

$$af_{ES}^2 + bf_{ES} + c = 0 \tag{5.14}$$

where:

$$a = C^0[1 + R^0(1 - \frac{\gamma_{GS} + 1}{2})] \tag{5.15}$$

$$b = -[4(R^0(1 - \frac{\gamma_{GS} + 1}{2}) + 1)(1 + C^0) + C^0 J] \tag{5.16}$$

$$c = C^0 J \tag{5.17}$$

Only one solution, i.e. with $f_{ES} > 0$ is physical.

Knowing the steady-state occupations and putting to zero the time derivatives at the left hand side of Eg. 5.11 it is now possible to calculate the intensity of the GS mode, i.e. $|F_{GS}|^2$:

$$|F_{GS}|^2 = \frac{2R^0 f_{ES}(1 - f_{GS}) - f_{GS}}{\gamma_{GS}} \tag{5.18}$$

The current for which $|F_{GS}|^2$ equals to zero constitutes threshold for the GS mode.

5.3.2 Ground and excited state emission

In this case, both the GS and ES gains balance the corresponding losses, i.e.:

$$f_{GS} = \frac{\gamma_{GS} + 1}{2} \tag{5.19}$$

$$f_{ES} = \frac{\gamma_{ES} + 1}{2} \tag{5.20}$$

With the time derivatives at the left hand side of Eg. 5.9 put to zero, and known steady state occupation of the ES (Eq. 5.20) the steady state occupation of the WL reads:

$$f_{WL} = \frac{J}{1 + C^0(1 - \frac{\gamma_{ES}+1}{2})} \tag{5.21}$$

The intensity of the GS mode is constant, given by Eq. 5.18 together with Eqs. 5.19 and 5.20. The intensity of the ES mode, i.e. $|F_{ES}|^2$ can be calculated by putting to zero the time derivatives at the left hand side of Eg. 5.10:

$$|F_{ES}|^2 = \frac{0.25C^0 f_{WL}(1 - f_{ES}) - f_{ES} - R^0 f_{ES}(1 - f_{GS}))}{\gamma_{GS}} \tag{5.22}$$

As the occupations f_{GS}, f_{ES} and f_{WL} in Eq. 5.22 the steady state values calculated with Eq. (5.19-5.21) should be used.

The current for which $|F_{ES}|^2$ equals to zero constitutes threshold for the ES mode.

Analytical expressions for the steady state occupations of the GS and ES and the mode intensities in a free-running laser, i.e. without optical injection are then used to calculate the mode intensity versus current for different values of the relaxation rate to the empty GS (R^0), see Fig. 5.1. As can be seen from the figure, the ES mode reaches its lasing threshold when the GS mode saturates. The threshold current for the ES mode strongly depends on the value of R^0. When R^0 decreases the ES mode starts to lase at smaller currents, while threshold for the GS mode slightly increases. At

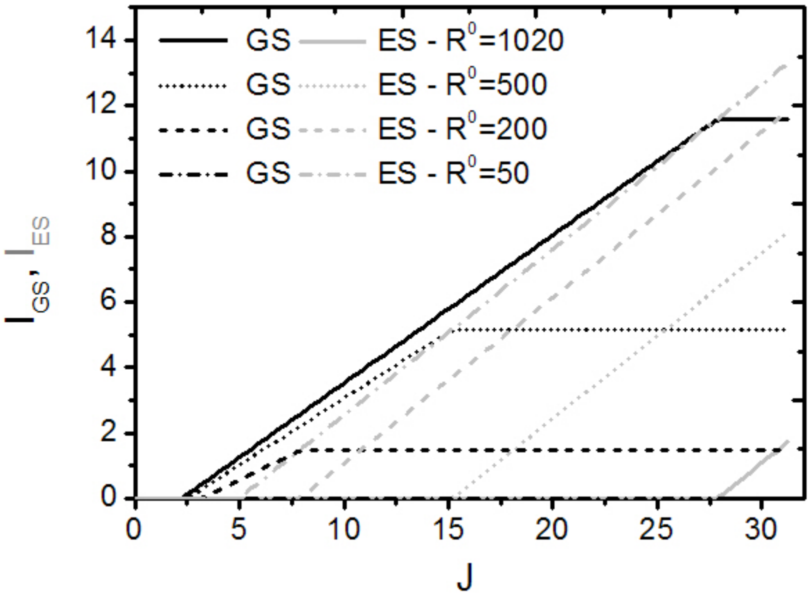

Figure 5.1: Intensities of the GS and ES modes versus current as a function of the relaxation rate to the empty GS, R^0.

extremely slow relaxation, i.e. $R^0 = 50$, the laser emits only the ES mode. For the remaining part of the chapter we fix $R^0 = 500$ giving threshold current for the ES mode of $J_{th}^{ES} = 15$ and $J_{th}^{ES} : J_{th}^{GS} = 6 : 1$. This choice reflects the available experimental values [31, 34].

5.3.3 Intrinsic gain switching in optically injected QD laser lasing simultaneously from the ground and excited states

In this section we fix the current to $J = 17$, that is just above the lasing threshold of the ES mode in a free-running laser, and investigate injection-induced dynamics of the GS and ES modes. To give a rough overview of the dynamics, we present in Fig. 5.2a an extrema map where we use different shades of gray to indicate a number of different extrema in the time series of the ES mode intensity, I_{ES}, for each point in the (Δ, S_m) plane. Specifically, light gray L^1 indicates absence of extrema and $I_{ES} = 0$ (steady state solution with ES mode below threshold), light gray L^2 indicates absence of extrema and $I_{ES} > 0$ (steady state solution with ES mode above threshold), dark gray U^2 indicates two different extrema (period-one periodic orbit), white U^3 indicates three different extrema, gray $U^{>3}$ indicates more than three different extrema

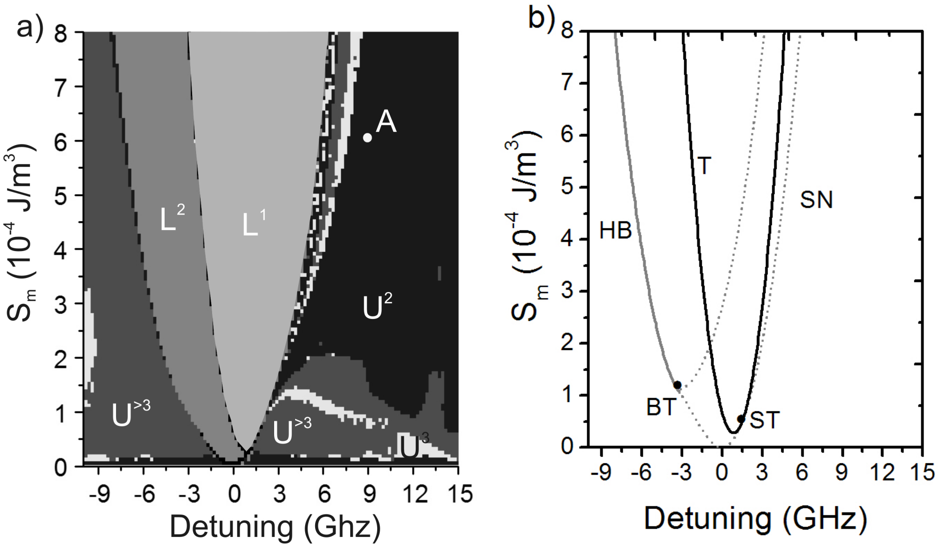

Figure 5.2: a) Extrema map for $J = 17$. Respective shades of gray represent: light gray L^1 - locked GS mode and suppressed ES one(lack of extrema), light gray L^2 - locked GS mode but unsuppressed ES one (lack of extrema), dark gray U^2 - time-periodic pulsations (two extrema), white U^3 - oscillations characterized by three extrema, gray $U^{>3}$ - complex dynamics characterized by more than thee extrema, possibly chaotic. b) 2-parameter bifurcation diagram calculated by AUTO [177]. Solid gray curve HB denotes Hopf bifurcation, dotted gray curve SN - saddle-node bifurcation and solid black curve T - transcritical bifurcation. BT and ST are codimension two points at which the saddle-node-Hopf bifurcation curves and saddle-node and transcritical bifurcation curves, respectively are tangent.

and includes cases of irregular, possibly chaotic oscillations. Interestingly, optical injection into the GS mode can have various effects on the dynamics of the ES mode. Depending on the settings of Δ and S_m, it can inhibit lasing of the ES mode or excite (irregular) selfpulsations in the ES mode intensity.

While the GS mode always remains above the threshold, its intensity dynamics are limited to two types of locking and time-periodic oscillations. In a single-mode injected laser, locking is a single-frequency operation when the laser emits at the frequency of the injected signal. In two-mode lasers however, it is possible to have two frequency operation with locked injected mode and unlocked uninjected one. Such behavior has been observed with two polarization-mode QW VCSELs [101] and with two longitudinal-mode QW EEL [187].

In Fig. 5.2a different types of locking of the GS mode are represented by light gray regions L^1 and L^2. Single-frequency locking (when the ES mode

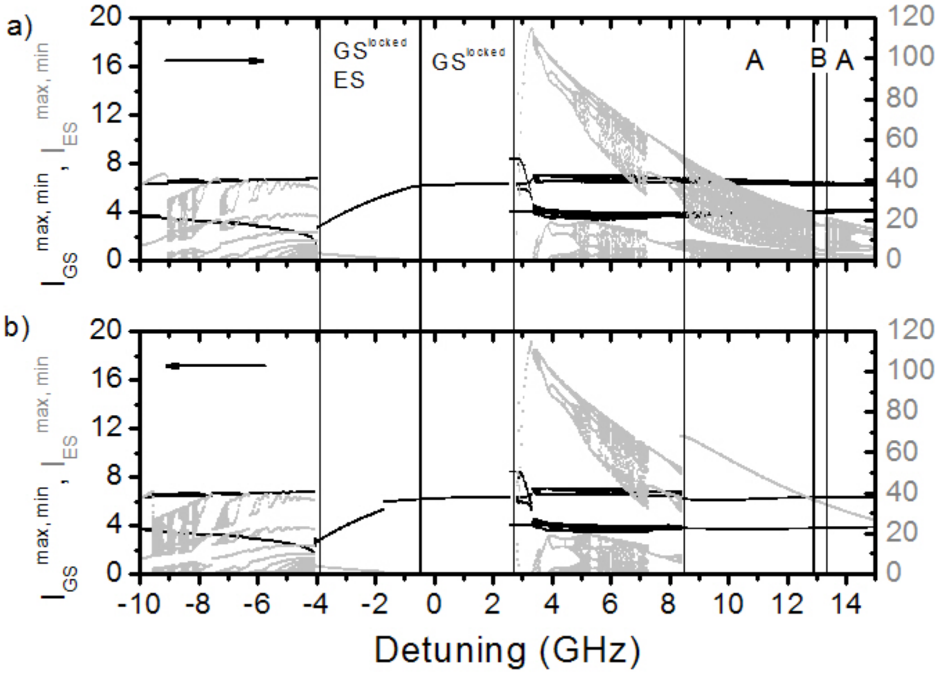

Figure 5.3: 1-parameter bifurcation diagram for $J = 17$, $S_m = 1.5{\times}10^{-4}$ J/m^3 when sweeping the detuning either from a) negative to positive or b) from positive to negative values.

is suppressed) exists inside the region L^1, and two-frequency locking (when the *ES* mode is unsuppressed and unlocked) exists inside the region L^2. We also used numerical continuation [177] to calculate a 2-parameter bifurcation diagram for the same parameter values as in Fig. 5.2a. Bifurcation analysis in Fig. 5.2b reveal that in the (Δ, S_m) plane locking is bounded by Hopf (HB) and saddle-node (SN) bifurcations. Furthermore, the transition between the two different types of locking occurs via transcritical bifurcation (T). This bifurcation defines the lasing threshold of the *ES* mode in the injected laser. For positive detuning Δ, the saddle-node bifurcation takes place on a periodic orbit and is sometimes referred to as saddle-node bifurcation on the invariant circle [161]. As a result, the waveform of period-one oscillations in the *GS* mode intensity found outside the locking region is influenced by a ghost of the saddle-node near to the bifurcation and looks like deterministic self-pulsations described in [188].

The behavior of the *ES* mode in the unlocked region is much more diverse and complicated. First we investigate its dynamics for injection strength smaller than 2×10^{-4} J/m^3. The 1-parameter bifurcation diagram for $S_m = 1.5 \times 10^{-4}$ J/m^3 is shown in Fig. 5.3. Regardless of the detuning, the waveform of the *ES* mode has one extremum at zero-intensity level, meaning that it is pulsed and the respective points in the bifurcation diagram correspond to the amplitudes of the pulses. A comparison between Fig. 5.3a and Fig. 5.3b reveals strong dependence on the sweeping direction of the detuning. Namely, starting from $\Delta = 8.8$ GHz there is bistability between pulsed output of the ES mode with periodic spikes of fixed amplitude and pulsed output of the ES mode that can be highly irregular and involve spikes of different amplitude (as in regions A in Fig. 5.3) or form more regular pulse patterns (as in regions B in Fig. 5.3).

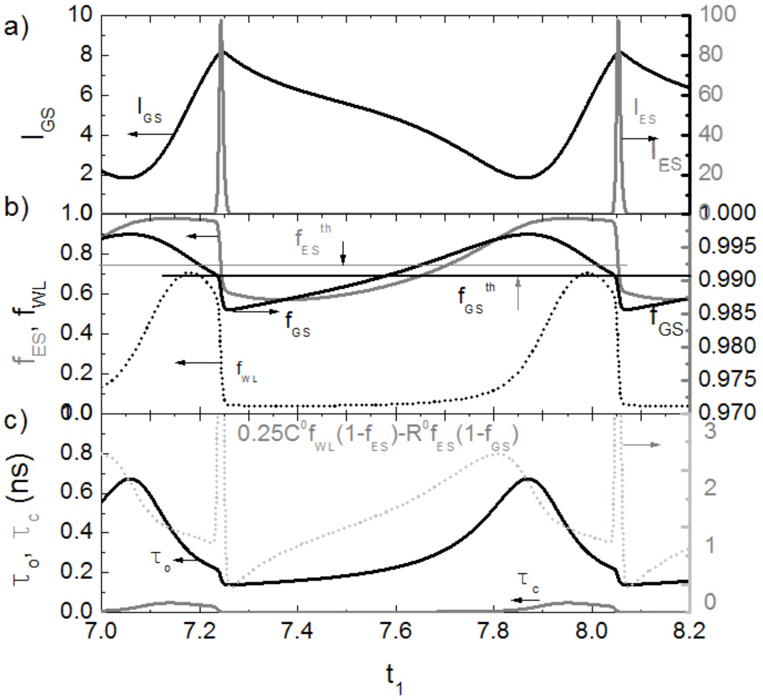

Figure 5.4: Temporal evolution of a) GS (left axis) and ES (right axis) mode intensities, b) occupation of the GS: solid black curve f_{GS} (right axis), ES: solid gray curve f_{ES} (left axis), WL: dotted black curve f_{WL} (left axis). Horizontal black and gray lines represent threshold occupation of the GS and ES, respectively. c) Modulation of the relaxation (black) and capture (gray) time resulting from changes in the occupation of the respective energy levels (left axis) and the difference between the capture $0.25C^0 f_{WL}(1 - f_{ES})$ and relaxation $-R^0 f_{ES}(1 - f_{GS})$ processes (dotted gray curve, right axis). $S_m = 6 \times 10^{-4}$ J/m^3, $\Delta = 9$ GHz.

To characterize the dynamics of the modes for the injection strength larger than 2×10^{-4} J/m^3, we show in Fig. 5.4a the time traces of the GS and ES mode intensities for fixed injection parameters $S_m = 6 \times 10^{-4}$ J/m^3, $\Delta = 9$

GHz (point A in Fig. 5.2a). As can bee seen from this figure the ES mode fires periodic pulses at a constant amplitude, which is ten times larger than the maximum intensity of the GS mode. Temporal changes of the occupation of the respective energy states are shown in Fig. 5.4b. Dynamics are governed by antiphase oscillations of the intensity and occupation of the GS caused by the optical injection. These oscillations modulate the relaxation time $\tau_o = \tau_o^0/(1 - f_{GS})$ via the Pauli blocking term (see Fig. 5.4c). Consequently, the occupation of the ES is also being modulated. In a similar way, oscillations of the occupation of the ES modulate the capture rate and influence the occupation of the WL. With the set of parameters used in the model, the GS is almost saturated meaning that small changes in its occupation cause large changes in the relaxation time. The amplitude of such modulation is 0.5 ns. The amplitude of the capture time modulation is much smaller. The large increase of the relaxation time explains the considerable increase of the occupation of the ES (well above its threshold value $f_{ES}^{th} = 0.72$) within the time corresponding to the increasing slope of the GS occupation in Fig. 5.4b. The ES occupation is governed by the capture $0.25C^0 f_{WL}(1-f_{ES})$

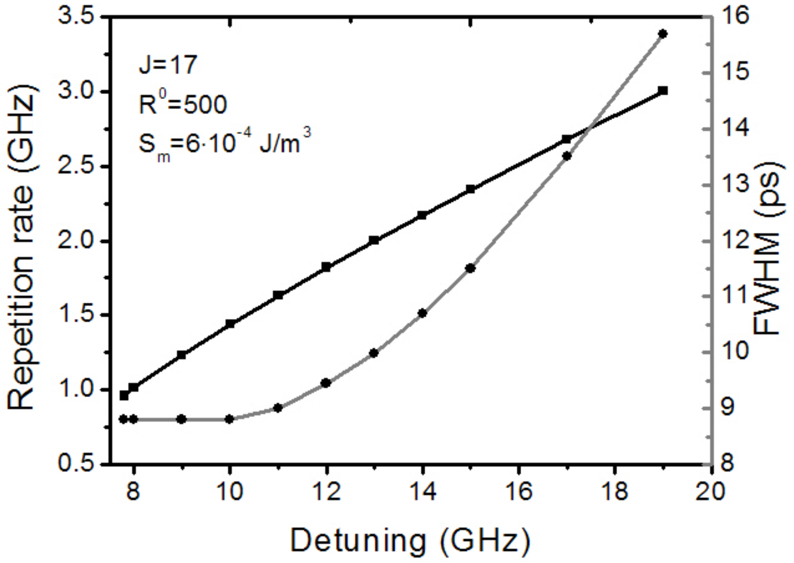

Figure 5.5: Repetition rate (black curve) and the duration (FWHM, gray curve) of pulses generated from the ES.

and relaxation $-R^0 f_{ES}(1 - f_{GS})$ processes in Eq. 5.10. The interplay of these two processes is plotted as a dotted light gray curve in Fig. 5.4c. When the occupation of the GS, and consequently the relaxation time, start decreasing after achieving their maxima, the occupation of the ES still increases for some time because the capture to the ES dominates over the process of relaxation to the GS. At some point the occupation of the ES saturates. When the decreasing occupation of the GS crosses its threshold value $f_{GS}^{th} = 0.991$, the ES fires a large intensity pulse while its occupation sharply decreases (the last, stimulated emission term in Eq. 5.10). This resembles typical gain switching mechanism and shows that modulation of the relaxation time can lead to generation of picosecond pulses. In Fig. 5.5 the pulse duration and repetition rate are plotted as a function of the detuning. In the investigated range, the pulse repetition rate increases linearly with the detuning and is of the order of a few GHz. At detuning of 8 GHz the pulse duration is as small as 8 ps. Similar values have been reported experimentally for pulses generated by a dual-wavelength mode-locked QD laser [106]. When the detuning increases however, the pulses become broader.

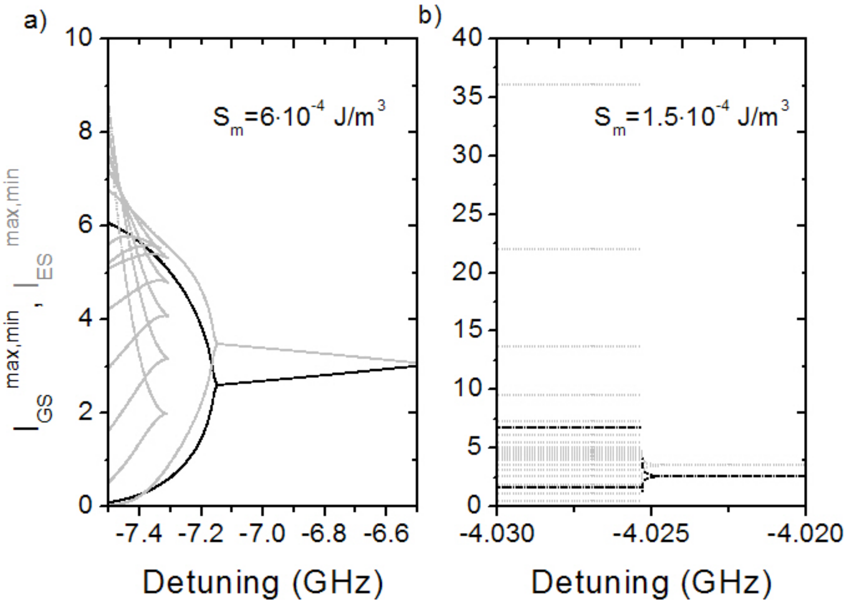

Figure 5.6: (Color online) 1-parameter bifurcation diagram for a) $S_m = 6.0 \times 10^{-4}$ J/m^3 and b) $S_m = 1.5 \times 10^{-4}$ J/m^3 showing the behavior of the GS and ES modes in close proximity of the two-mode Hopf-bifurcation.

For negative detuning, the locking region is bordered by parts of the saddle-node and Hopf bifurcation curves which meet together at the codimension-two Bogdanov-Takens point BT (Fig. 5.2b). The dynamics of the GS and ES modes in the unlocked region are characterized in Fig. 5.6, Fig. 5.7, and Fig. 5.8. Fig. 5.6 depicts the two-mode Hopf bifurcation for large (Fig. 5.6a) and small (Fig. 5.6b) injection strength. In close proximity to the Hopf bifurcation, the GS and ES modes oscillate in antiphase (not shown). As can

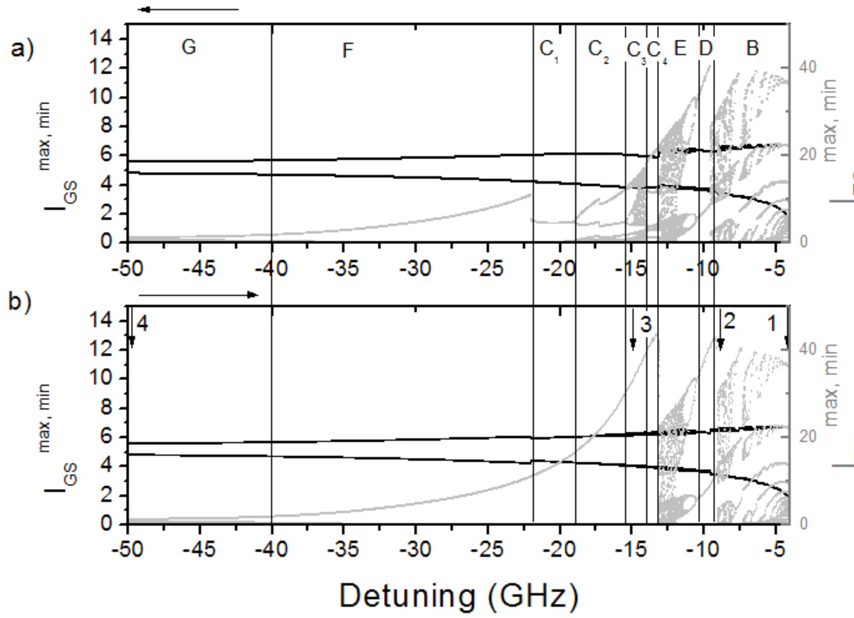

Figure 5.7: 1-parameter bifurcation diagram for $J = 17$, $S_m = 1.5\times10^{-4}$ J/m^3 for detuning when sweeping the detuning either from a) small to large or b) from large to small negative values. Arrows 1-4 correspond to time traces in Fig. 5.8-1:4.

be seen from Fig. 5.6 a number of extrema appear in the intensity of the ES mode when decreasing the detuning beyond the Hopf bifurcation point. What happens is that each time the ES mode rises above zero, its waveform follows relaxation oscillations (see also Fig. 5.8-1). Comparing Fig. 5.6a and Fig. 5.6b one can conclude that the range of detuning corresponding to the pure antiphase oscillations of the GS and ES modes depends on the injection strength and shrinks when approaching the BT point.

Fig. 5.7 presents forward and backward 1-parameter bifurcation diagram for the same injection strength as in Fig. 5.6b but for negative detuning reaching -50 GHz. As can be seen from this figure, the regular multipulse dynamics of the ES mode is followed by chaotic dynamics: region B in Fig. 5.7 (see also Fig. 5.8-2). For even larger negative values of the detuning, regular pulses with two different amplitudes are generated (region D in Fig. 5.7). These periodic dynamics undergo period doubling cascade to chaos (region E in Fig. 5.7). Similarly to the scenario presented for positive detuning, there exists a region of bistability starting from detuning of -13 GHz which extends over regions C_1-C_4 in Fig. 5.7. In region C_1 the bistability is between pulsed ES mode emission with constant, but different amplitudes of pulses (see also Fig. 5.8-3). In C_2 and C_3 one possible behavior is still associated with the pulsed ES mode

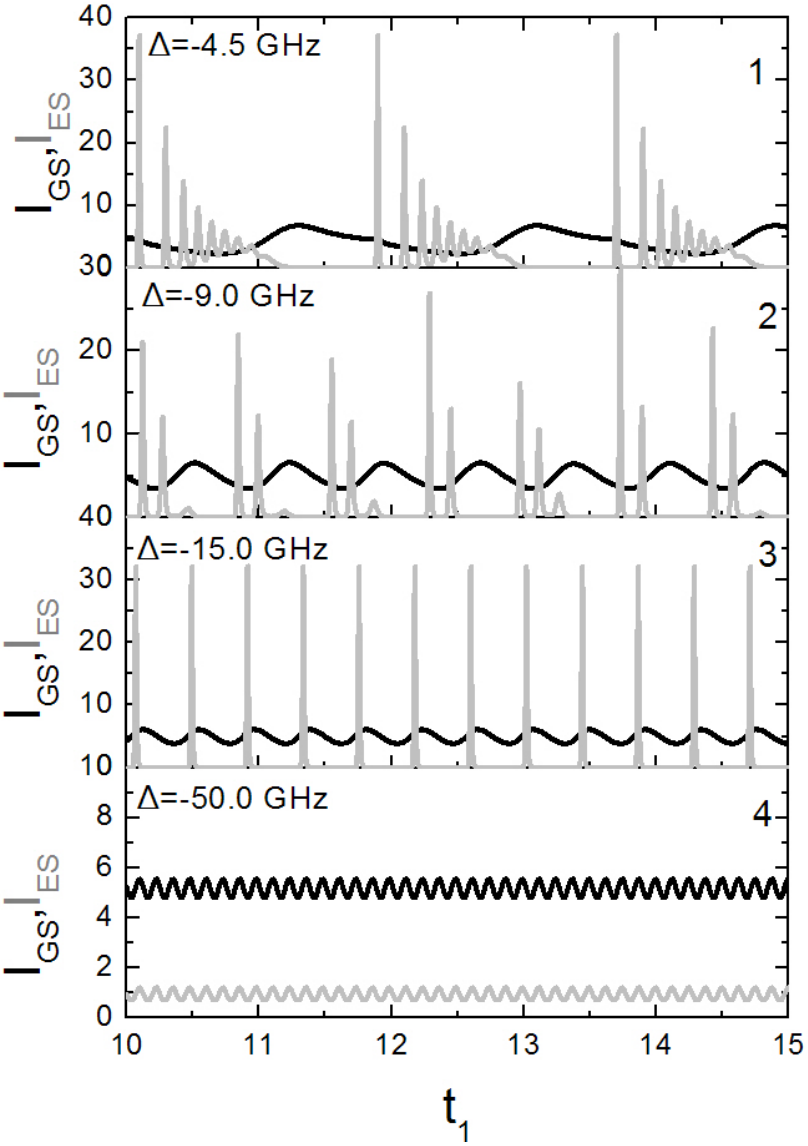

Figure 5.8: Temporal evolution of the GS and ES mode intensities for $S_m = 1.5 \times 10^{-4}$ J/m^3 and 1: $\Delta = -4.5$ GHz, 2: $\Delta = -9.0$ GHz, 3: $\Delta = -15.0$ GHz, 4: $\Delta = -50.0$ GHz.

emission with constant amplitude of pulses (panel b in Fig. 5.7) while the other one is associated with the emission of pulses which amplitudes undergo period doubling cascade to chaos when approaching region C_3 (panel a in Fig. 5.7).

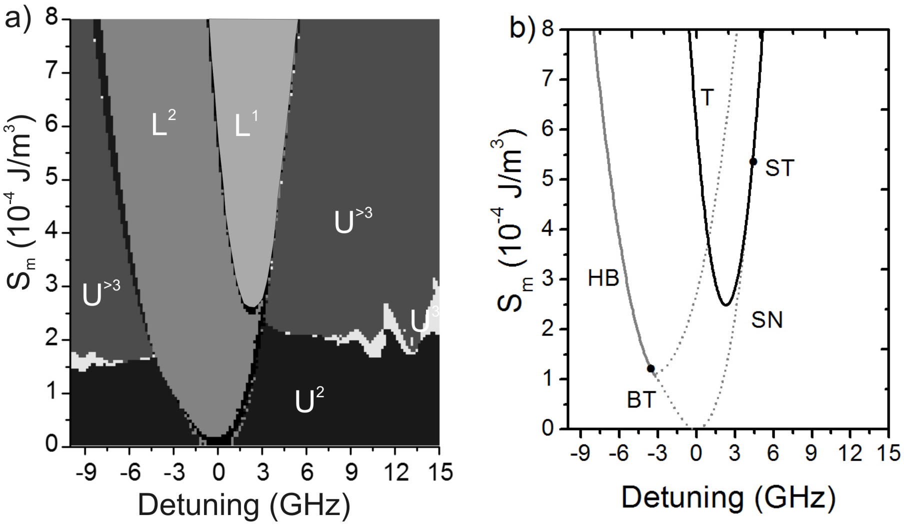

Figure 5.9: a) Extrema map for $J = 20$. b) 2-parameter bifurcation diagram calculated with AUTO [177]. The labeling and color coding is the same as in Fig. 5.2.

In region C_4 the bistability is between regular pulses with constant amplitude and multi-pulse pattern. In the region F of Fig. 5.7 the ES mode fires pulses with constant amplitude, and this amplitude becomes smaller and smaller as the detuning is increased. Finally, at the detuning larger than -40 GHz (region G in Fig. 5.7), the ES mode shows low- amplitude oscillations that are in-phase with the oscillations of the GS mode as shown in Fig. 5.8-4. Similar behavior is observed for large positive values of the detuning.

As long as the dynamics of the GS mode are limited to locking and period one time periodic oscillations, the value of R^0 does not change the overall dynamics of the ES mode. It influences, however, the size of the respective regions in the injection parameters space.

5.4 Generation of pulse packages in optically injected QD laser.

The results presented so far suggest that modulation of the capture and relaxation times induced by optical injection can switch on and off the ES mode and consecutively result in the pulsating behavior of its intensity. It is, therefore, reasonable to check if such pulsating behavior of the ES mode is maintained at higher currents. Extrema map computed for $J = 20$ is presented in Fig. 5.9a and the corresponding bifurcation diagram is shown in Fig. 5.9b.

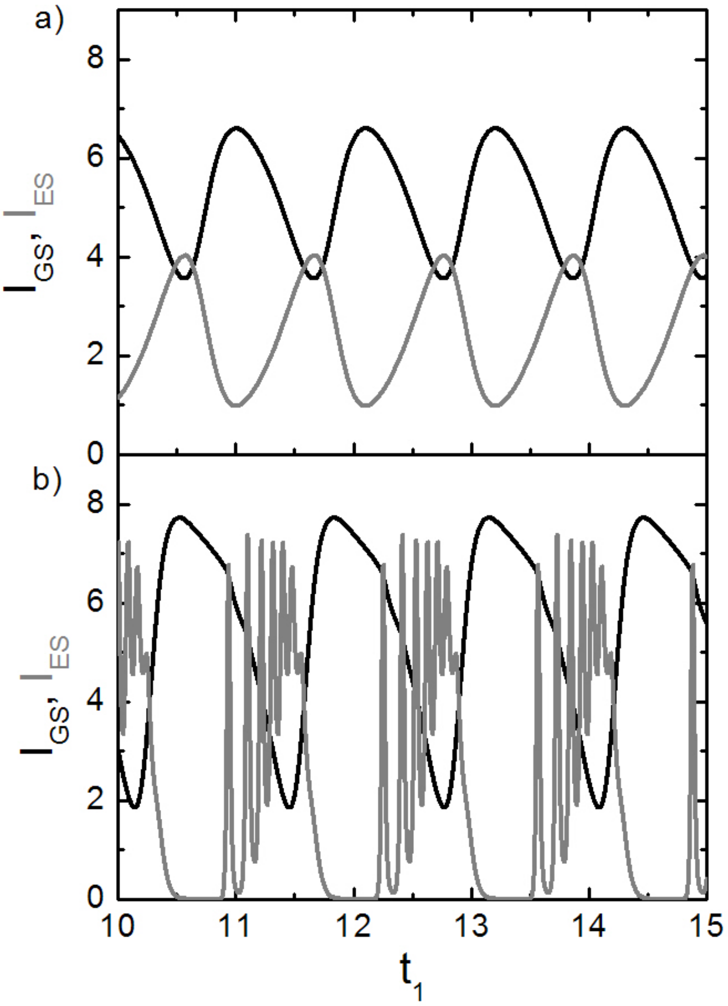

Figure 5.10: Temporal evolution of the GS and ES mode intensities for a) $S_m = 10^{-4}$ J/m^3, $\Delta = 6$ GHz, $S_m = 4 \times 10^{-4}$ J/m^3, $\Delta = 6$ GHz. $J = 20$.

Comparing the 2-parameter bifurcation diagrams in Fig. 5.2b and Fig. 5.9b one can conclude that at higher currents the region of locked, single-frequency GS mode emission shrinks and is achievable at higher injection strength. Similarly, the position of the codimension-two saddle-node-transcritical tangency point ST moves to larger injection strengths, whereas the position of the codimension-two Bogdanov-Takens point BT does not change. In the unlocked region, regardless of the sign of the detuning, at the injection strength smaller than 2×10^{-4} J/m^3 both modes oscillate in antiphase (region U^2 in

Fig. 5.10a). At higher values of S_m, however, the waveform of the ES mode builds up by emission of short-pulse packages with decreasing depth of intensity modulation (regions $U^{>3}$ in Fig. 5.10b). The frequency of spikes within the package corresponds to the relaxation oscillation frequency of the ES mode and is of the order of few GHz. It is worth noticing that the two-mode QW EEL of [103] also shows emission of pulse packages but from both modes simultaneously.

At currents larger than $J = 20$, the region of complex dynamics are attainable at a larger injection strength, so that in the range of injection parameters investigated in this paper, the ES mode can either be suppressed, when the GS mode is locked, or can exhibit period-one time periodic oscillations. Such an emission already occurs at the current when $I_{GS} > I_{ES}$, which shows that the intensity ratio of the GS and ES mode emission does not influence the overall dynamics of the system.

5.5 Summary and conclusions

To summary, this chapter presents a theoretical study on optically injected quantum dot laser lasing simultaneously from the ground and excited state. External light is injected into the ground-state mode alone, and the two lasing modes are coupled indirectly via the carrier relaxation process. We consider the range of currents where the ground-state and excited-state modes lase simultaneously in the absence of optical injection.

Our studies unveil that, in the presence of optical injection, dynamics of the ground-state mode are limited to single-frequency locking (excited-state mode suppressed), double-frequency locking (excited-state mode unsuppressed), and unlocked time-periodic intensity oscillations. Inside the locking region defined in the plane of injection strength and frequency detuning, two different types of locking are separated by a transcritical bifurcation corresponding to the lasing threshold of the excited-state mode. Outside the locking region, the excited-state mode can exhibit very complicated behavior. Our studies focused on picosecond pulses generated by a gain switching mechanism that is associated with modulation of the relaxation time caused by the injection-induced oscillations in the occupation of the respective energy states. The model predicts that pulses as short as 8 ps are achievable. The repetition rate and duration of such pulses increase with the frequency detuning of the injected signal. At even higher current, the region where the excited-state mode is suppressed and the ground-state mode is locked to the injected signal shrinks and requires higher injection strength. Outside the locking region, the intensity of the excited-state mode is no longer pulsed but it oscillates in antiphase with the intensity of the ground-state mode. For a certain set of injection parameters (region $U^{>3}$ in Fig. 5.9a), the envelope of the excited-state mode builds up by emission of short-pulse packages with decreasing depth of modulation. The frequency of the spikes within the package corresponds to the relaxation oscillation frequency of the excited state.

Chapter 6

Summary and perspectives for future work

6.1 Main achievements

Below we give a summary of our main achievements.

In Chap. 2, we have experimentally studied polarization properties of two generations of quantum dot (QD) vertical-cavity surface-emitting lasers (VCSELs), namely VCSELs with submonolayer (SML) and Stranski-Krastanov (SK) QDs. The main conclusions are as follows:

- Our investigations showed that among single-transverse-mode devices that in the investigated range of currents and temperatures exhibit stable, linearly polarized emission, polarization orientation of SK QD VCSELs changes from device to device. The distribution of the number of the devices with a given polarization orientation achieves two maxima at the x (90) and y (0) directions corresponding to the main crystallographic axes. In this regard SK QD VCSELs resemble QW devices. On contrary, polarization orientation of the investigated SML QD VCSELs is aligned with the y direction. Close to the lasing threshold this is also the case for the devices showing polarization instabilities.

- We have shown that five SK QD VCSELs (out of 24 investigated) abruptly switched their polarization to the orthogonal, linearly polarized mode when the wafer temperature was increased. Unlike in QW VCSELs however, switching has not been maintained in the consecutive measurements but the polarization direction remained orthogonal to that before the single switching event.

- Our investigation of SML QD VCSELs showed that seven devices (out of 26 investigated) exhibit very stable and reproducible polarization switching accompanied by polarization mode hopping between nonorthogonal, elliptically polarized states. Close to the lasing threshold the emission is linearly polarized. At some current it changes to stable elliptical polarization. The ellipticity and the polarization angle increase as the current is increased. Next, the region of polarization mode hopping between elliptically polarized, nonorthogonal modes starts. The distribution of the dwell time at a fixed current is exponential, which suggests that the hopping is stimulated by noise.

- We have checked which physical mechanism may be responsible for the observed polarization switching by performing a large-signal current modulation experiments. The cut-off frequency, i.e. the frequency at which no switching is observed, determined in these measurements is about 100 MHz. Since the intradot processes occur at a much faster timescale of a few tens of picoseconds we suspect that the switching is of thermal origin.

- Our results constitute the first experimental observation of polarization instabilities in solitary QD VCSELs.

The dynamics of the observed polarization mode hopping is analyzed in Chap. 3. We have shown that:

- Polarization mode hopping (PMH) takes place in an exceptionally wide range of currents. This is in contrast to PMH in QW VCSELs where it occurs in the vicinity of the current of a very abrupt polarization switching.

- Similarly to PMH in QW VCSELs both polarization modes are anticorrelated, i.e. when one mode is switched on, the remaining one in switched off. On the other hand, while in PMH in QW lasers is only symmetric at the current of an abrupt polarization switching, in QD VCSELs PMH is symmetric in the whole corresponding range of currents.

- When the current is increased, the average dwell time decreases by 8 orders of magnitude, from seconds to nanoseconds, without any external manipulation to the inherent anisotropies. To our best knowledge, this is the first observation of such behavior.

- In contrast to polarization switching involving dynamical states in QW VCSELs, after the region of PMH we observe emission of two orthogonal, linearly polarized modes. Their orientation is aligned with the directions characteristic for linearly polarized emission close to the lasing threshold before the onset of elliptically polarized emission.

In Chap. 4, we have studied theoretically temporal behavior of optically injected QD EELs paying attention to dynamics resulting in a pulsed output, i.e. self-pulsations and excitability. In particular:

- we have extended the model for optically injected QD laser system to account for the QD excited states.

- Our systematic study of bifurcations of the system dynamics in the plane detuning vs. injection strength using continuation techniques shows that the relaxation time strongly influences the size of regions of solutions emerging from the respective bifurcations. The capture time has a minor effect. We show that the waveform of the emitted signal is greatly determined by the fluctuations in the occupation of the excited state.

- In close proximity of the codimension-two saddle-node Hopf bifurcation point for the negative detuning we have unveiled a region of complex dynamics including bistability, period-one and period-two time-periodic, and chaotic oscillations.

- Close to the saddle-node on limit cycle bifurcation bordering the locking region we have identified regions of deterministic self-pulsations. Such self-pulsations appear for both positive and negative detuning. For completeness we also show self-pulsations associated with saddle-node homoclinic orbit bifurcation that can be triggered inside the homoclinic tooth.

- We have studied the interpose time distribution for self-pulsations in the deterministic system. We show that the pulses are periodic regardless of the detuning but the interpose time does depend on the detuning and follows the inverse square root scaling law. This suggests that the deterministic self-pulsations are due to the bottlenecking phenomena. We have also studied the interpose time distribution in the presence of spontaneous emission noise. In this case the periodicity of pulses is not preserved for all values of the detuning within the region of self-pulsations. Close to the saddle-node bifurcation the interpose time follows a skewed normal distribution, which becomes sharp as the detuning increases. Also the repetition rate increases with the detuning. These results agree with the experimental findings for the dynamics of excitable pulses.

- We have studied the influence of the noise strength on the interpose time distribution and identify two possible behaviors. Close to the locking region the spontaneous emission noise influences the dynamics of self-pulsations in the same way as the detuning does, that is, it shifts the mean toward smaller values and makes the pulsations more and more periodic. In contrast, for larger values of the detuning the standard deviation quickly saturates when the noise strength is increased, whereas the mean seems not to be influenced.

- Finally, we have studied the performance of an optically injected QD laser used for all-optical signal reshaping or regeneration. In our approach, the information signal acts as a master laser and switches the slave QD laser between the regions of locking and self-pulsations. The maximum bit rate of such a system is determined by the mean of the interpose time distribution for a given noise strength. In the deterministic system it amounts to 0.5 GHz. We have proposed a correction method that is based on an a-priori computation of the statistics of these delays (activation time) that can improve the maximum bandwidth of the system to 1 GHz.

In Chap. 5, we have studied theoretically nonlinear dynamics of optically injected quantum dot laser lasing simultaneously from the ground and excited state. Our studies unveil that:

- in the presence of optical injection, dynamics of the ground-state mode are limited to single-frequency locking (excited-state mode suppressed), double-frequency locking (excited-state mode unsuppressed), and unlocked time-periodic intensity oscillations. Inside the locking region defined in the plane of injection strength and frequency detuning, two different types of locking are separated by a transcritical bifurcation corresponding to the lasing threshold of the excited-state mode.

- Outside the locking region, the excited-state mode can exhibit very complicated behavior. We have unveiled the regime of picosecond pulses generation as caused by a gain switching mechanism. The gain switching arises due to modulation of the relaxation time by the injection-induced oscillations in the occupation of the respective energy states. Our model predicts that pulses as short as 8 ps are achievable. The repetition rate and duration of such pulses increase with the frequency detuning of the injected signal.

- At larger current, the region where the excited-state mode is suppressed and the ground-state mode is locked to the injected signal shrinks and requires higher injection strength. Outside the locking region, the intensity of the excited-state mode is no longer pulsed but it oscillates in antiphase with the intensity of the ground-state mode. For a certain set of injection parameters, the envelope of the excited-state mode builds up by emission of short-pulse packages with decreasing depth of modulation. The frequency of the spikes within the package corresponds to the relaxation oscillation frequency of the excited state.

6.2 Perspectives for future work

Our experimental studies on polarization properties of solitary QD VCSELs motivate further experimental and theoretical work that would help to understand the peculiar way of polarization switching and polarization mode hopping in SML-QD devices. Some similarities to polarization switching involving dynamical states in QW VCSELs show that the observed behavior can be influenced by the contributions from nonlinear anisotropies, which, in turn, may be governed by spin dynamics. It is, therefore, important to study the dynamics and polarization properties of the excitonic complexes in both single QD and an ensemble as a whole at temperatures that are typical for high-speed applications of lasers. Such studies should answer the questions of which complexes dominate at given conditions and whether competition between them can stimulate polarization instabilities. Gaining a deeper understanding of the underlying physics would help to develop QD VCSELs emitting light which polarization is either stable regardless of the operation conditions or can be switched in a controlled manner.

The natural continuation of our work on optically injected QD EELs is optical injection in QD VCSELs. In contrast to optical injection in EELs, optical injection in VCSELs requires the inclusion of an extra degree of freedom from polarization. For example, as shown in [189], injected light with polarization perpendicular to that of a free-running slave QW VCSEL can induce bistable polarization switching. These effects have been extensively studied for many years for fundamental aspects of nonlinear dynamics and for applications in optical memories [190], optical inverters [191] etc. The ultimate goal of this study would be the experimental verification of our theoretical predictions on different dynamics resulting in pulsed output and identification of the contributions from the polarization state of light. Specifically, it seems to be interesting to investigate these effects in the regime involving nonorthogonal states.

Chapter 7

Résumé en français

Vrije
Universiteit
Brussel

Supélec

paul
erlaine
université - metz

Propriétés de polarisation et dynamique non-linéaire de lasers à boîtes quantiques

Lukasz Olejniczak

7.1 Introduction

Les lasers à semi-conducteurs sont des composants clés de notre vie de tous les jours, avec des applications allant des télécommunications optiques et du stockage de données au traitement médical et à la production industrielle. Premièrement, cette position économique forte est la conséquence de leurs nombreux avantages: faible consommation de puissance, fonctionnement continu monomode à température ambiante, spectre large de longueurs d'ondes disponibles et possibilité de modulation directe. De plus, il y a une demande forte pour des sources compactes et fiables de lumière cohérente qui ne nécessitent pas d'alimentation externe de puissance ni de systèmes de refroidissement volumineux et coûteux.

Les lasers à semi-conducteurs disponibles commercialement sont essentiellement basés sur des structures à puits quantiques, qui sont des nanostructures confinant les porteurs de charge en une dimension spatiale. Des améliorations ont été possibles par le développement de boîtes quantiques à semi-conducteurs (quantum dots ou QDs), c'est-à-dire des nanostructures confinant les porteurs de charge dans les trois dimensions spatiales. Un tel confinement conduit à une distribution d'énergie discrète, ressemblant à un système laser atomique, permettant ainsi d'améliorer l'efficacité de l'émission laser. Une contribution principale de cette thèse est d'étudier les propriétés de polarisation de la lumière émise par de tels lasers à boîtes quantiques mais avec la géométrie d'une cavité verticale, c'est-à-dire des VCSELs (vertical-cavity surface-emitting lasers). Les lasers à cavité verticale émettent la lumière dans une direction verticale, perpendiculaire à la surface de la région active. Un comportement couramment observé dans les VCSELs à puits quantiques est un échange abrupte de puissance entre deux polarisations linéaires et orthogonales lorsque les conditions de fonctionnement du laser (courant d'injection et/ou température) varient. Un tel phénomène est qualifié de basculement de polarisation. Il se produit souvent sous la forme d'un phénomène aléatoire alimenté par le bruit d'émission laser, c'est-à-dire un saut aléatoire et continu dans le temps entre les modes de polarisation. Nos études sont intéressantes du point de vue fondamental parce qu'elles éclairent nos connaissances de l'interaction lumière-matière à l'échelle nanométrique. L'importance croissante des QD VCSELs pour des applications de communications de données montre cependant l'intérêt de nos études également sur le plan applicatif: de telles instabilités de polarisation conduisent à une dégradation des performances du système en terme de rapport signal à bruit et donc de taux d'erreur binaire. Notre motivation principale est donc de vérifier si de telles instabilités de polarisation courantes dans les VCSELs à puits quantiques (QW VCSELs) sont également présentes dans les QD VCSELs. Nous avons analysé des VCSELs obtenus par croissance de boîtes quantiques par la méthode de Stranski-Krastanov (SK) ou par la méthode dite *sub-monolayer* (SML), et fonctionnant avec un seul mode transverse d'émission (mode gaussien). Le premier mode de croissance (SK) se produit lorsqu'il y a un désaccord de maille important entre le substrat et le matériau déposé, par ex. les constantes cristallographiques de GaAs (5.6533 Å) et InAs (6.0583 Å) conduisent à un désaccord de maille de 7 %. La croissance consiste en la formation d'un puits quantique contraint, appelé *wetting layer* (WL), et lorsque son épaisseur devient critique la contrainte accumulée conduit à la formation d'ilots tridimensionnels boîtes quantiques. Dans la croissance SML il n'y a pas de *wetting layer* et les boîtes quantiques sont obtenues par dépôt d'un superlattice constitué de fines monocouches.

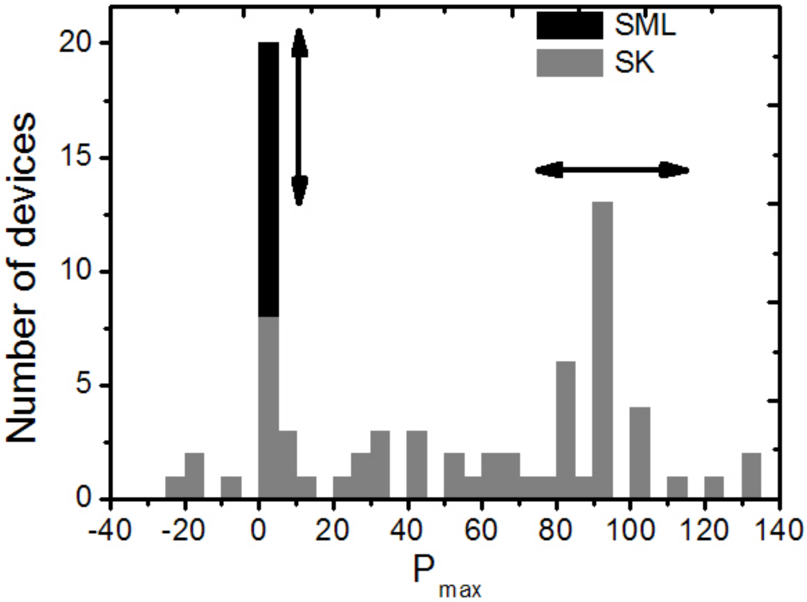

Figure 7.1: Distribution de l'orientation de polarisation (P_{max}) pour des QD VCSELs obtenus par croissance de type SK (gris) ou SML (noir). Les orientations 0 et 90 correspondent aux axes cristallographiques principaux.

Dans cette thèse nous étudions aussi les propriétés dynamiques de lasers à boîtes quantiques émettant par le côté (EEL ou edge-emitting laser), soumis à injection optique, c'est-à-dire qu'une lumière externe émise par un laser dit maître est injectée dans la cavité du laser esclave à boîtes quantiques. Dans les lasers à puits quantiques, cette technique a été proposée pour l'étude des propriétés fondamentales de systèmes optiques non linéaires [50, 89, 90] et fournit des moyens additionnels pour améliorer les performances du laser en stabilité, largeur de raie et bande passante de modulation [91, 92, 93]. Les caractéristiques particulières des lasers à boîtes quantiques comparés aux lasers à puits quantiques, à savoir leur faible facteur d'accroissement de largeur de raie [56] et leurs oscillations de relaxation fortement amorties [94], peuvent

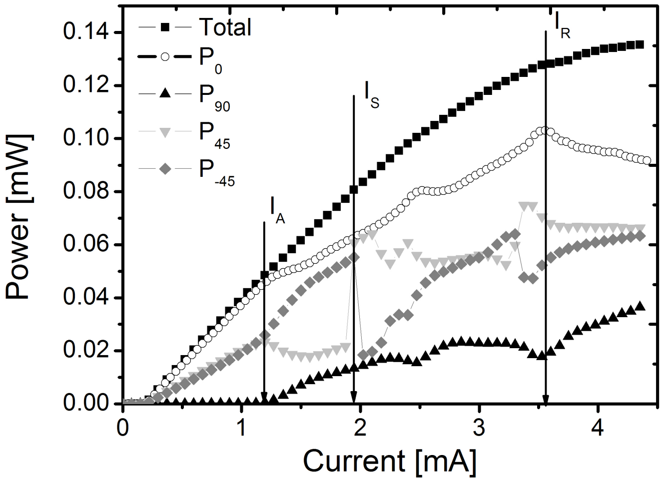

Figure 7.2: Caractéristique puissance-courant typique des lasers QD VCSELs analysés. Les notations P_i correspondent à des puissances mesurées avec une orientation de i degrés par rapport à une polarisation linéaire selon l'axe y.

influencer la dynamique non linéaire du laser en présence d'injection optique et résulter en des dynamiques différentes de celles observées dans les lasers à puits quantiques. Les premiers résultats expérimentaux sur les lasers à boîtes quantiques en présence d'injection optique révèlent, par exemple, l'existence de régions dans l'espace des paramètres (défini par le désaccord en fréquence maître-esclave et la puissance injectée) où le laser répond au signal injecté par l'émission d'impulsions courtes dites excitables, avec éventuellement l'émission non pas d'une impulsion mais de deux impulsions [95]. Alors que l'excitabilité est une propriété commune à de nombreux systèmes dans la nature et a été rapportée pour des lasers soumis à rétroaction optique [96], [97] et avec absorbant saturable [98], c'était la première fois qu'un tel comportement a été observé dans un laser avec injection optique.

Pour comprendre la dynamique de tels systèmes (QD VCSELs et QD EELs avec injection optique) nous souhaitons contribuer également à l'étude physique des boîtes quantiques. Une des particularités des lasers QD est leur dynamique plus compliquée des porteurs, qui étant capturés depuis la couche humide dans les boîtes, contribuent à des transitions radiatives par transitions successives par des états excités. Ces processus sont caractérisés par les temps de capture et de relaxation, respectivement. Ces deux constantes de temps ont été montrées comme influençant les performances de lasers QD en termes de bande passante et modulation et courant de seuil [57, 99, 100]. Nous souhaitons dès lors vérifier l'impact de ces deux constantes de temps sur la dynamique d'un laser QD avec injection optique.

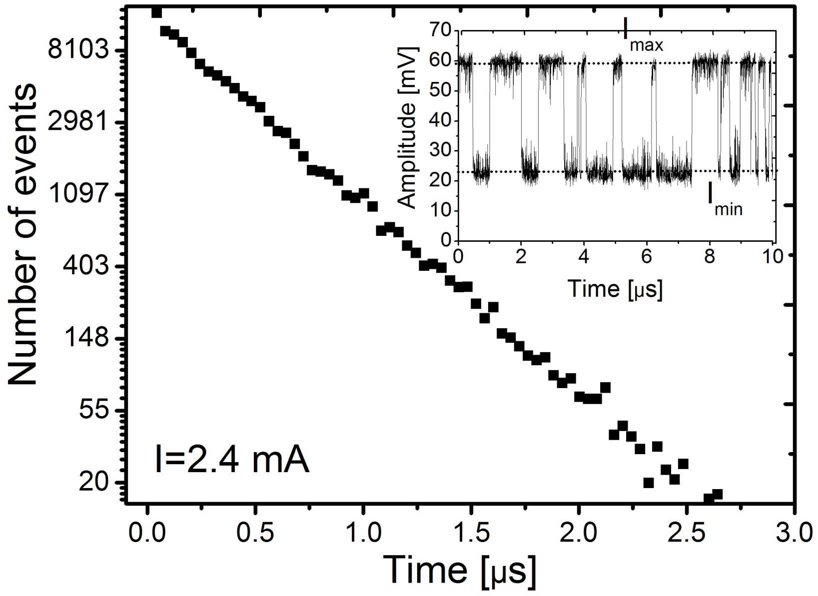

Figure 7.3: Distribution du temps de séjour dans un mode de polarisation, pour un courant d'injection de 2.4 mA dans la région de dynamique de saut de mode de polarisation. Un exemple de dynamique est présenté dans l'encart, pour une orientation du polariseur de 45 degrés, correspondant à une amplitude maximale du basculement de polarisation.

Pour répondre à cette question nous avons étendu le modèle présenté en [95] pour tenir compte des états excités et nous avons réalisé une cartographie des bifurcations dans le plan des paramètres de l'injection optique, c'est-à-dire désaccord en fréquence et puissance injectée. Nous portons une attention particulière aux dynamiques résultant en une émission pulsée, à savoir excitabilité et pulsations auto-entretenues, qui si elles sont suffisamment rapides peuvent conduire à des applications intéressantes. En particulier, nous voulons montrer comment les dynamiques de ces émissions pulsées sont influencées par le bruit d'émission spontanée et les paramètres de l'injection. Finalement, nous souhaitons utiliser ces dynamiques pour la re-génération de signal toute optique. Dans notre approche simple, le signal d'information atténué et déformé sert de signal maître qui conduit le laser esclave QD à basculer entre les régions de blocage par injection et auto-pulsations.

Dans les lasers à boîtes quantiques, le nombre fini de boîtes quantiques dans la région active et la structure d'énergie discrète des boîtes quantiques peut conduire à la saturation de l'état fondamental à des courants pourtant relativement faibles. En conséquence, l'occupation des états excités augmente

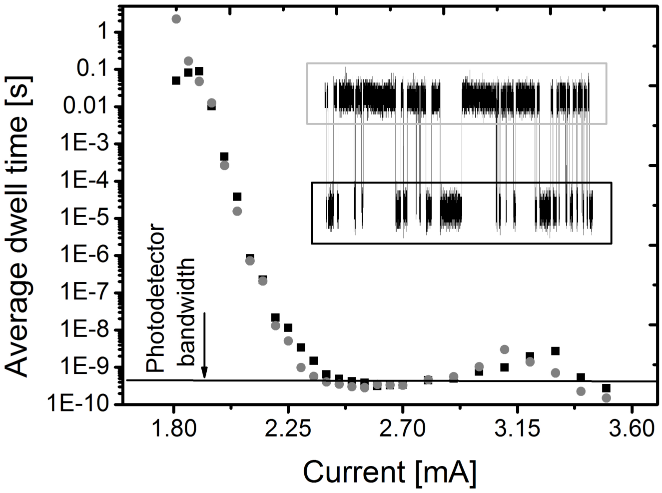

Figure 7.4: Temps de séjour dans un mode de polarisation en fonction du courant d'injection du laser. Mesure effectuée sur chacun des modes EP du laser (noir et gris), pour une orientation du polariseur de 45 degrés.

avec le courant d'alimentation et le laser peut se mettre à émettre simultanément sur l'état excité et l'état fondamental. L'émission simultanée de ces deux états d'énergie a été démontrée pour un laser QD seul dans [31, 58, 104]. Ce problème a également été étudié pour un laser QD soumis à rétroaction optique [105] et pour un blocage de modes dans un système à deux longueurs d'onde [106]. Dans cette thèse nous étudions un tel système dit *laser à deux couleurs* en présence d'injection optique, et plus particulièrement nous nous intéressons à l'émergence de dynamiques non linéaires. Contrairement au cas de lasers QW multimodes [103], dans notre modèle de laser QD les différents modes sont associés à différents réservoirs de porteurs, correspondant aux états fondamentaux et excités. Ces réservoirs sont couplés par des procédés de relaxation et se remplissent en cascade avec différents taux déterminés par les taux de capture et de relaxation. Des oscillations dans l'occupation de l'état fondamental, causées par l'injection optique, vont donc donner lieu à des oscillations dans l'occupation de l'état excité. De telles oscillations peuvent conduire à un mécanisme de basculement de gain (*gain switching*) et donc conduire à l'émission d'impulsions courtes (picosecondes) ou des paquets d'impulsions courtes à la longueur d'onde de l'état excité.

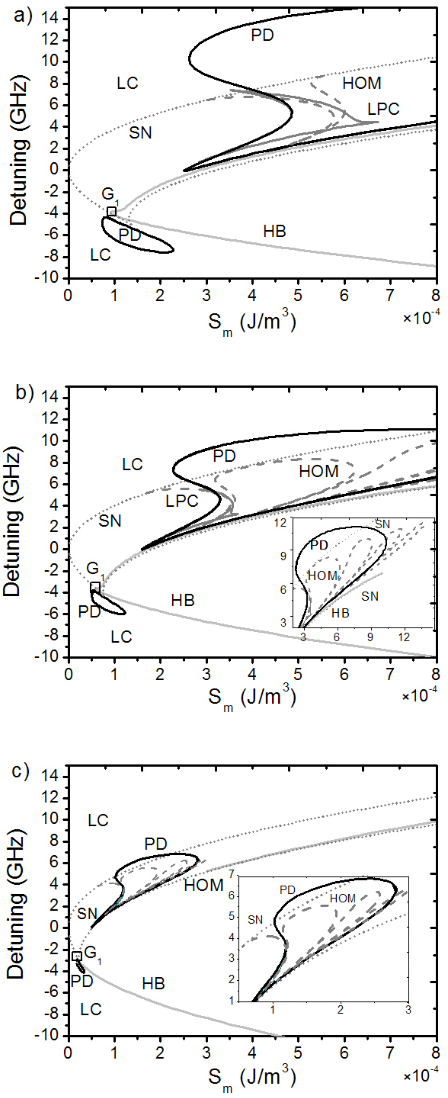

Figure 7.5: Diagramme des bifurcations dans le plan 2D des paramètres de l'injection optique (désaccord en fréquence et puissance injectée), et pour des valeurs décroissantes du taux de relaxation normalisé: a) 1020, b) 500, c) 200. Le modèle et les paramètres sont précisés dans le texte complet en anglais. HB: bifurcation de Hopf, SN: bifurcation point de selle, PD: doublement de période, HOM: bifurcation homoclinique, LPC: point de selle sur un cycle limite, LC: cycle limite, G_1: point de codimension-2 à l'intersection des courbes SN et HB.

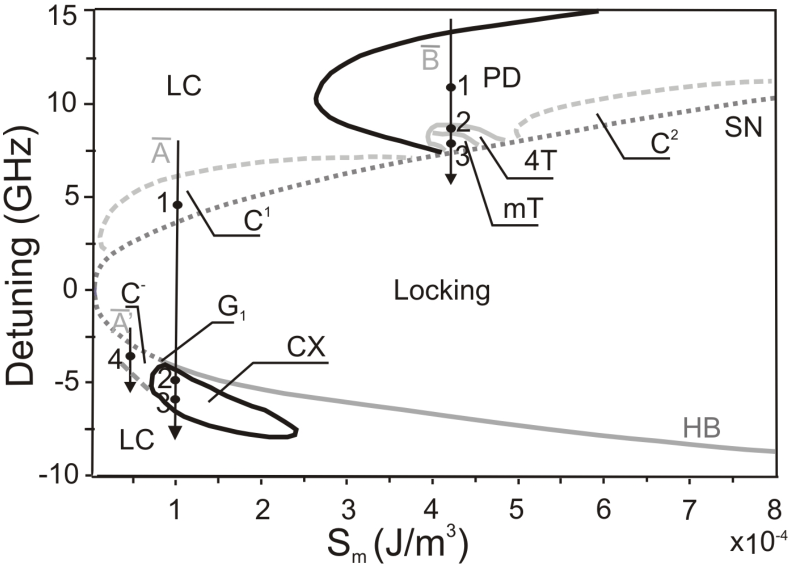

Figure 7.6: Cartographie des bifurcations d'un laser QD EEL avec injection optique, dans le plan des paramètres de l'injection: désaccord en fréquence vs. puissance injectée. a) C^1: région de dynamique pulsée auto-entretenue avec émission d'une impulsion à chaque période, C^2: idem mais deux impulsions émises par période, 4T: idem mais 4 impulsions par période, mT: dynamique chaotique. La région CX est une région de dynamique complexe entourée par une bifurcation de doublement de période. C^- est une région de dynamique pulsée auto-entretenue dans les valeurs négatives du désaccord en fréquence.

7.2 Instabilités de polarisation de QD VCSELs

Dans notre expérience nous avons analysé les propriétés de polarisation de 50 VCSELs à boîtes quantiques à fonctionnement monomode transverse : 24 obtenus par croissance de type SK et 26 obtenus par croissance de type SML. La figure 7.1 montre la distribution de l'orientation de polarisation des deux types de QD VCSELs. Comme le montre cette figure, dans le cas de QD VCSELs de type SK, l'orientation de la polarisation de la lumière émise varie d'un composant à l'autre. La distribution cependant présente deux maxima selon les directions x (90) et y (0) correspondant aux axes cristallographiques principaux. Dans ce sens ces lasers QD VCSELs SK ont un comportement semblable à celui de lasers QW. Au contraire, l'orientation de polarisation de tous les QD VCSELs de type SML est alignée avec la direction y.

Dans le cas de QD VCSELs SML, 7 composants présentent un basculement de polarisation très stable et reproductible accompagné de sauts de mode entre des états polarisés elliptiquement et non orthogonaux. Les propriétés principales du basculement de polarisation observé sont résumées dans la courbe

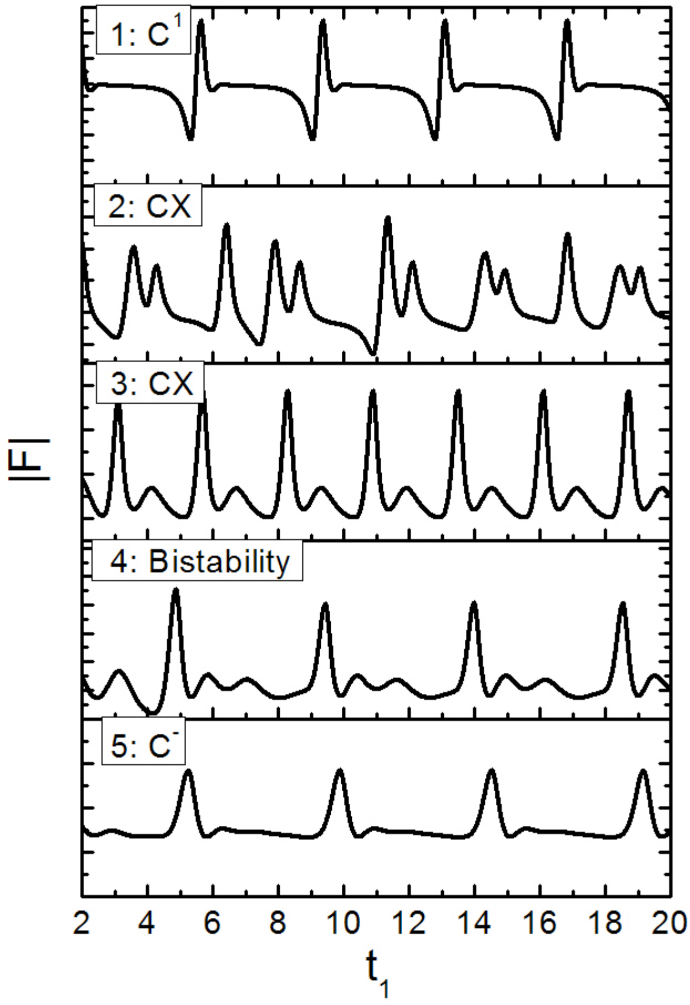

Figure 7.7: Evolution temporelle de l'amplitude du champ optique F, dans le cas de dynamiques pulsées auto-entretenues observées dans les différentes régions notées C^1, CX, C^-. Les labels 1 à 5 correspondent aux points indiqués dans le diagramme de bifurcation de la figure 7.6, le long des flèches A et A'.

puissance-courant de la figure 7.2. La puissance totale émise par le laser est représentée par les carrés noirs. Près du seuil laser, le laser émet une lumière polarisée linéairement selon la direction P_0 (mode LP_1, cercles ouverts) (l'angle de la direction de polarisation est notée par un indice càd que P_{20} signifie une polarisation orientée à 20 degrés de l'axe y). Quand le courant augmente, au point I_A la puissance mesurée dans la direction P_{90} (triangles noirs) augmente. Cette direction correspond à un mode polarisé linéairement et orthogonal qui est fortement atténué au seuil laser (mode LP$_2$). Le point I_A correspond donc au début d'une émission polarisée elliptiquement (mode EP_1). Quand le courant augmente au-delà de la valeur I_A, l'ellipse de polarisation du mode EP_1 tourne graduellement, jusqu'au point I_S où l'axe principal de l'ellipse est orienté selon la direction notée P_{-20}. Son ellipticité augmente également graduellement jusque 10%. A ce point I_S, un autre mode polarisé elliptiquement apparaît (mode EP_2) et un basculement de polarisation est observé. Pour des courants supérieurs à I_S, le laser présente des sauts de mode de polarisation entre EP_1 et EP_2. L'axe principal de EP_2 est aligné selon la direction P_{20}, ce qui montre que les modes EP_1 et EP_2 ne sont pas orthogonaux [159]. L'amplitude du basculement de polarisation change en modifiant l'orientation du polariseur et atteint un maximum pour les directions P_{45} et P_{-45} [159]. Les caractéristiques puissance-courant dans ces deux directions sont représentées dans la figure 7.2 par les triangles et carrés gris, respectivement. La région de saut de mode de polarisation s'étend jusqu'à la valeur de courant I_R. La figure 7.3 montre dans son encart un exemple de trace temporelle d'intensité dans la dynamique de saut de mode de polarisation. Etant donné que le laser ne fonctionne que dans un seul mode transverse gaussien et que dans la région de saut de mode de polarisation la puissance totale émise reste constante dans le temps, on peut s'attendre à ce que la dynamique observée dans les deux modes en compétition (polarisés elliptiquement) soit anticorrélée, à savoir lorsqu'un mode émet l'autre mode est éteint. La dynamique d'un seul des deux modes est donc suffisante pour analyser la dynamique du saut de mode. Cette trace temporelle a été mesurée pour une orientation du polariseur correspondant à une amplitude maximale du basculement de polarisation, càd que I_{max} et I_{min} correspondent à des projections des états polarisés elliptiquement selon ces deux directions. Pour caractériser le saut de mode de polarisation nous mesurons la distribution du temps de séjour, c'est-à-dire du temps que le système passe dans un mode avant de basculer dans l'autre mode. La distribution est calculée sur base de 10^4 événements. Comme le montre la figure 7.3 la distribution est exponentielle, comme cela a été également observé pour le saut de mode de polarisation d'un VCSEL à puits quantiques. Cela traduit une dynamique de sauts entre deux états stables entretenus par le bruit interne au laser.

Comme mentionné précédemment, la région de basculement de polarisation commence au point I_S et s'étend jusqu'au point I_R. Cet intervalle de courant dans lequel la polarisation est instable est très grand par rapport aux résultats publiés pour les VCSELs à puits quantiques, pour lesquels le saut de mode de polarisation se produit dans un intervalle très faible de courant au voisinage du point de basculement de polarisation [150]. Une autre différence par rapport aux observations faites sur les QW VCSELs est l'échelle de temps du saut de mode de polarisation pour différentes valeurs de courant. La figure 7.4 trace la dépendance du temps de séjour en fonction du courant d'injection.

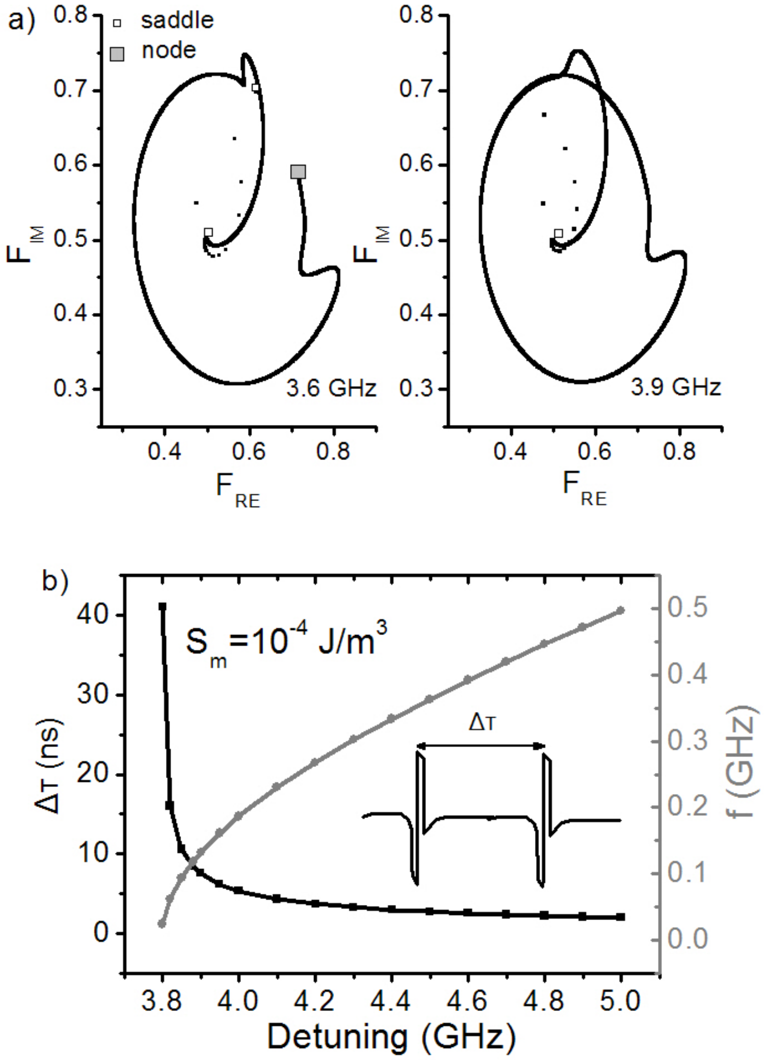

Figure 7.8: a) Espace de phase partie réelle vs. partie imaginaire du champ optique F. Illustration de la trajectoire du système pour deux valeurs du désaccord en fréquence. Les positions du point de selle et du nœud correspondant au blocage par injection sont notées par les carrés vide et plein respectivement. b) Evolution du temps entre les impulsions d'intensit du régime dynamique pulsé auto-entretenu (cf. encart), pour plusieurs valeurs du désaccord en fréquence. A droite évolution de la fréquence correspondante.

Contrairement aux conclusions obtenues sur les QW VCSELs, dans nos QD VCSELs le temps de séjour décroit avec l'augmentation du courant d'injection. Cette décroissance est de 8 ordres de grandeur: de la seconde à la nanoseconde, et ceci est observé sans aucune modification des anisotropies internes au VCSEL et dans un intervalle de courant égal à 8 fois le courant de seuil!

Pour vérifier quel mécanisme physique peut être à l'origine du basculement de polarisation dans nos composants lasers, nous avons réalisé une expérience de modulation de courant à grand signal. La profondeur de modulation est suffisamment grande pour permettre de traverser la région de saut de mode de polarisation. Au-delà d'une fréquence de modulation de 100 MHz, le laser ne parvient plus à basculer de polarisation. Cette fréquence basse définissant la fréquence limite de basculement de polarisation, laisse à penser que le mécanisme de basculement est d'origine thermique donc lent.

Nous avons également analysé le spectre optique de l'émission laser pour une valeur de courant supérieure à I_S. En tournant le polariseur nous avons pu mettre en évidence nos deux modes polarisés elliptiquement et non orthogonaux, et constater que leur séparation en fréquence est proche de 2 GHz (c'est-à-dire également proche de la résolution de notre interféromètre Fabry-Pérot à balayage). Cependant, en plus du pic principal correspondant à l'émission dans l'un de ces deux modes EP, le spectre optique présente deux raies latérales symétriquement distribuées autour du pic principal et espacées du pic principal par environ 8 GHz. Une analyse de la fréquence d'oscillations de relaxation du laser, extrapolée à cette valeur élevée du courant d'injection, permet de confirmer que ces raies correspondent à des oscillations de relaxation non amorties. Autrement dit, le basculement de polarisation entre les modes EP implique des dynamiques à la fréquence des oscillations de relaxation du laser. Cette observation définit un nouveau scénario de basculement. Dans le cas de VCSELs à puits quantiques, une seule observation expérimentale de dynamiques accompagnant le basculement de polarisation a été rapportée, et met en évidence une dynamique à la fréquence de la biréfringence effective [126].

7.3 Pulsations auto-entretenues dans un QD EEL

Comme tout laser à semi-conducteurs, les lasers à boîtes quantiques sont sensibles à la fois à la lumière ré-injectée après réflexion sur un élément optique (rétroaction optique) et à la lumière injectée par un laser externe appelé laser maître (injection optique). Leur faible coefficient d'accroissement de largeur de raie fait de ces lasers également de bons candidats pour l'étude de dynamiques non linéaires difficilement observables dans les lasers EELs ou VCSELs à puits quantiques. Dans cette section, nous étudions théoriquement la dynamique d'un laser QD soumis à injection optique, et plus spécifiquement l'influence de la physique du laser QD sur les bifurcations observées. A cette fin nous utilisons un outil numérique de continuation et d'analyse de bifurcations, AUTO-07P [177]. La figure 7.5 présente quelques premiers résultats. Sont tracés des diagrammes de bifurcations 2D, dans le plan des paramètres:

désaccord en fréquence et puissance injectée, pour des valeurs décroissantes du taux de relaxation. Dans tous les cas, les diagrammes montrent une bifurcation en point de selle (SN), une bifurcation de Hopf (HB), une bifurcation homoclinique (HOM), une bifurcation de doublement de période (PD) et un bifurcation de type point de selle sur une solution périodique (LPC). Les courbes de bifurcation SN et HB délimitent la région de blocage par injection (injection locking) pour les valeurs négatives du désaccord en fréquence, alors que c'est la courbe SN qui délimite la région de blocage par injection pour les valeurs positives du désaccord en fréquence.

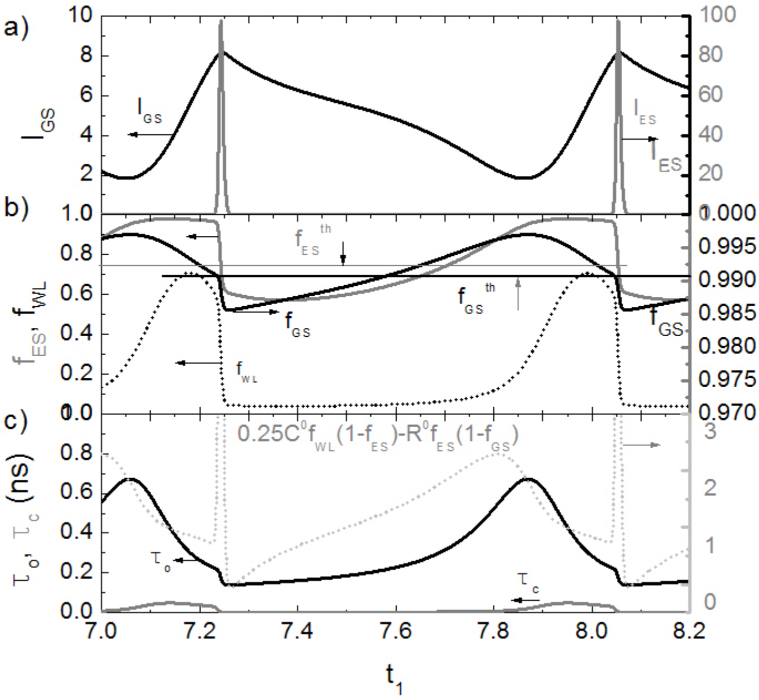

Figure 7.9: Illustration d'un mécanisme de basculement de gain conduisant à l'émission d'impulsions courtes dans l'intensité émise par l'état excité (ES). Evolution temporelle: a) intensités dans les modes GS (axe gauche) et ES (axe droit), b) occupation dans les états GS (f$_{GS}$, axe droit), ES (f$_{ES}$, axe gauche), WL (axe gauche). Les courbes notées *th* sont les courbes de seuil d'occupation des états GS et ES. C) Modulation des temps de relaxation (τ_o) et de capture (τ_c). Les paramètres du modèle sont détaillés dans le texte complet en anglais.

En comparant les cas (a) à (c) on constate que le taux de relaxation influence fortement les régions des parametres où des dynamiques complexes peuvent être observées, délimitées par les points de bifurcation. Quand la transition de l'état excité (ES) vers l'état fondamental (GS) est rapide, càd pour des valeurs grandes du taux de relaxation, les résultats sont identiques à ceux publiés dans Ref. [95]. Des valeurs plus faibles du taux de relaxation conduisent cependant à un agrandissement de la région de blocage par injection et à un décalage du point G_1 où les courbes SN et HB sont tangentes, vers les valeurs plus faibles de la puissance injectée. Nous avons vérifié que le taux de capture n'influence pas la dynamique observée lorsqu'il est compris dans l'intervalle 1-10 ps.

Dans la figure 7.5, la courbe de bifurcation homoclinique se superpose avec des parties de la courbe SN qui délimite la région de locking. Cependant, pour certaines valeurs de la puissance injectée, la courbe quitte la courbe SN et forme ce que l'on appelle une *homoclinic tooth* (HOM), qui également pénètre dans la région de locking. Comme il a été montré pour un laser QW avec injection optique [179], la courbe HOM constitue une frontière entre des dynamiques qualitativement différentes résultant en une émission pulsée : soit excitabilité soit pulsation auto-entretenue. En d'autres mots, lorsque l'on approche la courbe HOM et avant l'apparition de pulsation auto-entretenue, le laser est excitable càd qu'une perturbation suffisamment forte peut conduire à l'émission d'une impulsion dans les variables d'tat du système. Comme démontré en [160], le laser QD peut également générer deux impulsions au lieu d'une suite à la présence de la bifurcation en doublement de période.

Le laser QD peut également être excitable pour des paramètres au-delà de la courbe HOM, plus spécifiquement lorsque la courbe de bifurcation homoclinique se superpose à la courbe SN. Le mécanisme conduisant à l'excitabilité dans ce cas n'est pas liée à la bifurcation homoclinique mais à un point de selle sur un cycle limite. Comme de telles régions de superposition existent tant pour les valeurs positives que négatives du désaccord en fréquence, on peut observer de telles excitabilités dans les deux cas. Ceci a été démontré expérimentalement [160].

La figure 7.6 regarde plus spécifiquement les dynamiques stables observées en dehors de la région de locking, avec une attention encore plus particulière aux régions de pulsations auto-entretenues se trouvant proches de la bifurcation SN. Ce diagramme a été obtenu par intégration directe des équations dynamiques du laser, et non pas comme pour la figure 7.5 par une méthode de continuation. Ce diagramme est en accord avec celui obtenu par continuation, mais montre également de nouvelles régions de dynamiques qualitativement différentes et notées C^1, C^2, C^- et CX. Ces régions de l'espace des paramètres ne sont pas délimitées par de nouvelles bifurcations, mais correspondent à des modifications de la forme d'onde dans la dynamique d'intensité émise. Pour des faibles valeurs de puissance injectée et pour des valeurs positives et grandes du désaccord en fréquence, le laser présente une dynamique de type LC c'est-à-dire une intensité fluctuant périodiquement dans le temps de façon auto-entretenue. Lorsque le désaccord en fréquence diminue vers des valeurs négatives, en suivant la ligne A dans la figure 7.6, le laser entre dans un régime dynamique C^1 où la trace temporelle de l'intensité émise correspond à la figure 7.7-1. Cette dynamique ressemble à l'émission d'impulsions d'un système excitable mais, contrairement à l'excitabilité, l'émission d'impulsions est déterministe et ne nécessite pas de perturbation extérieure ou de bruit. Comme mentionné précédemment, lorsque le système approche la bifurcation SN vers la région d'injection locking, une dynamique véritablement excitable peut être également observée correspondant à un mécanisme de bifurcation de point de selle sur un cycle limite. Dans notre cas, la dynamique de la région C^1 est la génération spontanée et entretenue d'impulsions qui ont la forme d'impulsions excitables mais dans un système déterministe. Le mécanisme de bifurcation associé a été élucidé et correspond à ce que l'on appelle un *bottleneck* [161], comme illustré à la figure 7.8a. Lorsque le système est dans la région de locking, la trajectoire est attirée vers un point fixe de type *nœud* (carré plein) qui est stable et correspond à une solution stationnaire de blocage par injection. Cette trajectoire correspond à un mouvement large dans l'espace de phase le long de la trajectoire répulsive induite par le point de selle (carré vide). Lorsque le système franchit la bifurcation SN et entre dans la région C^1, la trajectoire du système devient un cycle limite car le point fixe nœud est devenu instable. Il est intéressant de remarquer cependant que la trajectoire reste influencée par la trajectoire répulsive du point de selle ou plutôt de son fantôme car le point de selle a disparu à la bifurcation SN (de même que le nœud). Ce phénomène par lequel la trajectoire d'un système reste influencée par la trajectoire issue d'un point de selle fantôme est appelé *bottleneck*. La mesure du temps caractéristique entre deux impulsions émises en fonction du désaccord en fréquence, donc en fonction de la distance à la bifurcation SN le long de la flèche A, est tracée dans la figure 7.8b et présente une loi de type inverse carré caractéristique de ce phénomène de *bottleneck*. La figure 7.7 présente d'autres formes d'onde caractéristiques des différentes régions dynamiques CX et C^-.

Nous avons complété notre étude de ces dynamiques pulsées auto-entretenues dans deux directions:

- En ajoutant du bruit d'émission spontanée dans les équations dynamiques du laser avec injection optique, nous avons observé la dispersion du temps entre deux impulsions émises. Ce temps devient une variable aléatoire avec une distribution gaussienne. L'écart type et la moyenne de cette distribution sont fortement dépendants du désaccord en fréquence qui, même dans le cas déterministe, modifie le temps entre les impulsions émises. Les résultats théoriques sont en très bon accord avec des observations expérimentales.

- Une application intéressante de ce régime dynamique auto-pulsée (dans la région C^1) est par exemple la régénération tout optique de signal: si un signal atténué et déformé est utilisé comme signal émis par un laser maître, et si l'amplitude de ce signal est telle que le laser esclave passe de la région C^1 à la région d'injection locking, alors l'mission d'mpulsions dans la région C^1 et l'absence d'impulsions dans la région dinjection locking permettent de regénérer le signal pratiquement sans erreur. Un exemple a été démontré de regénération sans erreur à un débit binaire de 1 Gb/s.

7.4 Basculement de gain intrinsèque dans un QD EEL émettant simultanément dans les états fondamental et excité (laser à deux couleurs)

Comme mentionné précédemment, le fait que le nombre de boîtes quantiques soit limité, et que le spectre d'énergie des boîtes quantiques soit discret, conduit à une saturation de l'occupation de l'état fondamental et ce même à des courants d'injection relativement faibles. Dans de telles situations l'état excité peut être occupé et conduire à l'émission laser simultanée dans deux états radiatifs de fréquences différentes. Dans les lasers QD, les porteurs injectés atteignent les états fondamental (GS) et excité (ES) à des taux déterminés par les temps de relaxation et de capture, respectivement. Ces temps sont exprimés par le rapport entre des valeurs fixes τ_o et τ_c qui correspondent à des états non occupés et un terme d'exclusion de Pauli du type $(1 - f_j)$ (j=ES ou GS) qui rend donc les temps de relaxation et capture dépendants de l'occupation de l'état en question. Dès lors même si l'injection optique n'affecte que l'état fondamental principalement (compte tenu de la différence très grande en fréquence, de l'ordre du THz, entre les états GS et ES), la modulation éventuelle de la population dans l'état GS peut se répercuter sur la population occupée dans l'état ES suite à des modifications de ces constantes de temps.

Un exemple est illustré a la figure 7.9. L'intensité émise par l'état fondamental (GS) évolue périodiquement de façon auto-entretenue. Nous savons par la discussion précédente que lorsqu'un laser est injecté optiquement avec des paramètres ne correspondant pas à la région de blocage par injection, ce laser en effet peut présenter la dynamique caractéristique d'un cycle limite. Cependant l'intensité émise dans le mode ES évolue elle aussi périodiquement sous forme d'impulsions très courtes, de durée ps, et de très forte amplitude (10 x l'intensit du mode GS). La figure 7.9 présente également en b) l'évolution des populations occupant les états GS et ES et la couche humide WL, et en c) l'évolution des constantes de temps de relaxation et de capture. La dynamique est dominée par les modulations en antiphase de l'intensité et de la population de l'état GS. Ces modulations causent des modulations du temps de relaxation τ_o, et donc aussi de la population occupant l'état excité. Ces oscillations dans l'état ES modulent alors le temps de capture τ_c, et donc aussi l'occupation de la couche humide. Lorsque la population occupant l'état GS atteint la valeur de seuil (th = threshold), l'état excité ES émet une impulsion très courte, selon un mécanisme correspondant à un basculement de gain. La fréquence de ces impulsions courtes dans le mode ES est de l'ordre de quelques GHz et augmente linéairement avec le désaccord en fréquence.

7.5 Conclusions

En résumé ce travail de thèse a permis de mettre en évidence plusieurs dynamiques nouvelles dans des lasers à boîtes quantiques. Premièrement, il a été démontré expérimentalement qu'un laser QD VCSEL peut présenter un basculement de son état de polarisation dans un intervalle important de courant d'injection, et que cette compétition de polarisation est accompagnée d'une dynamique aléatoire de saut de mode. Cette dynamique bien que semblable à celle observée dans les lasers VCSELs à puits quantiques est différente également en de nombreux points: 1/ elle implique des états polarisés elliptiquement et non orthogonaux, 2/ le temps de séjour moyen dans un mode de polarisation décroît avec l'augmentation du courant d'injection, 3/ la dynamique de saut de mode est observée dans un intervalle très grand de courants. Dans un deuxième temps nous avons étudié théoriquement le système constitué d'un laser à boîtes quantiques avec une injection optique. Nous avons mis en évidence deux dynamiques originales: 1/ des régimes dynamiques pulsés auto-entretenus, expliqués par une bifurcation de type *bottleneck* où la trajectoire du système reste influencée par la trajectoire instable issue d'un point de selle. Ces régimes dynamiques ressemblent à une dynamique excitable bien que les impulsions soient générées spontanément sans la nécessité d'une perturbation ou de l'ajout de bruit. 2/ Lorsque le laser émet spontanément dans l'état fondamental et l'état excité, les modulations d'intensité du mode fondamental peuvent conduire à des fluctuations d'intensité également dans le mode excité. L'intensité émise par le mode excité présente alors des séquences d'impulsions très courtes (ps) à des fréquences de plusieurs GHz.

Bibliography

[1] Z. Alferov. Double heterostructure lasers: Early days and future perspectives. *IEEE J. Select. Top. Quantum Electron*, 6(6):pp. 832–840, 2000. [cited at p. 5]

[2] M. Toda. Material selection for double heterojunction lasers: A higher bandgap does not necessarily mean lower refractive index. *IEEE J. Quantum Electron.*, 23(5):pp. 483–486, 1987. [cited at p. 6]

[3] L.A. Coldren and S.W. Corizone. *Diode lasers and photonic integrated circuits.* Wiley-Interscience, New York, 1995. [cited at p. 7]

[4] P. Harrison. *Quantum Wells, Wires and Dots: Theoretical and Computational Physics of Semiconductor Nanostructures, Second Edition.* Wiley-Interscience, 2006. [cited at p. 7, 8]

[5] D. Bimberg. Quantum dot based nanophotonics and nanoelectronics. *Electron. Lett.*, 44(3), 2008. [cited at p. 9, 10]

[6] M. Asada, Y. Miyamoto, and Y. Suematsu. Gain and the threshold of three-dimensional quantum-box lasers. *IEEE J. of Quantum Electron.*, 22(9):pp. 1915–1921, 1986. [cited at p. 9, 12]

[7] A. Persano, A. Cola, A. Taurino, M. Catalano, M. Lomascolo, A. Convertino, G. Leo, L. Cerri, A. Vasanelli, and L. Vasanelli. Electronic structure of double stacked InAs/GaAs quantum dots: Experiment and theory. *J. App. Phys.*, 102(094314), 2007. [cited at p. 10, 20]

[8] M. Sugawara, K. Mukai, Y. Nakata, H. Ishikawa, and A. Sakamoto. Effect of homogeneous broadening of optical gain on lasing spectra in self-assembled $In_xGa_{1-x}As/GaAs$ quantum dot lasers. *Phys. Rev. B*, 61(11):pp. 7595–7603, 2000. [cited at p. 9, 10, 11]

[9] H. Saito, K. Nishi, and S. Sugou. Shape transition of InAs quantum dots by growth at high temperature. *App. Phys. Lett.*, 74(9):pp. 1224–1226, 1999. [cited at p. 10]

[10] S.S. Mikhrin, A.E. Zhukov, A.R. Kovsh, N.A. Maleev, V.M. Ustinov, Yu.M. Shernyakov, I.P. Soshnikov, D.A. Livshits, I.S. Tarasov, D.A. Bedarev, B.V. Volovik, M.V. Maximov, A.F. Tsatsulnikov, N.N. Ledentsov, P.S. Kopev, D. Bimberg, and Zh.I. Alferov. 0.94 μm diode lasers based on Stranski-Krastanow and sub-monolayer quantum dots. *Semicond. Sci. Technol.*, 15:pp. 1061–1064, 2000. [cited at p. 10, 37]

[11] Z. Xu, K. Leosson, D. Birkedal, V. Lyssenko, J.M. Hvam, and J. Sadowski. InGaAs-GaAs quantum-dot-quantum-well heterostructure formed by submonolayer deposition. *Nanotechnology*, 14:pp. 1259–1261, 2003. [cited at p. 10]

[12] V.M. Ustinov. Quantum dot structures: Fabrication technology and control of parameters. *Semiconductors*, 38(8):pp. 923–930, 2004. [cited at p. 10]

[13] N.N. Ledentsov, D. Bimberg, F. Hopfer, A. Mutig, V.A. Shchukin, A.V. Savelev, G. Fiol, E. Stock, H. Eisele, M. Dahne, D. Gerthsen, U. Fischer, D. Litvinov, A. Rosenauer, S.S. Mikhrin, A.R. Kovsh, N.D. Zakharov, and P. Werner. Submonolayer quantum dots for high speed surface emitting lasers. *Nanoscale Res Lett.*, 2:pp. 417–429, 2007. [cited at p. 10]

[14] P. Borri, S. Schneider, W. Langbein, U. Woggon, A.E. Zhukov, V.M. Ustinov, N.N. Ledentsov, Zh.I. Alferov, D. Ouyang, and D. Bimberg. Ultrafast carrier dynamics and dephasing in InAs quantum-dot amplifiers emitting near 1.3-μm-wavelength at room temperature. *App. Phys. Lett.*, 79(16):pp. 2633–2635, 2001. [cited at p. 10, 11]

[15] N. Kirstaedter, O.G. Schmidt, N.N. Ledentsov, D. Bimberg, V.M. Ustinov, A.Yu. Egorov, A.E. Zhukov, M.V. Maximov, P.S. Kopev, and Zh.I. Alferov. Gain and differential gain of single layer InAs/GaAs quantum dot injection lasers. *App. Phys. Lett.*, 69(9):pp. 1226–1228, 1996. [cited at p. 11]

[16] A. Salhi, G. Rain, L. Fortunato, V. Tasco, L. Martiradonna, M.T. Todaro, M. De Giorgi, R. Cingolani, A. Passaseo, E. Luna, A. Trampert, and M. De Vittorio. Linear increase of the modal gain in 1.3 μm InAs/GaAs quantum dot lasers containing up to seven-stacked QD layers. *Nanotechnology*, 19(275401):pp. 1–4, 2008. [cited at p. 11, 13]

[17] P. Caroff, C. Paranthoen, C. Platz, O. Dehaese, H. Folliot, N. Bertru, C. Labb, R. Piron, E. Homeyer, A. Le Corre, and S. Loualiche. High-gain and low-threshold InAs quantum-dot lasers on InP. *App. Phys. Lett.*, 87(243107), 2005. [cited at p. 11]

[18] D. Bimberg, M. Grundmann, and N.N. Ledentsov. *Quantum Dot Heterostructures.* Wiley, 1998. [cited at p. 12]

[19] I.N. Kaiander, F. Hopfer, T. Kettler, U.W. Pohl, and D. Bimberg. Alternative precursor growth of quantum dot-based VCSELs and edge emitters for near infrared wavelengths. *J. Cryst. Growth*, 272:pp. 154–160, 2004. [cited at p. 13, 21, 23, 39]

[20] Y. Arakawa and H. Sakaki. Multidimensional quantum well laser and temperature dependence of its threshold current. *App. Phys. Lett.*, 40(11):pp. 939–941, 1982. [cited at p. 13]

[21] G. Park, O.B. Shchekin, D.L. Huffaker, and D.G. Deppe. Lasing from InGaAs/GaAs quantum dots with extended wavelength and well-defined harmonic-oscillator energy levels. *App. Phys. Lett.*, 73(23):pp. 3351–3354, 1998. [cited at p. 13]

[22] K. Kim, T.B. Norris, S. Ghosh, J. Singh, and P. Bhattacharya. Level degeneracy and temperature-dependent carrier distributions in self-organized quantum dots. *App. Phys. Lett.*, 82(12):pp. 1959–1961, 2003. [cited at p. 13]

[23] H. Jiang and J. Singh. Strain distribution and electronic spectra of InAs/GaAs self-assembled dots: An eight-band study. *Phys. Rev. B*, 56(8):pp. 4696–4701, 1997. [cited at p. 13]

[24] O. Stier, A. Schliw, R. Heitz, M. Grundmann, and D. Bimberg. Stability of biexcitons in pyramidal InAs/GaAs quantum dots. *Phys. stat. sol. (b)*, 224(1):pp. 115–118, 2001. [cited at p. 13]

[25] P.N. Brunkov, A.R. Kovsh, V.M. Ustinov, Yu.G. Musikhin, N.N. Ledentsov, S.G. Konnikov, A. Polimeni, A. Patane, P.C. Main, L. Eaves, and C.M.A. Kapteyn. Emission of electrons from the ground and first excited states of self-organized InAs/GaAs quantum dot structures. *J. Electron. Mat.*, 28(5):pp. 486–490, 1999. [cited at p. 14]

[26] M. Ediger, G. Bester, B.D. Gerardot, A. Badolato, P.M. Petroff, K. Karrai, A. Zunger, and R.J. Warburton. Fine structure of negatively and positively charged excitons in semiconductor quantum dots: Electron-hole asymmetry. *Phys. Rev. Lett.*, 98(036808), 2007. [cited at p. 13]

[27] C. Delerue and M. Lannoo. *Nanostructures: Theory and Modelling, NanoScience and Technology.* Springer-Verlag, Berlin, 2004. [cited at p. 13]

[28] S. Sasaki, D.G. Austing, and S. Taruch. Spin states in circular and elliptical quantum dots. *Physica B*, 256–258:pp. 157–160, 1998. [cited at p. 13]

[29] J. Urayama, T.B. Norris, H. Jiang, J. Singh, and P. Bhattacharya. Temperature-dependent carrier dynamics in self-assembled InGaAs quantum dots. *App. Phys. Lett.*, 80(12):pp. 2162–2164, 2002. [cited at p. 13]

[30] M. Gioannini, A. Sevega, and I. Montrosset. Simulations of differential gain and linewidth enhancement factor of quantum dot semiconductor lasers. *Opt. and Quantum Electron.*, 38(4–6):pp. 381–394, 2006. [cited at p. 13, 72]

[31] A. Markus, J.X. Chen, C. Paranthoen, A. Fiore, C. Platz, and O. Gauthier-Lafaye. Simultaneous two-state lasing in quantum-dot lasers. *Appl. Phys. Lett.*, 82(12):pp. 1818–1820, 2003. [cited at p. 13, 25, 71, 72, 74, 98, 102, 126]

[32] R.P. Prasankumar, R.S. Attaluri, R.D. Averitt1, J. Urayama, N. Weisse-Bernstein, P. Rotella, A.D. Stintz, S. Krishna, and A.J. Taylor. Ultrafast carrier dynamics in an InAs/InGaAs quantum dots-in-a-well heterostructure. *Opt. Express*, 16(2):pp. 1165–1173, 2008. [cited at p. 14]

[33] H. Benisty, C.M. Sotomayor-Torrs, and C. Weisbuch. Intrinsic mechanism for the poor luminescence properties of quantum-box systems. *Phys. Rev. B*, 44(19):pp. 10945–10948, 1991. [cited at p. 14]

[34] K. Ggndogdu, K.C. Hall, T.F. Boggess, D.G. Deppe, and O.B. Shchekin. Ultrafast electron capture into p-modulation-doped quantum dots. *App. Phys. Lett.*, 85(20):pp. 4570–4572, 2004. [cited at p. 14, 15, 102]

[35] B. Ohnesorge, M. Albrecht, J. Oshinowo, A. Forchel, and Y. Arakawa. Rapid carrier relaxation in self-assembled $In_xGa_{1-x}As$/GaAs quantum dots. *Phys. Rev. B*, 54(16):pp. 11532–11538, 1996. [cited at p. 14, 15]

[36] D. Morris, N. Perret, and S. Fafard. Carrier energy relaxation by means of auger processes in InAs/GaAs self-assembled quantum dots. *App. Phys. Lett.*, 75(23):pp. 3593–3595, 1999. [cited at p. 14]

[37] T. Inoshita and H. Sakaki. Electron relaxation in a quantum dot: Significance of multiphonon processes. *Phys. Rev. B*, 46(11):pp. 7260–7263, 1992. [cited at p. 14]

[38] P.C. Sercel. Multiphonon-assisted tunneling through deep levels: A rapid energy-relaxation mechanism in non-ideal quantum-dot heterostructures. *Phys. Rev. B*, 51(20):pp. 14532–14541, 1995. [cited at p. 14]

[39] T. Piwonski, T. ODriscoll, J. Houlihan, G. Huyet, R.J. Manning, and A.V. Uskov. Carrier capture dynamics of InAs/GaAs quantum dots. *App. Phys. Lett.*, 90(122108), 2007. [cited at p. 15]

[40] T. Erneux, E.A. Viktorov, P. Mandel, T. Piwonski, G. Huyet, and J. Houlihan. The fast recovery dynamics of a quantum dot semiconductor optical amplifier. *App. Phys. Lett.*, 94(113501), 2009. [cited at p. 15]

[41] V. Uskov, E.P. OReilly, R.J. Manning, R.P. Webb, D. Cotter, M. Laemmlin, N.N. Ledentsov, and D. Bimberg. On ultrafast optical switching based on quantum-dot semiconductor optical amplifiers in nonlinear interferometers. *IEEE Phot. Tech. Lett.*, 16(5):pp. 1265–1267, 2004. [cited at p. 15]

[42] N. Kirstaedter, N.N. Ledentsov, M. Grundmann, D. Bimberg, V.M. Ustinov, S.S. Ruvimov, M.V. Maximov, P.S. Kop'ev, Zh.I. Alferov, U. Richter, P. Werner, U. Gosele, and J. Heydenreich. Low threshold, large T_0 injection laser emission from (InGa)As quantum dots. *Electron. Lett.*, 30(17):pp. 1416–1417, 1994. [cited at p. 15, 21]

[43] O.B. Shchekin, J. Ahn, and D.G. Deppe. High temperature performance of self-organised quantum dot laser with stacked p-doped active region. *Electron. Lett.*, 38(14):pp. 712–713, 2002. [cited at p. 15, 21]

[44] I.I. Novikov, N.Yu. Gordeev, L.Ya. Karachinski, M.V. Maksimov, Yu.M. Shernyakov, A.R. Kovsh, I.L. Krestnikov, A.V. Kozhukhov, S.S. Mikhrin, and N.N. Ledentsov. Effect of p-doping of the active region on the temperature stability of InAs/GaAs QD lasers. *Semiconductors*, 39(4):pp. 477–480, 2005. [cited at p. 15, 21, 22]

[45] L.V. Asryan and R.A. Suris. Inhomogeneous line broadening and the threshold current density of a semiconductor quantum dot laser. *Semicond. Sci. Technol.*, 11:pp. 554–567, 1996. [cited at p. 15]

[46] C. Henry. Theory of the linewidth of semiconductor lasers. *IEEE J. Quantum Electron.*, QE-18(2):pp. 259–264, 1982. [cited at p. 16, 17, 18]

[47] G.P. Agrawal and N.A. Olsson. Self-phase modulations and spectral broadening of optical pulses in semiconductor laser amplifiers. *IEEE J. Quantum Electron.*, 25(11):pp. 2297–2306, 1989. [cited at p. 16]

[48] G.P. Agrawal. Intensity dependence of the linewidth enhancement factor and its implications for semiconductor lasers. *IEEE Phot. Tech. Lett.*, 1(8):pp. 212–214, 1989. [cited at p. 16]

[49] J.R. Marciante and G.P. Agrawal. Spatio-temporal characteristics of filamentation in broad-area semiconductor lasers: Experimental results. *IEEE Phot. Tech. Lett.*, 10(1):pp. 54–56, 1998. [cited at p. 16]

[50] S. Wieczorek, B. Krauskopf, T.B. Simpson, and D. Lenstra. The dynamical complexity of optically injected semiconductor lasers. *Phys. Rep.*, 416(1-2):pp. 1–128, 2005. [cited at p. 16, 24, 61, 62, 66, 69, 97, 123]

[51] G. Giuliani. Linewidth enhancement factor in semiconductor lasers. Technical report, COST 288 WG2, 2004. [cited at p. 18]

[52] Z. Xu, D. Birkedal, M. Juhl, and J.M. Hvam. Submonolayer InGaAs/GaAs quantum-dot lasers with high modal gain and zero-linewidth enhancement factor. *App. Phys. Lett.*, 85(15):pp. 3259–3261, 2004. [cited at p. 18, 20]

[53] T.C. Newell, D.J. Bossert, A. Stintz, B. Fuchs, K.J. Malloy, and L.F. Lester. Gain and linewidth enhancement factor in InAs quantum-dot laser diodes. *IEEE Phot. Tech. Lett.*, 11(12):pp. 1527–1529, 1999. [cited at p. 18]

[54] P.K. Kondratko, S.-L. Chuang, G. Walter, T. Chung, and N. Holonyak. Observations of near-zero linewidth enhancement factor in a quantum-well coupled quantum-dot laser. *App. Phys. Lett.*, 83(4818), 2003. [cited at p. 18]

[55] D. Bimberg, N. Kirstaedter, N.N. Ledentsov, Zh.I. Alferov, P.S. Kop'ev, and V.M. Ustinov. InGaAs-GaAs quantum-dot lasers. *IEEE J. Sel. Top. Quantum Electron.*, 3(2):pp. 196–205, 1997. [cited at p. 18]

[56] A.A. Ukhanov, A. Stintz, P.G. Eliseev, and K.J. Malloy. Comparison of the carrier induced refractive index, gain, and linewidth enhancement factor in quantum dot and quantum well lasers. *App. Phys. Lett.*, 84(7):pp. 1058–1060, 2004. [cited at p. 18, 24, 123]

[57] A. Markus, J.X. Chen, O. Gauthier-Lafaye, J.-G. Provost, C. Paranthoen, and A. Fiore. Impact of intraband relaxation on the performance of a quantum-dot laser. *IEEE J. Select. Top. Quantum Electron.*, 9(5):pp. 1308–1314, 2003. [cited at p. 18, 24, 72, 124]

[58] B. Dagens, A. Markus, J.X. Chen, J.-G. Provost, D. Make, O. Le Gouezigou, J. Landreau, A. Fiore, and B. Thedrez. Giant linewidth enhancement factor and purely frequency modulated emission from quantum dot laser. *Electron. Let.*, 41(6), 2005. [cited at p. 18, 25, 126]

[59] S. Melnik, G. Huyet, and V.A. Uskov. The linewidth enhancement factor α of quantum dot semiconductor lasers. *Opt. Express*, 14(7):pp. 2950–2955, 2006. [cited at p. 18]

[60] I. Hayashi, M.B. Panish, P.W. Foy, and S. Sumski. Junction lasers which operate continuously at room temperature. *App. Phys. Lett.*, 17(3):pp. 109–111, 1970. [cited at p. 18]

[61] R. Dingle, W. Wiegmann, and C.H. Henry. Quantum states of confined carriers in very thin $\mathrm{Al}_x\mathrm{Ga}_{1-x}\mathrm{As}$–GaAs-$\mathrm{Al}_x\mathrm{Ga}_{1-x}\mathrm{As}$ heterostructures. *Phys. Rev. Lett.*, 33(14):pp. 827–830, 1974. [cited at p. 18]

[62] H. Soda, K. Iga, C. Kitahara, and Y. Suematsu. GaInAsP/InP surface emitting injection laser. *Jpn. J. Appl. Phys.*, 18:pp. 2329–2330, 1979. [cited at p. 18]

[63] K. Iga, S. Ishikawa, C. Ohkouchi, and T. Nishimura. Room-temperature pulsed oscillation of GaAlAs/GaAs surface emitting lasers. *App. Phys. Lett.*, 45:pp. 348–350, 1984. [cited at p. 18]

[64] F. Koyama, S. Kinoshita, and K. Iga. Room temperature CW operation of GaAs vertical cavity surface emitting laser. *IEICE TRANSACTIONS*, E71-E(11):pp. 1089–1090, 1988. [cited at p. 18]

[65] Y.H. Lee, J.L. Jewell, A. Scherer, S.L. McCall, J.P. Harbison, and L.T. Florez. Room-temperature continuous-wave vertical-cavity single-quantum-well microlaser diodes. *Electron. Lett.*, 25(20):pp. 1377–1378, 1989. [cited at p. 18]

[66] J.L. Jewell, A. Scherer, S.L. McCall, Y.H. Lee, S. Walker, J.P. Harbison, and L.T. Florez. Low-threshold electrically pumped vertical-cavity surface-emitting microlasers. *Electron. Lett.*, 25(17):pp. 1123–1124, 1989. [cited at p. 18, 19]

[67] C.J. Chang-Hasnain, J.P. Harbison, G. Hasnain, A.C. Von Lehmen, L.T. Florez, and N.G. Stoffel. Dynamic, polarization, and transverse mode characteristics of vertical cavity surface emitting lasers. *IEEE J. of Quantum Electron.*, 27(6):pp. 1402–1409, 1991. [cited at p. 19, 27, 28]

[68] C.J. Chang-Hasnain, M. Orenstein, A. Von Lehmen, L.T. Florez, J.P. Harbison, and N.G. Stoffel. Transverse mode characteristics of vertical cavity surface-emitting lasers. *App. Phys. Lett.*, 57(3):pp. 218–220, 1990. [cited at p. 19]

[69] C.H. Chong and J. Sarma. Lasing mode selection in vertical-cavity surface-emitting laser diodes. *IEEE Phot. Tech. Lett.*, 5(7):pp. 761–764, 1993. [cited at p. 19]

[70] A. Valle, J. Sarma, and K.A. Shore. Spatial hole burning effects on the dynamics of vertical cavity surface-emitting laser diodes. *IEEE J.. of Quantum Electron.*, 31(8):pp. 1423–1431, 1995. [cited at p. 19]

[71] S.W. Corzine, R.H. Yan, and L.A. Coldren. *Optical gain in III-V bulk and quantum well semiconductors.* In Quantum Well Lasers. Academic Press, Boston, 1993. [cited at p. 19, 27]

[72] A.K. Jansen van Doorn, M.P. van Exter, and J.P. Woerdman. Tailoring the birefringence in a vertical-cavity semiconductor laser. *App. Phys. Lett.*, 69(24):pp. 3635–3637, 1996. [cited at p. 19]

[73] K. Panajotov, J. Danckaert, G. Verschaffelt, M. Peeters, B. Nagler, J. Albert, B. Ryvkin, H. Thienpont, and I. Veretennicoff. Polarization behavior of vertical-cavity surface-emitting lasers: Experiments, models and applications. *AIP Conf. Proc.*, 560:pp. 403–417, 2001. [cited at p. 19, 27, 29]

[74] F.P.J. de Groote. *Multi-Excitons in GaAs/AlGaAs Quantum Dot Arrays.* PhD thesis, Technische Universiteit Eindhoven, 2003. [cited at p. 20]

[75] F. Hopfer, A. Mutig, M. Kuntz, G. Fiol, D. Bimberg, N.N. Ledentsov, V.A. Shchukin, S.S. Mikhrin, D.L. Livshits, I.L. Krestnikov, A.R. Kovsh, N.D. Zakharov, and P. Werner. Single-mode submonolayer quantum-dot vertical-cavity surface-emitting lasers with high modulation bandwidth. *App. Phys. Lett.*, 89(141106), 2006. [cited at p. 20, 39]

[76] M.V. Maximov, Yu.M. Shernyakov, A.F. Tsatsulnikov, A.V. Lunev, A.V. Sakharov, V.M. Ustinov, A.Yu. Egorov, A.E. Zhukov, A.R. Kovsh, P.S. Kopev, L.V. Asryan, Zh.I. Alferov, N.N. Ledentsov, D. Bimberg, A.O. Kosogov, and P. Werner. High-power continuous-wave operation of a InGaAs/AlGaAs quantum dot laser. *J. App. Phys.*, 83(10):pp. 5561–5563, 1998. [cited at p. 20]

[77] K. Kamath, P. Bhattacharya, T. Sosnowski, T. Norris, and J. Phillips. Room-temperature operation of $In_{0.4}Ga_{0.6}As$/GaAs self-organised quantum dot lasers. *Electron. Lett.*, 32(15):pp. 1374–1375, 1996. [cited at p. 21]

[78] R. Mirin, A. Gossard, and J. Bowers. Room temperature lasing from InGaAs quantum dots. *Electron. Lett.*, 32(18), 1996. [cited at p. 21]

[79] P. Gyoungwon, O.B. Shchekin, D.L. Huffaker, and D.G. Deppe. Low-threshold oxide-confined 1.3-μm quantum-dot laser. *Electron. Lett.*, 12(3):pp. 230–232, 2000. [cited at p. 21]

[80] I.N. Kaiander, R.L. Sellin, T. Kettler, N.N. Ledentsov, D. Bimberg, N.D. Zakharov, and P. Werner. 1.24 μm InGaAs/GaAs quantum dot laser grown by metalorganic chemical vapor deposition using tertiarybutylarsine. *App. Phys. Lett.*, 84(16):pp. 2992–2994, 2004. [cited at p. 21]

[81] V.M. Ustinov, N.A. Maleev, A.E. Zhukov, A.R. Kovsh, A.Yu. Egorov, A.V. Lunev, B.V. Volovik, I.L. Krestnikov, Yu.G. Musikhin, N.A. Bert, P.S. Kopev, Zh.I. Alferov, N.N. Ledentsov, and D. Bimberg. InAs/InGaAs quantum dot structures on GaAs substrates emitting at 1.3 μm. *App. Phys. Lett.*, 74(19):pp. 2815–2817, 1999. [cited at p. 21]

[82] J. Tatebayashi, M. Nishioka, and Y. Arakawa. Luminescence in excess of 1.5 μm at room-temperature of InAs quantum dots capped by a thin InGaAs strain-reducing layer. *J. Cryst. Growth*, 237-239:pp. 1296–1300, 2002. [cited at p. 21]

[83] L.Ya. Karachinsky, T. Kettler, I.I. Novikov, Yu.M. Shernyakov, N.Yu. Gordeev, M.V. Maximov, N.V. Kryzhanovskaya, A.E. Zhukov, E.S. Semenova, A.P. Vasilev, V.M. Ustinov, G. Fiol, M. Kuntz, A. Lochmann, O. Schulz, L. Reissmann, K. Posilovic, A.R. Kovsh, S.S. Mikhrin, V.A. Shchukin, N.N. Ledentsov, and D. Bimberg. Metamorphic 1.5 μm-range quantum dot lasers on a GaAs substrate. *Semicond. Sci. Technol*, 21:pp. 691–696, 2006. [cited at p. 21]

[84] H.Y. Liu, M.J. Steer, T.J. Badcock, D.J. Mowbray, M.S. Skolnick, F. Suarez, J.S. Ng, M. Hopkinson, and J.P.R. David. Room-temperature 1.6 μm light emission from InAs/GaAs quantum dots with a thin GaAsSb cap layer. *J. App. Phys.*, 99(046104), 2006. [cited at p. 22]

[85] H. Saito, K. Nishi, I. Ogura, S. Sugou, and Y. Sugimoto. Room-temperature lasing operation of a quantum-dot vertical-cavity surface-emitting laser. *App. Phys. Lett.*, 69(21):pp. 3140–3242, 1996. [cited at p. 22]

[86] Z. Zou, D.L. Huffaker, S. Csutak, and D.G. Deppe. Ground state lasing from a quantum-dot oxide-confined vertical-cavity surface-emitting laser. *App. Phys. Lett.*, 75(1):pp. 22–24, 1999. [cited at p. 23]

[87] U.W. Pohl, K. Potschke, I. Kaiander, J.-T. Zettler, and D. Bimberg. Real-time control of quantum dot laser growth using reflectance anisotropy spectroscopy. *J. Cryst. Growth*, 272:pp. 143–147, 2004. [cited at p. 23, 39]

[88] H. Saito, K. Nishi, S. Sugou, and Y. Sugimoto. Controlling polarization of quantum-dot surface-emitting lasers by using structurally anisotropic self-assembled quantum dots. *Appl. Phys. Lett.*, 71(5):pp. 590–592, 1997. [cited at p. 23, 37, 38]

[89] R. Lang. Injection locking properties of a semiconductor laser. *IEEE J. Quantum Electron.*, 18(6):pp. 976–983, 1982. [cited at p. 24, 61, 69, 97, 123]

[90] M. Sciamanna and K. Panajotov. Route to polarization switching induced by optical injection in vertical-cavity surface-emitting lasers. *Phys. Rev. A*, 73(023811), 2006. [cited at p. 24, 25, 61, 69, 97, 123]

[91] T.B. Simpson, J.M. Liu, and A. Gavrielides. Small-signal analysis of modulation characteristics in a semiconductor laser subject to strong optical injection. *IEEE J. Quantum Electron.*, 32(8):pp. 1456–1468, 1996. [cited at p. 24, 97, 123]

[92] T.B. Simpson, J.M. Liu, and A. Gavrielides. Bandwidth enhancement and broadband noise reduction in injection-locked semiconductor lasers. *IEEE Phot. Tech. Lett.*, 7(7):pp. 709–711, 1995. [cited at p. 24, 97, 123]

[93] E.K. Lau, L.J. Wong, X. Zhao, Y.-K. Chen, C.J. Chang-Hasnain, and M.C. Wu. Bandwidth enhancement by master modulation of optical injection-locked lasers. *J. Lightwave Technol.*, 26(15):pp. 2584–2593, 2008. [cited at p. 24, 123]

[94] E. Malic, M.J.P. Bormann, P. Hovel, M. Kuntz, D. Bimberg, A. Knorr, and E. Scholl. Coulomb damped relaxation oscillations in semiconductor quantum dot lasers. *IEEE J. Select. Top. Quantum Electron*, 13(5):pp. 1242–1248, 2004. [cited at p. 24, 123]

[95] D. Goulding, S.P. Hegarty, O. Rasskazov, S. Mielnik, M. Hartnett, G. Greene, J.G. McInerney, D. Rachinskii, and G. Huye. Excitability in a quantum dot semiconductor laser with optical injection. *Phys. Rev. Lett.*, 98(153903), 2007. [cited at p. 24, 63, 66, 67, 68, 70, 72, 74, 75, 77, 98, 124, 125, 134]

[96] M.C. Eguia and G.B. Mindlin. Semiconductor laser with optical feedback: From excitable to deterministic low-frequency fluctuations. *Phys. Rev. E*, 60(2):pp. 1551–1557, 1999. [cited at p. 24, 66, 124]

[97] A.M. Yacomotti, M.C. Eguia, J. Aliaga, O.E. Martinez, G.B. Mindlin, and A. Lipsich. Interspike time distribution in noise driven excitable systems. *Phys. Rev. Lett.*, 83(2):pp. 292–295, 1998. [cited at p. 24, 66, 124]

[98] J.L.A. Dubbeldam, B. Krauskopf, and D. Lenstra. Excitability and coherence resonance in lasers with saturable absorber. *Phys. Rev. E*, 60(6):pp. 6580–6588, 1999. [cited at p. 24, 66, 124]

[99] C. Tong, D. Xu, and S.F. Yoon. Carrier relaxation and modulation response of 1.3 μm InAsGaAs quantum dot lasers. *J. Lightwave Technol.*, 27(23):pp. 5442–5450, 2009. [cited at p. 24, 72, 124]

[100] V.V. Lysak, A.V. Shulika, and I.A. Sukhoivanov. A five-level time-domain model for quantum dot lasers: influence of carrier capture and escape processes on dynamic and static characteristic. *Proc. of LFNM, 10.1109/LFNM.2001.930206*, pages pp. 64–68, 2001. [cited at p. 24, 72, 124]

[101] M. Nizette, M. Sciamanna, I. Gatare, H. Thienpont, and K. Panajotov. Dynamics of vertical-cavity surface-emitting lasers with optical injection: a two-mode model approach. *J. Opt. Soc. Am. B*, 26(8):pp. 1603–1613, 2009. [cited at p. 25, 97, 103]

[102] I. Gatare, M. Sciamanna, M. Nizette, and K. Panajotov. Bifurcation to polarization switching and locking in vertical-cavity surface-emitting lasers with optical injection. *Phys. Rev. A*, 76(031803(R)), 2007. [cited at p. 25, 97]

[103] S. Osborne, A. Amann, K. Buckley, G. Ryan, S.P. Hegarty, and G. Huyet. Antiphase dynamics in a multimode semiconductor laser with optical injection. *Phys. Rev. A*, 79(023834), 2009. [cited at p. 25, 97, 98, 112, 126]

[104] G.S. Sokolovskii, M.A. Cataluna, A.G. Deryagin, V.I. Kuchinskii, I.I. Novikov, M.V. Maksimov, A.E. Zhukov, M. Ustinov, W. Sibbett, and E.U. Rafailov. Anomalous dynamic characteristics of semiconductor quantum-dot lasers generating on two quantum states. *Tech. Phys. Lett.*, 33(1):pp. 4–7, 2003. [cited at p. 25, 98, 126]

[105] E.A. Viktorov, P. Mandel, I. ODriscoll, O. Carroll, G. Huyet, J. Houlihan, and Y. Tanguy. Low-frequency fluctuations in two-state quantum dot lasers. *Opt. Lett.*, 31(15):pp. 2302–2304, 2006. [cited at p. 25, 98, 126]

[106] M.A. Cataluna, D.I. Nikitichev, S. Mikroulis, H. Simos, C. Simos, Ch. Mesaritakis, D. Syvridis, I. Krestnikov, D. Livshits, and E.U. Rafailov. Dual-wavelength mode-locked quantum-dot laser, via ground and excited state transitions: experimental and theoretical investigation. *Opt. Exp.*, 18(12):pp. 12832–12838, 2010. [cited at p. 25, 98, 107, 126]

[107] K.D. Choquette, R.P. Schneider, K.L. Lear, and R.E. Leibenguth. Gain-dependent polarization properties of vertical-cavity lasers. *IEEE J. Select. Top. Quantum Electron.*, 1(2):pp. 661–666, 1995. [cited at p. 27, 28, 30]

[108] K.D. Choquette and R.E. Leibenguth. Control of vertical-cavity laser polarization with anisotropic transverse cavity geometries. *IEEE Phot. Tech. Lett.*, 6(1):pp. 40–42, 1994. [cited at p. 27]

[109] B. Ryvkin, K. Panajotov, A. Georgievski, J. Danckaert, M. Peeters, G. Verschaffelt, H. Thienpont, and I. Veretennicoff. Effect of photon-energy-dependent loss and gain mechanisms on polarization switching in vertical-cavity surface-emitting lasers. *J. Opt. Soc. Am. B*, 16(11):pp. 2106–2113, 1999. [cited at p. 27, 28, 29, 30, 32]

[110] K. Panajotov, B. Nagler, G. Verschaffelt, A. Georgievski, H. Thienpont, J. Danckaert, and I. Veretennicoff. Impact of in-plane anisotropic strain on the polarization behavior of vertical-cavity surface-emitting lasers. *App. Phys. Lett.*, 77(11):pp. 1590–1592, 2000. [cited at p. 27, 29, 40]

[111] A.K. Jansen van Doorn, M.P. van Exter, and J.P. Woerdman. Elasto-optic anisotropy and polarization orientation of vertical-cavity surface-emitting semiconductor lasers. *Appl. Phys. Lett.*, 69(8):pp. 1041–1043, 1996. [cited at p. 27, 29, 40]

[112] M.P. Exter, M.B. Willemsen, and J.P. Woerdman. Polarization fluctuations in vertical-cavity semiconductor lasers. *Phys. Rev. A*, 58(5):pp. 4191–4205, 1998. [cited at p. 27]

[113] D. Burak, J.V. Moloney, and R. Binder. Microscopic theory of polarization properties of optically anisotropic vertical-cavity surface-emitting lasers. *Phys. Rev. A*, 61(053809), 2000. [cited at p. 29, 40]

[114] D. Burak, J.V. Moloney, and R. Binder. Macroscopic versus microscopic description of polarization properties of optically anisotropic vertical-cavity surface-emitting lasers. *IEEE J. Quantum Electron.*, 36(8):pp. 956–970, 2000. [cited at p. 29]

[115] M. San Miguel, Q. Feng, and J.V. Moloney. Light-polarization dynamics in surface-emitting semiconductor lasers. *Phys. Rev. A*, 52(2):pp. 1728–1739, 1995. [cited at p. 30, 38]

[116] J. Martin-Regalado, F. Prati, M. San Miguel, and N.B. Abraham. Polarization properties of vertical-cavity surface-emitting lasers. *IEEE J. Quantum Electron.*, 33(5):pp. 765–783, 1997. [cited at p. 30, 32, 33, 34, 35, 39]

[117] M. Travagnin, M. Van Exter, A.K. Jansen Van Doorn, and J.P. Woerdman. Role of optical anisotropies in the polarization properties of surface-emitting semiconductor lasers. *Phys. Rev. A*, 54(2):pp. 1647–1660, 1996. [cited at p. 30, 32]

[118] Y. Okuno. *Polarization control of long-wavelength vertical cavity surface emitting laser (VCSEL) fabricated by orientation-mismatched wafer bonding.* PhD thesis, University of California, Santa Barbara, USA, 2004. [cited at p. 31, 32]

[119] K. D. Choquette, D.A. Richie, and R.E. Leibenguth. Temperature dependence of gain-guided vertical-cavity surface emitting laser polarization. *App. Phys. Lett.*, 64(16):pp. 2062–2064, 1994. [cited at p. 30]

[120] M. Travagnin, M. Van Exter, A.K. Jansen Van Doorn, and J.P. Woerdman. Erratum: Role of optical anisotropies in the polarization properties of surface-emitting semiconductor lasers [phys. rev. a 54, 1647 (1996)]. *Phys. Rev. A*, 55(6):pp. 4641–4641, 1997. [cited at p. 32]

[121] C. Serrat, N.B. Abraham, M. San Miguel, R. Vilaseca, and J. Martn-Regalado. Polarization dynamics in a vertical-cavity laser with an axial magnetic field. *Phys. Rev. A*, 53(6):pp. R3731–R3733, 1996. [cited at p. 32, 35]

[122] J.P. Woerdman, A.K. Jansen van Doorn, and M.P. van Exter. Symmetry breaking in vertical-cavity semiconductor lasers. *Laser Phys.*, 7(1):pp. 63–67, 1997. [cited at p. 32, 35]

[123] F. Prati, P. Caccia, M. Bache, and F. Castelli. Analysis of elliptically polarized states in vertical-cavity-surface-emitting lasers. *Phys. Rev. A*, 69(033810), 2004. [cited at p. 32, 35]

[124] T. Erneux, J. Danckaert, K. Panajotov, and I. Veretennicoff. Two-variable reduction of the San Miguel-Feng-Moloney model for vertical-cavity surface-emitting lasers. *Phys. Rev. A*, 59(6):pp. 4660–4667, 1999. [cited at p. 35]

[125] T. Ackemann and M. Sondermann. Characteristics of polarization switching from the low to the high frequency mode in vertical-cavity surface-emitting lasers. *Appl. Phys. Lett.*, 78(23):pp. 3574–3576, 2001. [cited at p. 35]

[126] M. Sondermann, T. Ackemanna, S. Balle, J. Mulet, and K. Panajotov. Experimental and theoretical investigations on elliptically polarized dynamical transition states in the polarization switching of vertical-cavity surface-emitting lasers. *Opt. comm.*, 235(4-6):pp. 421–434, 2004. [cited at p. 35, 54, 55, 132]

[127] M. Travagnin. Linear anisotropies and polarization properties of vertical-cavity surface-emitting semiconductor lasers. *Phys. Rev. A*, 56(5):pp. 4094–4105, 1997. [cited at p. 35]

[128] R. Seguin, A. Schliwa, T.D. Germann, S. Rodt, K. Ptschke, A. Strittmatter, U.W. Pohl, D. Bimberg, M. Winkelnkemper, T. Hammerschmidt, and P. Kratzer. Control of fine-structure splitting and excitonic binding energies in selected individual InAs/GaAs quantum dots. *App. Phys. Lett.*, 89(263109), 2006. [cited at p. 35]

[129] R. Seguin, A. Schliwa, S. Rodt, K. Ptschke, U.W. Pohl, and D. Bimberg. Size-dependent fine-structure splitting in self-organized InAs/GaAs quantum dots. *Phys. Rev. Lett.*, 95(257402), 2005. [cited at p. 35, 36, 37]

[130] D. Bimberg. *Semiconductor quantum dots: The Excitonic Zoo-novel devices for future applications.* In Optical Fiber Telecommunications V A. Elsevier, edited by I. P. Kaminow, T. Li, A. E. Willner edition, 2008. [cited at p. 36]

[131] M. Bayer, G. Ortner, O. Stern, A. Kuther, A.A. Gorbunov, A. Forchel, P. Hawrylak, S. Fafard, K. Hinzer, T.L. Reinecke, S.N. Walck, J.P. Reithmaier, F. Klopf, and F. Schfer. Fine structure of neutral and charged excitons in self-assembled In(Ga)As/(Al)GaAs quantum dots. *Phys. Rev. B*, 65(195315), 2002. [cited at p. 37]

[132] K. Kowalik, O. Krebs, A. Lematre, S. Laurent, P. Senellart, P. Voisin, and J.A. Gaj. Influence of an in-plane electric field on exciton fine structure in InAs-GaAs self-assembled quantum dots. *Appl. Phys. Lett.*, 86(041907), 2005. [cited at p. 37]

[133] Z. Xu. *Submonolayer Deposited InGaAs/GaAs Quantum Dot Heterostructures and Lasers.* PhD thesis, Technical University of Denmark, Lyngby, Denmark, 2004. [cited at p. 38]

[134] T.C. Damen, K. Leo, J. Shah, and J.E. Cunningham. Spin relaxation and thermalization of excitons in GaAs quantum wells. *App. Phys. Lett.*, 58(17):pp. 1902–1904, 1991. [cited at p. 38]

[135] X. Marie, P. Le Jeune, T. Amand, M. Brousseau, J. Barrau, M. Paillard, and R. Planel. Coherent control of the optical orientation of excitons in quantum wells. *Phys. Rev. Lett.*, 79(17):pp. 3222–3225, 1997. [cited at p. 38]

[136] A. Tackeuchi, Y. Nishikawa, and O. Wada. Room-temperature electron spin dynamics in GaAs/AlGaAs quantum wells. *App. Phys. Lett.*, 68(6):pp. 797–799, 1996. [cited at p. 38]

[137] H. Gotoh, H. Ando, H. Kamada, A. Chavez-Pirson, and J. Temmyo. Spin relaxation of excitons in zero-dimensional InGaAs quantum disks. *Appl. Phys. Lett.*, 72(11):pp. 1341–1343, 1998. [cited at p. 38]

[138] M. Paillard, X. Marie, P. Renucci, T. Amand, A. Jbeli, and J.M. Grard. Spin relaxation quenching in semiconductor quantum dots. *Phys. Rev. Lett.*, 86(8):pp. 1634–1637, 2001. [cited at p. 38]

[139] A. Tackeuchi, R. Ohtsubo, K. Yamaguchi, M. Murayama, T. Kitamura, T. Kuroda, and T. Takagahara. Spin relaxation dynamics in highly uniform InAs quantum dots. *Appl. Phys. Lett.*, 84(18):pp. 3576–3578, 2004. [cited at p. 38]

[140] H. Gotoh, H. Kamada, H. Ando, and J. Temmyo. Exciton spin relaxation properties in zero dimensional semiconductor quantum dots. *Jpn. J. Appl. Phys.*, 42:pp. 3340–3349, 2003. [cited at p. 38]

[141] M.I. Dyakonov. *Spin Physics in Semiconductors*, volume 157 of *Springer Series in Solid-State Sciences*. Academic Press, Boston, 2008. [cited at p. 38]

[142] A.W. Holleitner, V. Sih, R.C. Myers, A.C. Gossard, and D.D. Awschalom. Dimensionally constrained Dyakonov-Perel spin relaxation in n-InGaAs channels: transition from 2D to 1D. *New J. Phys.*, 9(342):pp. 1–12, 2007. [cited at p. 38]

[143] P.-F. Braun, X. Marie, L. Lombez, B. Urbaszek, T. Amand, P. Renucci, V.K. Kalevich, K.V. Kavokin, O. Krebs, P. Voisin, and Y. Masumoto. Direct observation of the electron spin relaxation induced by nuclei in quantum dots. *Phys. Rev. Lett.*, 94(116601), 2005. [cited at p. 38]

[144] B. Eble, P.-F. Braun, O. Krebs, L. Lombez, X. Marie, B. Urbaszek, T. Amand, D. Lagarde, P. Renucci, P. Voisin, A. Lematre, K. Kowalik, A. Kudelski, V.K. Kalevich, and K.V. Kavokin. Spin dynamics and hyperfine interaction in InAs semiconductor quantum dots. *Phys. stat. sol. (b)*, 243(10):pp. 2266–2273, 2006. [cited at p. 38]

[145] V.K. Kalevich, M. Paillard, K.V. Kavokin, X. Marie, A.R. Kovsh, T. Amand, Yu.G. Zhukov, A.E. Musikhin, V.M. Ustinov, E. Vanelle, and B.P. Zakharchenya. Spin redistribution due to pauli blocking in quantum dots. *Phys. Rev. B*, 64(045309), 2001. [cited at p. 39]

[146] C. Cao and D.G. Deppe. Impact of spin blocking on the energy relaxation of electrons in quantum-dot lasers. *App. Phys. Lett.*, 84(15):pp. 2736–2738, 2004. [cited at p. 39]

[147] M.B. Willemsen, M.U.F. Khalid, M.P. van Exter, and J.P. Woerdman. Polarization switching of a vertical-cavity semiconductor laser as a Kramers hopping problem. *Phys. Rev. Lett.*, 82(24):pp. 4815–4818, 1999. [cited at p. 47, 51, 52]

[148] P. Hnggi, P. Talkner, and M. Borkovec. Reaction-rate theory: fifty years after Kramers. *Rev. Mod. Phys.*, 62(2):pp. 251–341, 1990. [cited at p. 51]

[149] H.A. Kramers. Brownian motion in a field of force and the diffusion model of chemical reactions. *Physica*, 7(4):pp. 284–304, 1940. [cited at p. 51]

[150] B. Nagler, M. Peeters, J. Albert, G. Verschaffelt, K. Panajotov, H. Thienpont, I. Veretennicoff, J. Danckaert, S. Barbay, G. Giacomelli, and F. Marin. Polarization-mode hopping in single-mode vertical-cavity surface-emitting lasers: Theory and experiment. *Phys. Rev. A*, 68(013813), 2003. [cited at p. 51, 52, 55, 130]

[151] G. Giacomelli and F. Marin. Statistics of polarization competition in vcsels. *Quantum Semiclass. Opt.*, 10:pp. 469–476, 1998. [cited at p. 51]

[152] M. Sondermann, M. Weinkath, T. Ackemann, J. Mulet, and S. Balle. Two-frequency emission and polarization dynamics at lasing threshold in vertical-cavity surface-emitting lasers. *Phys. Rev. A*, 68(033822), 2003. [cited at p. 51]

[153] J. Kaiser, C. Degen, and W. Elsasser. Polarization-switching influence on the intensity noise of vertical-cavity surface-emitting lasers. *J. Opt. Soc. Am. B*, 19(4):pp. 672–677, 2002. [cited at p. 51]

[154] M. Sciamanna, K. Panajotov, H. Thienpont, I. Veretennicoff, P. Mgret, and M. Blondel. Optical feedback induces polarization mode hopping in vertical-cavity surface-emitting lasers. *Opt. Lett.*, 28(17):pp. 1543–1545, 2003. [cited at p. 51]

[155] K. Panajotov, M. Sciamanna, A. Tabaka, P. Megret, M. Blondel, G. Giacomelli, F. Marin, H. Thienpont, and I. Veretennicoff. Residence time distribution and coherence resonance of optical-feedback-induced polarization mode hopping in vertical-cavity surface-emitting lasers. *Phys. Rev. A*, 69(011801(R)), 2004. [cited at p. 51]

[156] J. Houlihan, D. Goulding, Th. Busch, C. Masoller, and G. Huyet. Experimental investigation of a bistable system in the presence of noise and delay. *Phys. Rev. Lett.*, 22(5):pp. 050601:1–4, 2004. [cited at p. 51]

[157] I. Gatare, M. Triginer, H. Thienpont, K. Panajotov, and M. Sciamanna. Experimental study of polarization switching and polarization mode hopping induced by optical injection in VCSELs. *Proceedings Symposium IEEE/LEOS Benelux Chapter, Ghent*, pages pp. 143–146, 2004. [cited at p. 51]

[158] A.K. Jansen van Doorn, M.P. van Exter, and J.P. Woerdman. Tailoring the birefringence in a vertical-cavity semiconductor laser. *App. Phys. Lett.*, 69(24):pp. 3635–3637, 1996. [cited at p. 51]

[159] L. Olejniczak, M. Sciamanna, H. Thienpont, K. Panajotov, A. Mutig, F. Hopfer, and D. Bimberg. Polarization switching in quantum-dot vertical-cavity surface-emitting lasers. *IEEE Phot. Techn. Lett.*, 21(14):pp. 1008–1010, 2009. [cited at p. 52, 130]

[160] B. Kelleher, D. Goulding, S.P. Hegarty, G. Huyet, D.-Y. Cong, A. Martinez, A. Lematre, A. Ramdane, M. Fischer, F. Gerschtz, and J. Koeth. Excitable phase slips in an injection-locked single-mode quantum-dot laser. *Opt. Lett.*, 34(4):pp. 440–442, 2009. [cited at p. 61, 66, 67, 69, 75, 77, 84, 86, 87, 95, 134]

[161] S.H. Strogatz. *Nonlinear Dynamics and Chaos with Applications to Physics, Biology, Chemistry and Engineering.* Perseus Books. [cited at p. 62, 65, 83, 94, 104, 135]

[162] S. Wieczorek, T.B. Simpson, B. Krauskopf, and D. Lenstra. Global quantitative predictions of complex laser dynamics. *Phys. Rev. E*, 65(045207 R), 2002. [cited at p. 62, 63]

[163] E.M. Izhikevich. *Dynamical Systems in Neuroscience: The Geometry of Excitability and Bursting.* The MIT Press, London, England, 2007. [cited at p. 63, 64, 65]

[164] S. Wieczorek, B. Krauskopf, and D. Lenstra. A unifying view of bifurcations in a semiconductor laser subject to optical injection. *Opt. Comm.*, 172:pp. 279–295, 1999. [cited at p. 62, 63]

[165] H.G. Solari and G.-L. Oppo. Laser with injected signal: perturbation of an invariant circle. *Opt. Comm.*, 111:pp. 173–190, 1994. [cited at p. 65]

[166] M.G. Zimmermann, M.A. Natiello, and H.G. Solari. Sil'nikov-saddle-node interaction near a codimension-2 bifurcation: Laser with injected signal. *Physica D*, 109(3):pp. 293–314, 1997. [cited at p. 65]

[167] T.B. Simpson, J.M. Liu, A. Gavrielides, V. Kovanis, and P.M. Alsing. Period-doubling cascades and chaos in a semiconductor laser with optical injection. *Phys. Rev. A*, 51(5):pp. 4181–4185, 1995. [cited at p. 65]

[168] S. Melnik, O. Rasskazov, and G. Huyet. A route to robust double pulse excitability in optically injected semiconductor lasers. *J. Phys.: Conf. Ser.*, 138(012014), 2008. [cited at p. 66]

[169] B. Lindnera, J. Garcia-Ojalvo, A. Neimand, and L. Schimansky-Geiere. Effects of noise in excitable systems. *Phys. Rep.*, 392:pp. 321–424, 2004. [cited at p. 66, 68]

[170] P. Coullet, T. Frisch, J.M. Gilli, and S. Rica. Excitability in liquid crystal. *Chaos*, 4(3):pp. 485–489, 1994. [cited at p. 66]

[171] D. Dunfield and K. Haas. In vivo single-cell excitability probing of neuronal ensembles in the intact and awake developing Xenopus brain. *Nature Protocols*, 5:pp. 841–848, 2010. [cited at p. 66]

[172] D. OBrien, S.P. Hegarty, G. Huyet, and A.V. Uskov. Sensitivity of quantum-dot semiconductor lasers to optical feedback. *Opt. Lett.*, 29(10):pp. 1072–1074, 2004. [cited at p. 70]

[173] A.V. Uskov, Y. Boucher, J. Le Bihan, and J. McInerney. Theory of a self-assembled quantum-dot semiconductor laser with auger carrier capture: Quantum efficiency and nonlinear gain. *App. Phys. Lett.*, 73(11):pp. 1499–1501, 1998. [cited at p. 71]

[174] D.R. Matthews, H.D. Summers, P.M. Smowton, and M. Hopkinson. Experimental investigation of the effect of wetting-layer states on the gain-current characteristic of quantum-dot lasers. *App. Phys. Lett.*, 81(4904), 2002. [cited at p. 71]

[175] T. Erneux, E.A. Viktorov, and P. Mandel. Time scales and relaxation dynamics in quantum-dot lasers. *Phys. Rev. A*, 76(023819), 2007. [cited at p. 72]

[176] T. Erneux, E.A. Viktorov, P. Mandel, S. Azouigui, and A. Ramdane. Relaxation characteristics of quantum-dash-based semiconductor lasers. *App. Phys. Lett.*, 95(231107), 2009. [cited at p. 72]

[177] E. Doedel, T. Fairgrieve, B. Sandstede, A. Champneys, Yu. Kuznetsov, and X. Wang. AUTO, `http://indy.cs.concordia.ca/auto/`, jun 2009. [cited at p. 75, 103, 104, 110, 132]

[178] S. Wieczorek, B. Krauskopf, and D. Lenstra. Multipulse excitability in a semiconductor laser with optical injection. *Phys. Rev. Lett.*, 88(063901), 2002. [cited at p. 77]

[179] S. Wieczorek and B. Krauskopf. Bifurcations of n-homoclinic orbits in optically injected lasers. *Nonlinearity*, 18(3):pp. 1095–1120, 2005. [cited at p. 77, 134]

[180] B. Krauskopf, K. Schneider, J. Sieber, S. Wieczorek, and M. Wolfrum. Excitability and self-pulsations near homoclinic bifurcations in semiconductor laser systems. *Opt. Comm.*, 215(4-6):pp. 367–379, 2003. [cited at p. 77]

[181] S. Wieczorek and D. Lenstra. Spontaneously excited pulses in an optically driven semiconductor laser. *Phys. Rev. E*, 69(016218), 2004. [cited at p. 77, 87]

[182] T. Erneux, E.A. Viktorov, B. Kelleher, D. Goulding, S.P. Hegarty, and G. Huyet. Optically injected quantum-dot lasers. *Opt. Lett.*, 35(7):937–939, 2010. [cited at p. 77]

[183] Dstool, `http://mathlab.cit.cornell.edu/dyn_sys/dstool/dstool.html`, 2009. [cited at p. 83]

[184] E. Fontich and J. Sardanyes. General scaling law in the saddlenode bifurcation: a complex phase space study. *J. Phys. A: Math. Theor.*, 41(015102), 2008. [cited at p. 84, 94]

[185] O.V. Ushakov, H.-J. Wnsche, F. Henneberger, I.A. Khovanov, L. Schimansky-Geier, and M.A Zaks. Coherence resonance near a Hopf bifurcation. *Phys. Rev. Lett.*, 95(123903), 2005. [cited at p. 89]

[186] M.A. Arteaga, M. Valencia, M. Sciamanna, H. Thienpont, M. Lopez-Amo, and K. Panajotov. Experimental evidence of coherence resonance in a time-delayed bistable system. *Phys. Rev. Lett.*, 97(023903), 2007. [cited at p. 89]

[187] S. Osborne, K. Buckley, A. Amann, and S. OBrien. All-optical memory based on the injection locking bistability of a two-color laser diode. *Opt. Express.*, 17:6293–6300, 2009. [cited at p. 103]

[188] L. Olejniczak, K. Panajotov, H. Thienpont, and M. Sciamanna. Self-pulsations and excitability in optically injected quantum dot lasers: impact of the excited states and spontaneous emission noise. *Phys. Rev. A*, 82(023807), 2010. [cited at p. 104]

[189] Z.G. Pan, S. Jiang, M. Dagenais, R.A. Morgan, K. Kojima, M.T. Asom, R.E. Leibenguth, G.D. Guth, and M.W. Focht. Optical injection induced polarization bistability in vertical-cavity surface-emitting lasers. *Appl. Phys. Lett.*, 63(2999), 1993. [cited at p. 119]

[190] T. Mori, Y. Yamayoshi, and H. Kawaguchi. Low-switching-energy and high-repetition-frequency all-optical flip-flop operations of a polarization bistable vertical-cavity surface-emitting laser. *Appl. Phys. Lett.*, 88(101102), 2006. [cited at p. 119]

[191] Y. Onishi, N. Nishiyama, C. Caneau, F. Koyama, and C.E. Zah. Optical inverter using a vertical-cavity surface-emitting laser with external light injection. *Proc. IEEE, LEOS 2003*, 2:pp. 708–709, 2006. [cited at p. 119]

Résumé

Dans cette thèse nous présentons dans un premier temps nos résultats expérimentaux sur les instabilités de polarisation de lasers à boîtes quantiques (QD) et à cavité verticale (VCSELs). Ces instabilités présentent des caractéristiques différentes de celles observées dans les lasers VCSELs à puits quantiques: une compétition se produit entre deux états polarisés elliptiquement et non orthogonaux, qui donne lieu à une dynamique de saut de mode de polarisation dans le temps. Le temps de séjour moyen dans un mode décroit de huit ordres de grandeur en augmentant le courant d'injection (de la seconde à la nanoseconde). A notre connaissance ceci constitue la première observation d'une dynamique de polarisation d'un VCSEL avec une échelle de temps aussi diversifiée. Nous présentons ensuite une étude théorique d'un laser QD avec injection optique, en prenant en compte la dynamique des porteurs de charge vers des états énergétiques excités. Nous montrons qu'aux dynamiques d'impulsions excitables observées expérimentalement s'ajoutent des dynamiques auto-pulsées complexes résultant d'une phénomène de bifurcation autour d'un point de selle *bottleneck*. Finalement nous avons étudié le cas d'un laser QD émettant simultanément depuis les états d'énergie fondamental et excité. Alors que la lumière est injectée dans laser QD esclave à la fréquence proche de l'état d'énergie fondamental, nous montrons que l'émission à la fréquence de l'état excité présente une dynamique auto-pulsée avec des impulsions très courtes (ps) suite à un mécanisme de basculement de gain.

Summary

In this thesis we first show our experimental results on polarization instabilities in quantum dot (QD) lasers with vertical cavity, so called VCSELs. Their characteristics are different from what is typically observed in their QW counterparts: light that is linearly polarized close to lasing threshold becomes elliptically polarized as current is increased and then a wide region of polarization mode hopping between nonorthogonal, elliptically polarized modes sets on. Within this region the average dwell time decreases by eight orders of magnitude from seconds to nanoseconds. To our best knowledge this is the first observation of such a diversified dynamics of polarization mode hopping in a single VCSEL. We have also carried out theoretical studies of optically injected QD lasers accounting for the intradot carrier dynamics through the higher-energy excited states. We show that experimentally observed excitable pulses are complemented by self-pulsations resulting from the so-called bottleneck phenomenon. Finally, we have theoretically investigated optically injected QD laser lasing simultaneously from the ground and excited states. We show that although the external light is injected to the ground state mode alone, modulation of the relaxation time induced by injected signal can provide a gain switching mechanism leading to generation of picosecond pulses from the excited state.